# One-dimensional Photonic Crystal / Photonic Wire Cavities Based on Silicon-on-Insulator (SOI)

**Ahmad Rifqi Md Zain**

April 2009

A thesis submitted for the degree of
Doctor of Philosophy (Ph.D.) to the Faculty of Engineering
Department of Electrical and Electronics Engineering
University of Glasgow

# ABSTRACT

It has been of major interest in recent research to produce faster optical processing for many telecommunications applications, as well as other applications of high performance optoelectronics. The combination of one-dimensional photonic crystal structures (PhC) and narrow photonic wire (PhW) waveguides in high refractive-index contrast materials such as silicon-on-insulator (SOI) is one of the main contenders for provision of various compact devices on a single chip. This development is due to the ability of silicon technology to support monolithic integration of optical interconnects and form fully functional photonic devices incorporated into CMOS chips. The high index contrast of the combination of a silicon core with a surrounding cladding of silica and/or air provides strong optical confinement, leading to the realization of more compact structures and small device volumes. In order to obtain a wide range of device functionality, the reduction of propagation losses in narrow wires is equally important, although there are still performance limitations determined by fabrication processes. Compact single-row PhC structures embedded in PhW waveguide micro-cavities could become essential components for wavelength selective devices, especially for possible application in WDM systems. The high quality factor, Q, and confinement of light in a small volume, V, are important for optical signal processing and filtering purposes, implying large Purcell factor values.

In this thesis, one-dimensional photonic crystal/photonic wire micro-cavities have been designed and modeled using both 2D and 3D versions of the finite-difference time-domain (FDTD) approach. These devices were fabricated using electron beam lithography (EBL) and reactive ion etching (RIE) for patterning of the silicon layer. The device structures were characterized with TE polarized light, using a tunable laser covering the range from 1480 nm to 1585 nm. Single-row periodic hole-type PhC mirrors consisting of identical and equally spaced holes were embedded in 500 nm wire waveguides. Two PhC hole mirrors were separated with a cavity spacer varying from 400 nm to 500 nm in length to form a micro-cavity. In contrast, several different cavity arrangements were also successfully investigated, - i.e. extended cavity and coupled micro-cavity structures.

The experimental results on photonic crystal/photonic wire micro-cavity structures have demonstrated that further enhancement of the quality-factor (Q-

factor) - up to approximately 149,000 at wavelengths in the fibre telecommunications range is possible. The Q-factor values and the useful transmission levels achieved are due, in particular, to the combination of both tapering within and outside the micro-cavity, with carefully designed hole diameters and non-periodic hole placement within the tapered sections. On the other hand, a large resonance quality factor of approximately 18,500, together with high normalized transmission of 85% through the use of tapering on both sides of the hole-type PhC mirrors that formed the micro-cavity, has been obtained. For the extended cavity case, the multiple resonances excited within the stop band, together with substantial tuning capability of the resonances obtained by varying the cavity length has been demonstrated, together with a Q-factor value of approximately 74,000 at the selected resonance frequency with a normalised transmission of 40%.

In addition, the coupled micro-cavity structures considered in this thesis have formed the basic building block for designing multiple cavity structures where the combination of several cavities splits the selected single cavity resonance frequency into a number of resonances that depends directly on the number of cavities used in the design. The coupling strength between the resonators and the Free Spectral Range (FSR) between the split resonance frequencies of the coupled cavity combination were controlled via the use of different numbers of periodic hole structures – and through the use of different aperiodic hole taper arrangements between the two cavities in the middle section of the mirrors.

## LIST OF PUBLICATIONS

**Journal papers**

1. <u>A.R.Md Zain</u>, N.P.Johnson, M.Sorel and R.M.De La Rue, "Coupling Strength Control in Photonic Crystal/Photonic Wire Multiple Cavity Devices", *Electronics Letters*, **20** (5), 26th February 2009.

2. <u>A.R.Md Zain</u>, N.P.Johnson, M.Sorel and R.M.De La Rue," Ultra high Quality Factor One Dimensional Photonic Crystal/Photonic Wire Micro-cavities in Silicon-on-Insulator (SOI)", *Optics Express*, **16** (16), August 2008.

3. <u>A.R.Md Zain</u>, Marco Gnan, Harold M. H. Chong, Marc Sorel and Richard M. De La Rue, "Tapered Photonic Crystal Micro-cavities Embedded in Photonic Wire Waveguides with Large Resonance Quality-Factor and High Transmission', *IEEE Photonic Technology Letts*, **20** (1), page 6 – 8, 1st of January 2008.

4. <u>A.R.Md Zain</u>, N.P.Johnson, M.Sorel and R.M.De La Rue," High Quality-Factor 1D-Suspended Photonic Crystal/Photonic Wire Silicon Waveguide", Draft ready for submission for *IEEE Photonic Technology Letters*, April 2009.

5. <u>A.R.Md Zain</u>, N.P.Johnson, M.Sorel and R.M.De La Rue," Modeling of 1D-Photonic Crystal/Photonic Wire Extended Cavity", in preparation April/May 2009.

**Conferences**

1. <u>Ahmad R.Md Zain</u>, Marc Sorel and R.M.De La Rue," Advancing the performance of One-Dimensional Photonic Crystal/Photonic Wire Microcavities in Silicon-on-Insulator", *Integrated Photonics and Nano-photonics Research and Applications (IPNRA)*, Boston, Massachusset, U.S.A, 13-16 July 2008.

2. <u>Ahmad R.Md Zain</u>, Marc Sorel and R.M.De La Rue," High Quality Factor Suspended-wire 1D Photonic Crystal Micro-cavity in Silicon-on-Insulator", *European Conference in Integrated Optics (ECIO) 2008*, Eindhoven, The Netherland, 11-13 June 2008.

3. <u>Ahmad R. Md Zain</u>, N.P.Johnson, R.M.De La Rue," High Transmisison 1D Photonic Crystal/Photonic Wire Multiple Cavity Structures Based on Silicon-

on-Insulator (SOI)", *Photonic Europe (SPIE Europe) 2008*, Strasbourg, France, 7-11 April 2008.

4. <u>Ahmad Rifqi Md Zain</u>, H.Chong, N.Johnson, R.M.De La Rue", Fine Tuning of Single Row Photonic Crystal Extended Cavities Embedded in Photonic Wire Waveguides", *International Conference of Microelectronics, MEMS and Nanotechnology*, Australian National University (ANU), Canberra, Australia, 4-7 December 2007.

5. <u>Ahmad R.Md Zain</u>, H.M.H.Chong, A.Samarelli, M.Gnan, M.Sorel, R.M.De La Rue,"Photonic Crystal (PhC) micro-cavity filters embedded in Silicon on Insulator (SOI) photonic wire waveguides", *International Conference of Micro-Technologies For The New Millennium 2007*, Gran Canaria, Spain, 2 - 4th May 2007

6. <u>Ahmad R.Md Zain</u>, R.M.De La Rue," Design, Fabrication and measurement of SOI based photonic wire devices, including Bragg Grating structures", *IEEE 8th International Conference on Transparent Optical Networks (ICTON) 2006*, Vol:4, page 274-274, June 2006, Nottingham, UK.

**OTHER PUBLICATIONS:**

**Journal Paper**

1. Michele Belotti, Matteo Galli, Dario Gerace, Lucio Claudio Andreani, and Giorgio Guizzetti, <u>Ahmad R. Md Zain</u>, Nigel P. Johnson, Marc Sorel, and Richard M. De La Rue ", All-optical switching in silicon-on-insulator photonic wire nano-cavities", Recently submitted for publication in Optics Express, April 2009.

2. Richard De La Rue, Harold Chong, Marco Gnan, Nigel Johnson, Iraklis Ntakis, Pierre Pottier, Marc Sorel, <u>Ahmad Md Zain</u>, Hua Zhang, Edilson Camargo, Chongjun Jin, Mario Armenise and Caterina Ciminell 'Photonic crystal and photonic wire nano-photonics based on silicon-on-insulator', *New Journal of Physics*, 8, (2006) 256.

**Conferences**

1. Michele Belotti, Matteo Galli, Dario Gerace, Lucio Claudio Andreani, and Giorgio Guizzetti, <u>Ahmad R. Md Zain</u>, Nigel P. Johnson, Marc Sorel, and Richard M. De La Rue", All Optical Switching in Silicon-on-Insulator

Photonic Wire Nano-cavities", *IEEE LEOS Winter Topical 2009*, Inssbruck, Austria, January 2009.

2. Y.Jourlin, E.Gamet, Olivier M. Parriaux, Stéphanie Reynaud; Anne Talneau; Petri Karvinen, Nicolas Passilly, Joensuu Yliopisto ; Ahmad Md Zain, Richard M. De La Rue, Univ. of Glasgow, " DUV phase mask for 100 nm period grating printing", *Photonic Europe* (SPIE Europe), Paper 6992-11, Strasbourg, France, 7-11 April 2008.

3. M.Gnan, Ahmad R.Md Zain,H.M.H.Chong,R.M.De La Rue,"Modelling of photonic wire Bragg grating structure", *XIII International workshop, Optical waveguide theory and numerical modeling (OWTNM)*, Grenoble, France, 8-9 April 2005

4. A. Samarelli, Ahmad R.Md Zain, M.Gnan, H.M.H.Chong, M.Sorel, Richard De La Rue, Paola Frascella, Caterina Ciminelliand Mario Armenise," Single Row SOI-based Photonic Crystal/Photonic Wire Micro-cavities with Medium Q-factor and High Transmission", *Integrated Photonics and Nano-photonics Research and Appliations (IPNRA) 2007*, OSA Technical Digest (Optical Society of America, 2007), paper IWD5, Salt Lake City, Utah, USA, 8-11 July 2007.

# Acknowledgements

First of all I wish to acknowledge my supervisor, Professor Richard De La Rue for initially accepting me as his PhD student. His invaluable patience is highly appreciated - and has helped me to set sail through this challenging experience in order to complete my PhD. His patient, relentless advice and fruitful discussions are highly appreciated. His help, in particular, in improving my English and enlightening my knowledge in this area of research has been a source of real delight. These have been great years working with him. I'm also grateful for the financial support from the European Network of Excellence (ePIXnet), which has given me greater opportunity to meet and have memorable and fruitful discussions with other people with a variety of different expertise.

I would also like to express my thanks to all technical staff in the James Watt Nanofabrication Centre (JWNC) - who have helped me a lot in the technological aspects, including various training in using state-of-the art tools available within the lab. Many thanks go also to my second supervisor, Dr Nigel Johnson, and other research colleagues who have been involved directly or in-directly in sharing their technical views and discussions towards completing my PhD, especially Drs Marco Gnan, Marc Sorel and Harold Chong.

Finally and most importantly, I would like to express my deepest heartfelt gratitude to my late father, Mr Md Zain Hasan and my mother Mrs Shofiah Walat - and last but not least to my beloved wife, Anisah Karim, and my three wonderful children, Aiman Syafiq, Abdul Rasyid and Nur Mawaddah. Their smiles and their laughter make me feel motivated every single day. Their endless support after long hours of the working day, in and out, are highly memorable.

*In loving memory to my beloved father who passed away in March 2006 while I'm working on this present work…. wish you were here…*

AHMAD RIFQI MD ZAIN

# TABLE OF CONTENTS

# List of Figures

# List of Tables:

# CHAPTER 1: Introduction

## 1.1        Introduction

The potential importance of integrated optics was not fully realized until 1968. Light propagation in thin films has been proposed and developed extensively since then [1]. The term integrated optics relates to a wide variety of structures where the propagation of light is controlled by a thin dielectric film or by strips of dielectric. The range of laser frequencies available and the types of material used have their limitations.  Initially, gas laser and solid state lasers were used as the light sources in early experiments. There is a possible need for much smaller sources that can be used to achieve the requirement of integrated optics in order to integrate with other applications. For shorter wavelength regions, overcoming large absorption and scattering losses becomes a priority since the smaller wavelength range imposes limitations on the practical use of wave-guiding. In addition, waveguide integrated optics is based on electromagnetic wave-guiding at optical frequencies using thin film optics. In recent years, semiconductor devices have played a major role in the evolution of integrated optics, due to their significant properties relevant to the goal of monolithic integrated optical circuits. In the early 60s, research on thin film phenomena became the key route towards developing more complex waveguide properties. The guiding action of planar layers in p-n junctions was observed and reported in 1963 by Yariv and Leite [2] and Bond et al [3]. Their results have been subsequently used by Nelson and Reinhardt [4] in providing light modulation via the electro-optic effect. Although, there was no concern with the optical waveguide circuitry, this work was just the beginning of the new era of planar thin film waveguides. Light propagation in thin films has been proposed and developed since then [5]. The subject of dielectric periodic microstructures has become a priority ever since the evolution of lasers and integrated optics generally in the early 1960s [5-11]. This great evolution was just the beginning of the new era of development of photonic

microstructures on single compact chips. Much research has been carried out with the aim of providing faster optical communication and data processing - whether for entertainment, route switching or computational purposes. In recent years, the motivation towards producing compact and faster communication has become a platform for much research, including switching purposes.

In addition, the advance in photonics technology for many applications has emerged on a large scale, whether using active devices such as III-V semiconductor materials or even silicon and silica passive devices. But the latter two materials still work as a separate system, although the main aim is still to achieve a monolithic photonic integration that is capable of handling any application in a single chip. Developments based on the concepts formulated by Purcell [31, 32] regarding the effect of radiation properties due to the presence of mirrors have been discussed extensively. These ideas led to the new concept of photonic crystals (PhCs) [15, 16]. Instead of manipulating the electrons that are involved in the use of the conventional electronic properties of solids, where they can produce an electronic band-gap, photons are manipulated in periodic structures (photonic crystals) – and can exhibit stop-band and photonic band-gap (PBG) behaviour. In other words, photons are not allowed to propagate through the 'crystal' structures at all - and there can be a forbidden gap or band-gap.

Much of the attraction in the research areas of the micro and nano-photonics structures comes from the use of high refractive index contrast materials such as silicon-on-insulator (SOI) that have been increasingly used in recent years. This development is due to the ability of silicon technology to support monolithic integration of optical interconnects and form fully functional photonic devices that can be incorporated into CMOS chips. Soref et.al [12] have demonstrated the possibilities of passive and active silicon waveguides as long ago as 1985, with single-crystal silicon grown epitaxially on a heavily doped silicon substrate. The advances of silicon based and silicon-on-insulator optoelectronics have also been noted by Jalali et al in 1998 and Masini et al in 2002 [13-14].

**1.2         Photonic Crystal and Photonic Wire Waveguides**

The concept of photonic band-gap structures was independently proposed by Yablonovitch and by John in 1987 [15, 16]. PBG structures create the condition where, over a certain photon energy range, light can travel through the periodic structure - and is reflected back when impinging onto the crystal and is not allowed to propagate - thus creating a so-called forbidden zone. In 1991, the first experimental demonstrations have shown that by using an array of holes drilled into the high refractive index material, a stop-band is produced where no transmission is allowed over this frequency range [17]. Full PBG structures consist of three-dimensionally periodic structures that inhibit spontaneous emission within the electromagnetic band-gap. New designs have been developed and innovated based on this concept ever since, although improving the overall performance of the devices is still a major concern for full device functionality - and there is also performance limitations determined by the various fabrication processes [17-18]. 3D Photonic crystal structures (PhCs) are one of the possible contenders for the provision of highly compact devices on a single chip that will allow the realization of complex sub-systems. Due to the inherent difficulties of realising and controllably modifying 3D structures, work on 2D and 1D structures has emerged tremendously - which is partly due to the lesser design complexity and the reduction in size. But they can produce some interesting results that have contributed significantly towards the realisation of Photonic Integrated Circuits (PICs). The motivation towards miniaturising PIC devices has expanded the need to put more effort into designing compact photonic-crystal based devices. The massive development of telecommunication infrastructures has created a large demand for multiple applications realised on a single chip by using a combination of several optical sub-systems.

In general, photonic crystal device structures exhibit a strong optical confinement covering a fairly large frequency spectrum. Strong optical confinement is needed in a small volume to provide a suitable building block in the optical emission properties - thus creating enhancement of the luminescent 'atoms' through spontaneous emission. By creating a 'defect' or a small region surrounded by the photonic crystal arrangement, the basic properties of that photonic crystal lattice are significantly changed. In other words, the photonic crystal has the capability to

localise light when a 'defect' is introduced within the periodicity of the crystal arrangement - thus forming a micro-cavity that is surrounded by a highly reflective mirror region. For example, in 2D photonic crystal structures, a 'defect' or micro-cavity can be formed by simply removing one or more holes [34-36] - or by changing the surrounding hole sizes. [37-39]. Light that is strongly confined within the channel waveguide formed by the photonic crystal arrangement (square [40] or hexagonal lattice [41-42]) is directly coupled into the micro-cavity region. In this design arrangement, light may be guided through the structure by removing a single row of holes to form a channel waveguide - and in this way light can propagate at the characteristic frequency of the cavity, within the band-gap. Channel waveguides may be designed to have different widths, W, such as W1 [43] - where a single row of holes is removed to provide a channel waveguide. In other examples, W3 [44] consists of three hole removed and W0.7 [45] – i.e. a situation where the spacing between two blocks of photonic crystal is additionally increased by 0.7 of a lattice spacing. Recently, low propagation losses, 4.1 dB/cm, have been obtained in a single line defect W1 PhC channel waveguide [27] which shows that PhCs can provide a suitable platform for designing low loss devices. In 1D photonic crystal structures, the micro-cavity has great potential for producing a high quality factor in a small volume – thus providing a suitable platform to design a wavelength selective device for example for WDM applications using passive components such as multiplexers/de-multiplexers, optical switching, sensors and optical filters. On the other hand, in 1D photonic crystals, micro-cavities may be formed by creating a defect and using a smaller hole in the middle of a single row crystal, as shown in *Fig 1.1*.

In photonic crystal (PhC) micro-cavity structures, the optical properties may be characterised by the Q/V ratio (often called the Purcell factor [31-32, 46]), where Q is the Quality factor and V is the modal volume corresponding to the particular micro-cavity and its characteristic electromagnetic resonant modes. Thus designing high Q-factor optical micro-cavities confined in a small volume, V, may be useful for high speed optical processing- where light is confined within a small volume on the order of $(\lambda/2n)^3$ - and $\lambda$ is the emission wavelength and n is the refractive index of the given material. Different design configurations for achieving large quality-factor values have been considered - such as micro-pillars [48-50] - with Q-factor values in excess of 150,00 for 4 μm diameter pillars and a Q-factor value of 1500 for a 600 nm

diameter pillar, silica toroids [47,51], PhC cavities [28, 51, 52, 60, and 61], , in photonic wire waveguides or 2D PhC membrane [53-55] and slot waveguide [64] where the calculated quality factor is still as high as $2 \times 10^5$ with the mode volume, V as small as 0.14 of a cubic wavelength in a vacuum. For example, in 2D PhC structures, a Q-factor of $9 \times 10^5$ [60-61] and $1 \times 10^6$ [62] or greater [63] has been achieved by Notomi and co-workers, with modal volume, V of approximately 1.7 $(\lambda/n)^3$. On the other hand, Q-factor values as large as $10^8$ have also been obtained in silica toroids [51], but this design configuration has a relatively large modal volume, which gave Q/V of approximately $5.10^4$ $(\lambda/n)^3$. The interest in manufacturing ultrasmall micro-cavity device structures has been boosted by the capability of achieving modal volumes close to a theoretical minimum value of $V=(\lambda/2n)^3$.
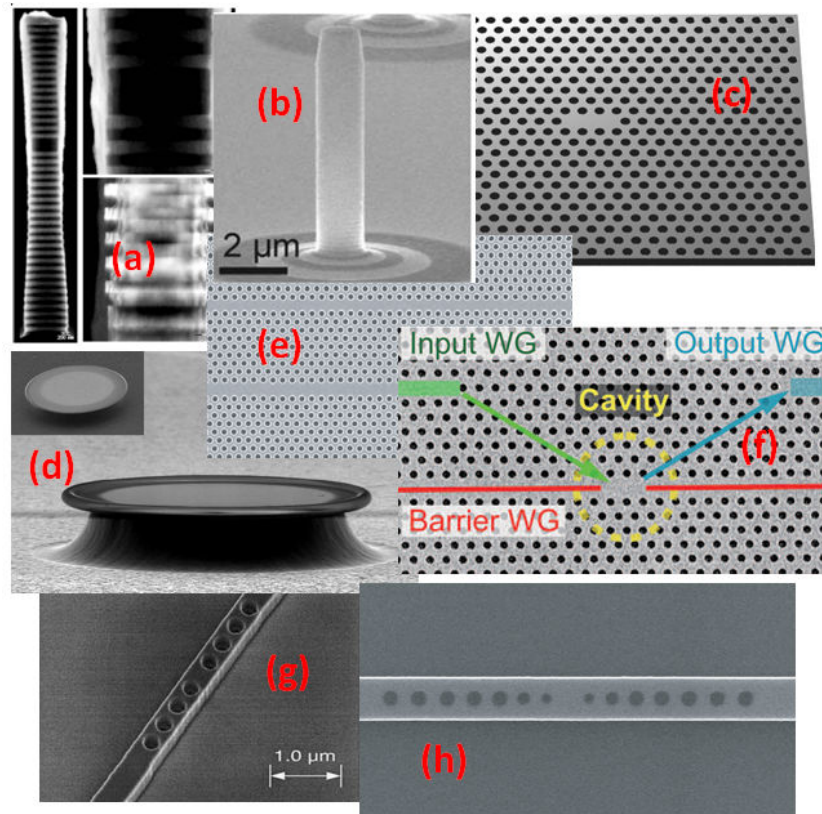


**Fig.1.0**: *An example of different cavity configuration which have been demonstrated with significantly high-Q with low modal volume, V (a) micro-pillar [50] (b) micro-pillar [49] (c) L3 cavity [54] (d) toroids [51] (e) 2D PhC heterostructure cavity [58] (f) PhC nano-cavity [61] (g) Initial work on 1D PhC/PhW [28] (h) Optimised 1D PhC/PhW [56]*

Based on the motivation towards large Purcell-factors, Q-factor values as large as $10^6$ have been achieved [58] and other configurations such as 1D PhCs [56-57], L3 cavities where three holes in line were removed to provide a micro-cavity section [54] and hetero-structure cavities [58-59].

This design has shown a great enhancement in the Q-factor, together with strong confinement within a small volume - and close to the theoretical value - through the use of the mode-matching mechanism. But in most cases, the footprints that the design covers are large, especially for 2D PhCs. Therefore, in order to design a compact device that requires a small foot-print and to satisfy the requirement for integration with other optical devices, 1D PhC/PhW device were proposed by Foresi et al [28] in 1997. The foot print of this particular device covers an area of approximately 1 μm by 3 μm. Using this design configuration, ultra-high Q-factor micro-cavities with resonant modes that can occupy small mode volume have already been demonstrated in [56,57]. The Q-value of these resonant structures is in excess of 50,000, with a modal volume of approximately 0.6 $(\lambda/n)^3$. This record value of Q/V ratio of approximately $10^6$ was obtained without the need to use membrane type structures. *Fig.1.0* shows examples of several different cavity arrangements that have produced high Q-factor values and low modal volumes close to the theoretical limiting value.

Therefore, in most optical telecommunication applications, there is a need to have 1D PhC/PhW device structures that offer the possibility for manipulation of light at infra-red wavelengths (around 1550 nm) – ruled by its capability of confined light within a small volume, V. Due to the fabrication challenges and the capability of designing structures that occupy very small areas, one-dimensional PhC structures have been preferred, although there are practical performance limitations. The devices typically consist of a single row of holes embedded in a narrow single-mode photonic-wire waveguide. On the other hand, photonic wire (PhW) device structures based on total internal reflection (TIR) concepts have shown a capability for reduced loss, together with less complexity. They can also provide strong optical confinement due to the large refractive index contrast between the waveguide core and its surrounding cladding, leading also to small device volumes and compact structures [19]. In addition the photonic wire approach also gives great flexibility for the design of structures such as sharp bends, abrupt Y-junctions, small device volumes, micro-

cavities and Mach Zehnder (MZ) structures [20- 26]. In other words, this concept is based on high refractive index contrast where light is confined in such a narrow ridge waveguide. The combination of one-dimensional photonic crystal (PhC) structures and photonic wire (PhW) waveguides in high refractive index materials such as silicon–on-insulator (SOI) became increasingly important in a number of research areas. In order to obtain a wide range of device functionality, the reduction of propagation losses in narrow photonic wires is equally as important as enhancing the performance of the device structures.

On the other hand, 1D PhC/PhW device structures have increasingly become a topic of interest - and use a mirror design that is based on a single periodic row of holes embedded in a narrow ridge waveguide, as shown in *Fig.1.1*. This approach was first introduced by Foresi et.al [28]. The periodic hole mirror characteristics can be varied by changing several parameters - such as hole diameter, cavity spacing and hole spacing - as will be described in detail in *Chapter 4*. In the present work, light confined within a PhC/PhW structure is directly coupled into the micro-cavity by using a tapered hole arrangement, as shown in *Fig.1.1*.
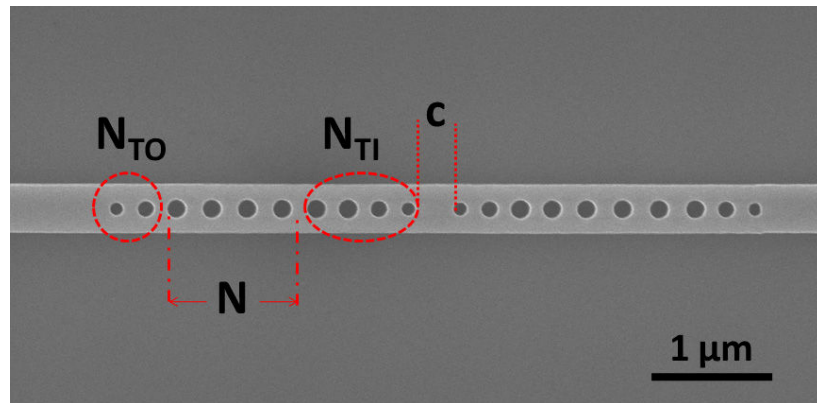


**Fig.1.1**: *1D PhC/PhW waveguide structures with a series of PhC hole of periodic spacing,a and ,hole diameter, d embedded in 500 nm wire. The tapered hole introduced has a number of hole tapered outside cavity, $N_{TO}$ and the number of tapered hole within cavity, $N_{TI}$ with cavity length, c. A periodic mirror has N number of equally spaced hole.*

These kinds of device structure also have the capability of providing compact structures in small device volumes, as compared to other more complex structures such as ring resonators - which occupy larger device volumes. Furthermore, 1D PhC/PhW structures may also be preferred, since they can exhibit large band gaps as compared to what 3D photonic crystal structures can offer - thus making the PhC/PhW approach a contender for filter devices that can be integrated with other photonic devices. The fact that they share similar concepts with grating filters helps in understanding how these devices operate. With the material properties of SOI, an extremely small waveguide working in single mode operation can be realised, with a reduction in propagation losses from 50 dB in 1996 [29] to 1.7 dB/cm in late 2006 [30] - and more recently a propagation loss value of 0.91 dB/cm [33] has been achieved. The other features that have led to increasing attention to this area of research are the ability to provide a platform for the confinement of light within a small volume - for example when a defect or a spacer is introduced between periodic mirrors. With this condition, light can be trapped within a small cavity, thus producing resonances that occur at certain frequencies within the stop-band. These structures have been characterised by their high Q-factor value, adequate normalised optical transmission and small modal volume.

## 1.3 Aims and Objectives:

The main aims and objectives of the present work are to design, fabricate and characterize 1D single-row Photonic Crystal cavities embedded in 500 nm wire waveguides. These device structures were designed to work with TE polarised light at a wavelength of around 1550 nm. Different cavity arrangement were explored, including micro-cavities with cavity spacer sections ranging in length from 390 to 500 nm, extended cavities with several micrometre lengths and two coupled micro-cavities consisting of two spacer sections inserted between periodic mirrors. Tapering effects using several aperiodic holes with different diameters and aperiodic spacing have been used to reduce modal mismatch between un-patterned wires and periodic mirrors regions – thus enhancing both the resonance quality factor and optical transmission of the device structures. In general, the aims and objectives of the present work can be divided into several areas as follows:

- To study sub-micrometre scale 1D photonic crystal/photonic wire device structures that are based on high index contrast material, in particular silicon-on-insulator (SOI).

- To use and understand the basic concepts of current state-of-the-art fabrication tools available within the James Watt Nano-fabrication Centre (JWNC). These tools are expected to produce high quality device structures on a nanometre scale. Optimizing the standard process used became one of the priorities, in order to achieve good device fabrication tolerances and reproducibility. Most of the patterning process of the PhC/PhW device structure used electron beam lithography (EBL).

- To exploit the properties of single row 1D Photonic Crystal/Photonic Wire cavity structures - which can be characterised using several parameters such as the length of the cavity spacer section, hole diameter and hole spacing.

- To design and study the effects of using mode-matching hole tapers consisting of aperiodically located holes with different diameters and aperiodic spacing situated outside and within the cavity – for different cavity conditions: such as micro-cavities, extended cavities and two coupled micro-cavities.

- To design, fabricate and characterize 1D PhC/PhW structure micro-cavities that exhibit high quality factor values of greater than 10,000, together with large optical transmission in small volumes – that are suitable for some telecom applications, such as Dense Wavelength Division Multiplexing (DWDM).

- Ability to tune the resonance wavelength through small differences in cavity lengths.

- To enhance the optical confinement of the light propagating through the waveguides by removing the buffer layer below the silicon guiding layer - thus improve the quality factor values, together with the optical transmission.

## 1.4　　　　Thesis Outline:

This thesis will present an up-date on progress in device miniaturization based on silicon photonics technology.

**Chapter 2** describes the Finite Difference Time Domain (FDTD) method used to model the device structures where various simulation tools have been used for comparison. Both 2D and 3D FDTD approaches have been considered.

**Chapter 3** describes the fabrication techniques used to produce 1D PhC/PhW device structures. This process includes pattern writing processes using a Vistec VB6 state-of-the art electron beam lithography (EBL) tool. Comparison has been made in term of the quality of fabrication outcomes between EBPBG5 and VB6 tools, showing great improvement with the latter. The patterns were dry-etched using reactive ion etching (RIE) techniques. On the other hand, silica wet chemical etching using Hydrofluoric acid (HF) is further demonstrated to produce membrane types of Photonic wire waveguides. This chapter will also describe the techniques used for characterizing the device structures.

**Chapter 4** demonstrates experimentally the effect of tapering within and outside the cavity of 1D PhC/PhW device structures that exhibit high quality factor values approaching 150,000 with reasonably large optical transmission. Issues related to enhancement of the Q-factor are discussed in this chapter. This chapter also underlines the need to achieve high Q values together with sufficiently large optical transmission for such devices to be useful for telecom applications such as Dense Wavelength Division Multiplexing (DWDM), all optical switching and non-linear optics. It also investigates further enhancement of optical confinement via removal of the silica cladding/buffer layer in order to improve the symmetrical condition of the mode propagating through the hole mirrors within the wire waveguides. Due to time constraints, investigations concentrated on the tapered micro-cavity structures.

**Chapter 5** describe the effect of the hole and mirror tapering used in chapter *four* on different cavity arrangements such as extended cavities having a cavity length of between 2 and 9 μm  -and structures based on two coupled micro-cavities inserted

between periodic hole mirrors. Different hole tapering arrangements were also described in this chapter.

**Chapter 6** concludes the present work on high quality factor tapered mirror PhC/ PhW waveguide micro- cavities based on Silicon-on-Insulator (SOI) and follows with suggestions for future work that should be explored, especially the use of device structures demonstrated in Chapters *three, four and five* for achieving monolithic integration into Photonic Integrated Circuits (PICs).

**References:**

1.  S.E.Miller, "Integrated optics:An Introduction," Bell System Technical Journal, Vol: 48, pp 2059-2070,(1969).

2.  A.Yariv,R.C.C.Leite: *Applied physics letters*, vol. 2, no. 55 (1963).

3.  W.L.Bond, B.G.Cohen, R.C.C. Leite and A.Yariv: *Applied Physics Letters*, vol. 2, no. 57 (1963)

4.  D.F.Nelson, F.K.Reinhardt: *Applied Physics Letters*, vol. 5, no. 148 (1964).

5.  Nathan, M. I., Dumke, W. D., Burns, G., Dill, F. H. Jr., and Lasher, G., "Stimulated emission of radiation from GaAs p-n junction", *Applied Physics Letters*, vol. 1, no. 62, 1962.

6.  Basov, N. G., Vul, B., and Popov, Yu. M., (1959): Zh. Eksperim. Teor. Fiz., 37, pp. 587-588 [(1960): Sov. Phys. – JETP, 10, pp. 416].

7.  Maiman, T. H., "Stimulated Optical Radiation by Ruby Lasers," Nature, 187, pp. 493, 1960.

8.  Hall, R. N., Fenner, G. E., Kingsley, J. D., Soltys, T. J., and Carlson, R. O., "Coherent light emission from GaAs junction", *Physical Review Letters*, 9, pp. 366-368, 1962.

9.  Kogelnik, H., "An introduction to integrated optics", *IEEE Transactions on Microwave Theory and Techniques*, vol. 23, no. 1, pp. 2-16, 1975.

10. Adams, M. J., Steventon, A. G., Devlin, W. J., and Henning, I. D., "Semiconductor lasers for long-wavelength optical fibre communications systems", *IEE Materials and Devices Series* 4, Peter Peregrinus, 1987.

11. Quist, T. M., Rediker, R. H., Keyes, R. J., Krag, W. E., Lax, B., McWhorter, A. L., and Zeiger, H. J., "Semiconductor maser of GaAs", *Applied Physics Letters*, vol. 1, no. 91, 1962.

12. Soref, R. A., and Lorenzo, J. P., "All-silicon active and passive guided-wave components for $\lambda$ = 1.3 $\mu$m and 1.6 $\mu$m", *IEEE Journal of Quantum Electronics*, vol. 22, no. 6, pp. 873-839, 1986.

13. Masini, G., Colace, L., and Assanto, G., "Si based optoelectronics for communications", *Material Science and Engineering B*, vol. 89, pp. 2-9, 2002.

14. Jalali, B., Yegnanarayanan, S., Yoon, T., Yoshimoto, T., Rendina, I, and Coppinger, F., "Advances in Silicon-on-insulator Optoelectronics", IEEE

*Journal of Selected Topics in Quantum Electronics*, vol. 4, no. 6, pp. 938-947, 1998.

15. John, S., "Strong Localization of Photons in Certain Disordered Dielectric Superlattices", *Physical Review Letters*, vol. 58, no. 23, pp. 2486-2489, 1987.

16. Yablonovitch, E., "Inhibited Spontaneous Emission in Solid-State Physics and Electronics", *Physical Review Letters*, vol. 58, no. 20, pp. 2059-2062, 1987.

17. Krauss TF and De la Rue RM, 'Photonic crystals in the optical regime - past, present and future', *Progress in Quantum Electronics*, vol. 23, no. 2, March, 1999.

18. Krauss TF, 'Planar photonic crystal waveguide devices for integrated optics', *Physica Status Solidi A-Applied Research*, vol. 197, no. 3, June, 2003.

19. Bogaerts W, Taillaert D, Luyssaert B, Dumon P, Van Campenhout J, Bienstman P, Van Thourhout D, Baets R, Wiaux V, and Beckx S, 'Basic structures for photonic integrated circuits in silicon- on-insulator', *Optics Express*, vol. 12, no. 8, April, 2004.

20. Ahmad RU, Pizzuto F, Camarda GS, Espinola RL, Rao H, and Osgood RM, 'Ultracompact corner-mirrors and T-branches in silicon-on- insulator', *IEEE Photonics Technology Letters*, vol. 14, no. 1, January, 2002.

21. F.Ohno, T. Fukuzawa and T. Baba," Mach–Zehnder Interferometers Composed of μ-Bends and μ-Branches in a Si Photonic Wire Waveguide", *Japanese Journal of Applied Physics*, vol. 44, no. 7A, 2005, pp. 5322–5323, 2005

22. Richard De La Rue, Harold Chong, Marco Gnan, Nigel Johnson, Iraklis Ntakis, Pierre Pottier, Marc Sorel, Ahmad Md Zain, Hua Zhang, Edilson Camargo, Chongjun Jin, Mario Armenise and Caterina Ciminell 'Photonic crystal and photonic wire nano-photonics based on silicon-on-insulator', *New Journal of Physics*, vol. **8**, no. 256, (2006).

23. E. A. Camargo, H. M. H. Chong, and R. M. De La Rue, 'Highly compact asymmetric Mach-Zehnder device based on channel guides in a two-dimensional photonic crystal', *Appl. Opt.,* **45**, pp. 6507-6510, 1st Sept (2006).

24. E.A. Camargo, H.M.H. Chong and R.M. De La Rue, 'Four-port coupled channel-guide device based on 2D photonic crystal structure', *Photonics and*

*Nanostructures - Fundamentals and Applications*, 2(3), $^{\text{pp}}$. 207-213, December (2004).

25. Hua Zhang, M. Gnan, N.P. Johnson and R.M. De La Rue, 'Ultra-Small Mach-Zehnder Interferometer Devices in Thin Silicon-on-Insulator', *Integrated Photonics Research and Applications (IPRA),* Uncasvil$^{\text{le}}$, Conn., USA, April (2006).

26. Zhao CZ, Li GZ, Liu EK, Gao Y, and Liu XD, 'Silicon-On-Insulator Mach-Zehnder Wave-Guide Interferometers Operating at 1.3 μm', *Applied Physics Letters*, vol. 67, no. 17, October, 1995.

27. L.O'Faolain et.al, "Low loss propagation in Photonic Crystal Waveguide" *Electronic Letters*, no. 25, vol. 42, December 2006.

28. J.S.Foresi, P.R Villeneuve, J.Ferrera. E.R.Thoen, G.Steinmeyer, S.Fan. J.D.Jonnopoulos, L.C.Kimmerling, Henry.I.Smith and E.P.Ippen" *Photonic Bandgap microcavities in optical waveguides*", Nature, 390, 143-145, November 1997.

29. A. Sakai, G. Hara, and T. Baba, "Propagation characteristics of ultrahigh-Delta optical waveguide on silicon-on-insulator substrate," *Japanese Journal of Applied Physics Letters*, vol. 40, no. 4B, pp. L383–L385, 2001.

30. F. Xia, L. Sekaric, and Y. A. Vlasov, "Ultracompact optical buffers on a silicon chip," *Nature Photonics*, vol. 1, no. 1, pp. 65–71, 2007.

31. E. M. Purcell, H. C. Torrey, and R. V. Pound, *Physical Review*, Vol. 69, p. 37 (1946)

32. E. M. Purcell, *Physical Review*, Vol. 69, p. 681 (1946)

33. M. Gnan, S. Thoms, D. S. Macintyre, R. M. De La Rue, and M. Sorel, "Fabrication of low-loss photonic wires in silicon-on-insulator using hydrogen silsesquioxane electron-beam resist," *Electronics Letters,* vol. 44, pp. 115-116, 2008.

34. Joannopoulos, J. D., Meade, R. D., and Winn, J. N., "Photonic Crystals Molding the Flow of Light", Princeton University Press, 1995.

35. Scherer, A., Painter, O., Vuckovic, J., Loncar, M. and Yoshie, T., "Photonic crystals for confining, guiding, and emitting light", *IEEE Transaction on Nanotechnology*, vol. 1, no. 1, pp. 4-11, 2002.

36. Yoshie, T, Vuckovic, J., Scherer, A., Chen. H., and Deppe, D., "High quality two-dimensional photonic crystal slab cavities", *Applied Physics Letters*, vol. 79, no. 26, pp. 4289-4291, 2001.

37. Park, H-G, Hwang, J-K., Huh, J., Ryu, H-Y., Lee, Y-H., and Kim, J-S., "Nondegenerate monopole-mode two-dimensional photonic band gap laser", *Applied Physics Letters*, vol. 79, no. 19, pp. 3032-3034, 2001.

38. Painter, O., Vuckovic, J., and Scherer, A., "Defect modes of a two-dimensional photonic crystal in an optically thin dielectric slab", *Journal of the Optical Society of America B*, vol. 16, no. 2, pp. 275-285, 1999.

39. Ryu, H-Y, Notomi, M., and Lee, Y-H., "High-quality-factor and small-mode-volume hexapole modes in photonic-crystal-slab nanocavities", *Applied Physics Letters*, vol. 83, no. 21, pp. 4294-4296, 2003.

40. Jin, C., Fan, S., Han, S., and Zhang, D., "Reflectionless multichannel wavelength demultiplexer in a transmission resonator configuration", *IEEE Journal of Quantum Electronics*, vol. 39, no. 1, pp. 160-165, 2003.

41. Chong, H., and De La Rue, R. M., "Planar photonic crystal microcavities for add/drop filter functionality", post-deadline paper for 11th European Conference on Integrated Optics (ECIO 2003), Prague, Czech Republic, 2003.

42. Lin, S. Y., Chow, E., Johnson, S. G., and Joannopoulos, J. D., "Direct measurement of the quality factor in a two-dimensional photonic-crystal microcavity", *Optics Letters*, vol. 26, no. 23, pp. 1903-1905, 2001.

43. Loncar, M., Nedeljkovic, D., Doll, T., Vuckovic, J., Scherer, A., and Pearsall,T, "Waveguiding in planar photonic crystals", *Applied Physics Letters*, vol. 77, no. 13, pp. 1937-1939, 2000.

44. Olivier, S., Benisty, H., Smith, C. J. M., Rattier, M., Weisbuch, C., and Krauss, T. F., "Transmission properties of two-dimensional photonic crystal channel waveguides", *Optical and Quantum Electronics*, vol. 34, pp. 171-181, 2002.

45. Notomi, M., Shinya, A., Yamada, K., Takahashi, J, Takahashi, C., and Yokohama, I., "Singlemode transmission within photonic bandgap of width-varied single-line-defect photonic crystal waveguides on SOI substrates", *Electronics Letters*, vol. 37, no. 5, pp. 293-295, 2001.

46. E.M.Purcell,"Spontaneous emission probabilities at radio frequencies", *Physical Review Letters*, Vol. 69, p.681, 1946.

47. D. K. Armani, T. J. Kippenberg, S. M. Spillane & K. J. Vahala, "Ultralow-threshold microcavity Raman laser on a microelectronic chip," *Nature* **421**, 925 (2003).

48. K. Iga, F. Koyama, and S. Kinoshita, Surface emitting semiconductor-lasers, IEEE J. Quantum Electron. 24, 1845–1855 (1988).

49. S. Reitzenstein, C. Hofmann, A. Gorbunov, M. Gorbunov, M. Strauss, S. H. Kwon, C. Schneider, A. L¨offler, S. Hoefling, M. Kamp, and A. Forchel, AlAs/GaAs micropillar cavities with quality factors exceeding 150,000, Appl. Phys. Lett. 90, 251109 (2007).

50. G. Lecamp, J. P. Hugonin, P. Lalanne, R. Braive, S. Varoutsis, S. Laurent, A. Lemaˆıtre, I. Sagnes, G. Patriarche, I. Robert-Philip, and I. Abram, Submicron-diameter semiconductor pillar microcavities with very high quality factors, Appl. Phys. Lett. 90, 091120 (2007).

51. J. P. Zhang, D.Y. Chu, S. L. Wu, W.G. Bi, R. C. Tiberio, R. M. Joseph, A. Taflove, C.W. Tu, and S. T. Ho, Nanofabrication of 1-D photonic bandgap structures along a photonic wire, IEEE Photonics Technol. Lett. 8, 491–93 (1996).

52. P. Velha, J. C. Rodier, P. Lalanne, J. P. Hugonin, D. Peyrade, and E. Hadji, Ultra-high-reflectivity photonic-bandgap mirrors in a ridge SOI waveguide, New J. Phys. 8, 204 (2006).

53. J. D. Joannopoulos, R. D. Meade, and J. N. Winn, Photonic Crystals (Princeton University Press, 1995).

54. Y. Akahane, T. Asano, B. S. Song, and S. Noda, High-Q photonic nanocavity in two-dimensional photonic crystal, Nature 425, 944–947 (2003).

55. E. Weidner, S. Combrie, N.V. Q. Tran, A. De Rossi, J. Nagle, S. Cassette, A. Talneau, and H. Benisty, Achievement of ultrahigh quality factors in GaAs photonic crystal membrane nanocavity, Appl. Phys. Lett. 89, 221104 (2006).

56. P. Velha, E. Picard, E. Hadji, J. C. Rodier, P. Lalanne, and D. Peyrade, Ultrahigh Q/V Fabry-Perot microcavity on SOI substrate, Opt. Express 15, 16090–16096 (2007).

57. A. R. Md Zain, N. P. Johnson, M. Sorel, and R. M. De La Rue, Ultra high quality factor one dimensional photonic crystal/photonic wire micro-cavities in silicon-on-insulator (SOI), Opt. Express 16, 12084–12089 (2008).

58. B. S. Song, S. Noda, T. Asano, and Y. Akahane, Ultrahigh-Q photonic double-heterostructure nanocavity, Nature Mater. 4, 207–210 (2005).

59. Y. Akahane, T. Asano, B. S. Song, and S. Noda, Fine tuned high-Q photonic-crystal, Opt. Express 13, 1202–1214 (2005).

60. T. Tanabe, M. Notomi, E. Kuramochi, A. Shinya, and H. Taniyama, Trapping and delaying photons for one nanosecond in an ultrasmall high-Q photonic crystal nanocavity, Nature Photonics 1, 49–52 (2007).

61. Kuramochi, E., Notomi, M., Mitsugi, S., Shinya, A. & Tanabe, T. "Ultrahigh-Q photonic crystal nanocavities realized by the local width modulation of a line defect", Applied Phys. Lett. 88, 041112 (2006).

62. Notomi M , Kuramochi E and Tanabe T," Large-scale arrays of ultrahigh-Q coupled nanocavities", NATURE Photonics, Vol: 2, Issue: 12, p.p741-747, December 2008

63. Kuramochi E, Taniyama H, Tanabe T, Shinya A and Notomi M," Ultrahigh-Q two-dimensional photonic crystal slab nano-cavities in very thin barriers" Applied Physics Letters, (93) 11, 111112, 15 September 2008 .

64. Yamamoto T, Notomi M, Taniyama H, Kuramochi E , Yoshikawa Y, Torii Y, Kuga T, "Design of a high-Q air-slot cavity based on a width-modulated line-defect in a photonic crystal slab", Optics Express, (16) 18   p.p: 13809-13817, 1 September 2008.

# CHAPTER 2: Simulation Techniques

Maxwell's equations are important for an understanding of light propagation in photonic crystals. They are central for the solution of electro-magnetic problems in dielectric media – for a variety of different length and dielectric scales, which are related to each other.

## 2.1 Photonic Crystals: The Theory

In photonic crystals, the famous Maxwell's equations are used to study light propagation in photonic crystal structure. The propagation of light in a medium is governed by the four well-known Maxwell's equations, written here in c.g.s units [1, 19-20]. The forms of the Maxwell equation are given by;

$$\nabla . B = 0 \qquad\qquad (1.1)$$

$$\nabla . D = 4\pi\rho \qquad\qquad (1.2)$$

$$\nabla \times E + \frac{1}{c}\left(\frac{\partial B}{\partial t}\right) = 0 \qquad\qquad (1.3)$$

$$\nabla \times H - \frac{1}{c}\left(\frac{\partial D}{\partial t}\right) = \frac{4\pi}{c}J \qquad\qquad (1.4)$$

or in mks/SI unit they can be written as;

$$\nabla . B = 0 \qquad\qquad (1.1a)$$

$$\nabla . D = \rho \qquad\qquad (1.2a)$$

$$\nabla \times E + \left(\frac{\partial B}{\partial t}\right) = 0 \qquad\qquad (1.3a)$$

$$\nabla \times H - \left(\frac{\partial D}{\partial t}\right) = J \qquad\qquad (1.4a)$$

Based on Joannopolous and Jackson [1, 19], equations 1.1 to 1.4 are given in cgs units whereas equation 1.1a to 1.4a are given in mks/SI units, where the physical quantities are given as:

$B$        - Magnetic flux density in Tesla, T

$D$        - Electric flux density in Coulombs per square m, C/m$^2$

$E$        - Electric field strength in Volt per meter, V/m

$H$        - Magnetic field strength in Ampere per meter, A/m

$\rho$        - Electric charge density in Coulombs per cubic meter, C/m$^3$

J        - Electric current density in Ampere per square meter, A/m$^2$

The detailed derivation of each counterpart of Maxwell's equations, is given by Jackson (1962) in the reference [19]. For propagation in mixed dielectric medium, $\rho$ and J are set to zero, since there are no free charges or currents in the homogeneous dielectric material. By assuming that the applied field strength is small and behave linearly, the dielectric flux density, D can be related to the electric field density by the power series of;

$$D_i = \sum_j \varepsilon_{ij} E_j + \sum_j k\chi_{ijk} E_j E_k + O(E^3) \qquad (1.5)$$

Since the electric field strength E (r,ω) and displacement field, D (r,ω) are related to the scalar dielectric constant of the microscopic and isotropic material ε (r,ω)- χ and the higher order term can be neglected. In low loss dielectric materials, ε (r) can be treated as purely real, thus producing the electric field density written as

$$D(r) = \varepsilon (r) E (r) \qquad (1.6)$$

In addition, for most dielectric material, the magnetic permeability, $\mu_r$ is approximately equal to 1, giving the magnetic flux density, B equal to the magnetic field strength, H. The flux density of the dielectric material can be written as D = ε.E where the permittivity, ε is real. Therefore the Maxwell equation can be re-written as already illustrated in [1, 19] as;

$$\nabla . H(r,t) = 0 \qquad (1.7)$$

$$\nabla . \varepsilon(r) E(r,t) = 0 \qquad (1.8)$$

$$\nabla \times E(r,t) + \frac{1}{c}\left(\frac{\partial H(r,t)}{\partial t}\right) = 0 \qquad (1.9)$$

$$\nabla \times H(r,t) - \frac{\varepsilon(r)}{c}\left(\frac{\partial E(r,t)}{\partial t}\right) = 0 \qquad (1.10)$$

Then the harmonic mode of the E and H fields components propagating in the dielectric medium are considered as;

$$H(r,t) = H(r)e^{i\omega t} \qquad = 0 \qquad (1.11)$$

And $\qquad E(r,t) = E(r)e^{i\omega t} \qquad = 0 \qquad (1.12)$

By substituting Eq. (1.11 and 1.12) into the Maxwell equations (1.7 to 1.10), the equation for the mode profiles of a given frequency is reduced to a simple condition (two divergences) as shown below-;

$$\nabla.H(r) = \nabla.D(r) = 0 \qquad (1.13)$$

Where H(r) and E(r) and the field components at t=0. By deriving equation 1.11 and 1.12 and substituting it into *equation 1.9 and 1.10*, the Maxwell equation will become;

$$\nabla \times \left( \frac{1}{\varepsilon(r)} \nabla \times H(r) \right) = \left( \frac{\omega}{c} \right)^2 H(r) \qquad (1.14)$$

Thus *equation 1.14* derived, only has H components which become a master equation for dielectric medium, in particular photonic crystal with only magnetic field, H(r) component. This can also be used to recover an electric field component, E(r) of the Maxwell equation given by;

$$E(r) = \left[ \frac{-ic}{\omega\varepsilon(r)} \right] \nabla x H(r) \qquad (1.15)$$

The final equations given above (*1.14 and 1.15*) are only used primarily to understand the basic concepts of photonic crystal (PhC) structures. These concepts can also be used for more complex structures such as 2D and 3D PhCs. In this present work, only 1D photonic crystal structures consisting of a single row of holes embedded in a narrow photonic wire will be explored in depth, as will be described in *Chapter 3*.

## 2.2 PhC/PhW micro-cavities

PhC micro-cavities embedded in narrow photonic wire have been widely studied. A small shift in the periodic mirrors - in particular one situated in the middle of the periodic mirror - will produce a sharp resonance peak in the middle of stop band. This resonant condition oscillates naturally at certain frequencies with greater amplitudes than others within the system. The *Q*-factor is particularly useful in determining the qualitative behaviour of a system. For some telecoms applications, such as dense

wavelength division multiplexing (DWDM), the performance of those resonances is determined by their Quality factors and optical transmission at a certain resonance frequency. The Quality factor of a system is a dimensionless parameter that defines the first order behaviour, for the decay, of an oscillating frequency within a micro-cavity. It is characterised by the ratio of the resonant frequency to the bandwidth of the resonance or by the decrease in the amplitude of the wave propagating through a system, within an oscillation period. Equivalently, it compares the frequency at which the system oscillates to the rate of energy dissipated by the system. A higher *Q-factor* value indicates a lower rate of energy dissipation relative to the oscillation frequency, so the oscillations die out more slowly. For example, a pendulum suspended from a high-quality bearing, oscillating in air, would have a high *Q*, while a pendulum immersed in oil would have a low one. In optics, the Q-factor is generally given by [2-3]:

$$Q = \frac{2\pi f_0 E}{P}$$

Where E is the stored energy in the cavity and P is the power dissipated within the cavity, given by;

$$P = -\frac{dE}{dt}$$

The *Q*-factor is equal to the ratio of the resonant frequency to the bandwidth of the cavity resonance shown in *Fig.2.1*.
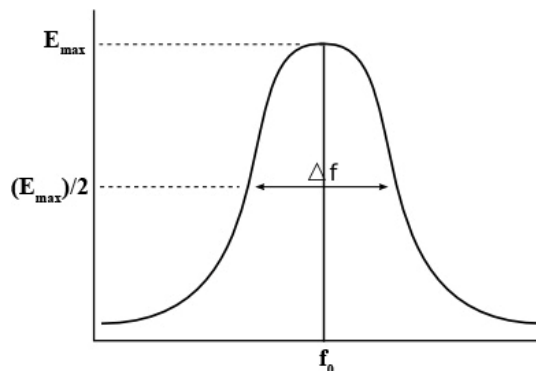


**Fig.2.1**: *A typical resonance frequency resulted from micro-cavity structures defined by the central resonance frequency, f₀ and the bandwidth of the frequency at 3 dB points (energy at the steady state condition)*

Ideally, the average lifetime of a resonant photon in the cavity is proportional to the cavity's $Q$. Resonant systems respond to frequencies close to their natural frequency much more strongly than they respond to other frequencies. A system with a high $Q$ resonates with greater amplitude (at the resonant frequency) than one with a low $Q$ factor, and its response falls off more rapidly as the frequency moves away from resonance. Therefore the physical interpretation of resonance is given by its general equation;

$$Q = \frac{f_0}{\Delta f}$$

Where $f_0$ is the central frequency of the resonance and $\Delta f$ is the frequency difference within at 3 dB points or ½ of the total energy stored in the micro-cavity system. In this present work, several different types of resonator have been studied, namely waveguide Bragg gratings and 1D PhC/PhW waveguides – as shown in *Fig.2.2*. Unlike the Bragg grating waveguide [4], which has a rectangular recess embedded on a photonic wire waveguide, a single row of holes is used as a set of mirrors.

This structure consists of a single row of holes drilled in the 500 nm width of wire waveguides. Those holes acted as a periodic mirror where light impinging on the PhC bounced back provide a band gap where light is forbidden to propagate at certain frequency. A spacer was introduced symmetrically between the periodic mirrors - thus producing a narrow resonance in the transmission. The concepts for this kind of structure were proposed by Krauss and Foresi [5,18]. But the Q-factor at this [5] resonance condition obtained was small (~500). The PhC hole mirrors resulted in a wide stop band (approximately 182 nm), using eight PhC mirrors holes, whereas 32 period waveguide Bragg gratings were used and showed a narrower stop band of approximately 88 nm. This difference is due to the fact that the light was coupled more strongly in the periodic hole mirrors – where 95% of the light was reflected with the periodic hole arrangement, as compared to the waveguide Bragg gratings where ~ 82% light was reflected back. Hole gratings show more pronounce stop bands compared to their counterpart. As mentioned before, stronger reflection was observed for the hole grating. The hole gratings have a bigger stop-band of approximately 180 nm, which is useful for some filter designs and some optical communications applications. This wide stop-band may be compared with the limited bandwidth of the

stop band of the may be contrasted with the significantly smaller stop-band of the rectangular recess grating.
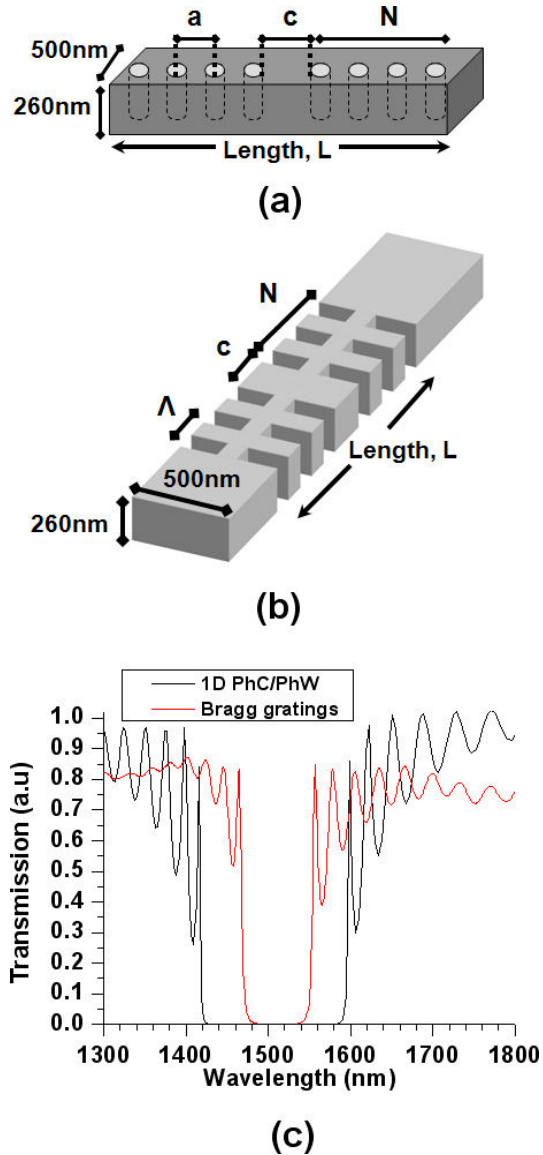


**Fig.2.2**: *Different types of PhW waveguides micro-cavity (a) 1D PhC/PhW waveguides with cavity length (distance between two hole edges of the hole spacer) c, hole periodic spacing (distance between centre-to-centre hole), a and Number of periodic holes, N (b) PhW Bragg Gratings waveguides with cavity length, c, period, Λ and Number of recess period, N - and (c) Transmission spectra of Bragg Grating waveguides and 1D PhC/PhW*

In addition, for this grating condition, the total length, L of the waveguide Bragg grating of ~11 μm is longer by a factor of four in order to achieve a practical stop-band spectrum, as compared with the hole gratings structures (~3 μm). The present work will demonstrate the design, fabrication and characterisation of the 1D PhC based micro-cavity, which is potentially useful for wavelength division multiplexing (WDM) in PhC devices. A single row of PhC holes is embedded in a narrow photonic wire waveguide to allow sufficient optical coupling for integration with other photonic devices. This thesis will address the importance of using a combination of hole tapering with a different hole diameter at the interface between the un-patterned wire and the cavity mirror, as well into the micro-cavity region - in order to achieve large optical transmission together with a high resonance Q-factor value. Achieving high Q-factor together with large optical transmission remains asignificant challenge. The key points towards designing an ultra high Q-factor device that confines light in such a small volume lie in reducing the modal mismatch between the un-patterned wire and the PhC or grating sections. Therefore, designing a tapered structure to reduce the modal mismatch at the interfaces between the mirror region and the PhW waveguide sections is necessary. One of the approaches used to overcoming this situations is the use of a taper structure consisting of holes with different sizes through progressive increase of the hole size into the mirror region [6]. On the other hand, the same model has also been used with short taper sections incorporated into a 1D micro-cavity based system [7]. Using these concepts, the impact of progressive tapering using different hole diameters has shown a huge improvement in enhancing the quality-factor of the micro-cavity [8, 9].

Therefore, 1D PhC/PhW micro-cavities can provide higher optical confinement in smaller volumes that are closer to the theoretical value of $0.055 \, (\lambda/n)^3$ [8] - which has a great potential in high index contrast materials such as silicon-on-insulator (SOI) to be used in some telecommunication applications such as DWDM, add-drop filter switching experiments, slow light and non-linear optics.

## 2.3 The Finite-Difference Time-Domain (FDTD) approach

There have been several methods used for computational purposes, especially for modelling photonic crystal structures and photonic wire waveguides. The Finite

Difference Time Domain (FDTD) approach is a commonly used technique because it provides both the spatial and temporal properties of the structure with a single calculation, making it suitable for the analysis of many structures. However it requires a lot of time to compute a single run. This technique uses the famous Maxwell's equations based on the Yee mesh [10], published in 1966. Yee has proposed this technique in order to derive a numerical scattering problem and electromagnetic absorption on the basis of Maxwell's equations. The computational domain was first established, in order to determine the physical region within which the calculation will be performed. The Electric field, E, and the magnetic field, H, are distinguished at every point within the domain by specifying the material used at each domain point *(in xyz directions)*. The materials involved could be free space (air), metal or dielectric material. A light source in the form of a plane wave is then impinging on the chosen material. Later in 1994, the technique called the Perfectly Matched Layer (PML) boundary condition was introduced [11]. It was used as an absorption mechanism for electromagnetic waves incident on the edge of the computational domain in space. The FDTD method can be implemented in either 2D or 3D computations - but it requires a lot of memory and power consumption for a single computational run, especially for a large device in 3-D. 2D FDTD reduce time and memory requirement significantly. It employs a refractive index approximation or average refractive index of the slab- called effective index method (EIM). By using this method, the cross sectional index profile is usually transformed to the one dimensional index profile by using EIM [12, 13]. In the EIM approach, the eigenvalue of the equivalent slab waveguide is an approximate index value of the original waveguide. Although the EIM approach provides a good approximation, it still suffers from errors in the vicinity of the cut-off [14-17]. At the beginning of this present work, this method is used to investigate the preliminary behaviour of the device with the assumption that losses are negligible. In order to reduce simulation time and power consumption 2D FDTD approach was initially used throughout the course to analyse the general optical behaviour of the device structures- implementing EIM. Since EIM is only an approximation of the actual refractive index obtained by taking into account the whole ridge waveguide structures – at least a small discrepancy between the simulations measured results is very much to be expected. On the other

hand, the 3D FDTD method can give a better estimate of the properties, although it is time and power consuming, which is still a major concern.

During this present work, different types of commercial software have been used. The Fullwave RSoft computational software has been used at the beginning of this work, where only 2D computation was deeply explored due to the longer time and high power consumption for 3D FDTD. Based on the concept proposed by Yee [10], several key pieces of information are needed to solve the basic propagation problem in optical waveguide which comprised of:

- The refractive index distribution, n(x,y,z)
- Electromagnetic field excitation (Plane wave or Gaussian)
- Finite Computational domain in x,y and z direction)
- The boundary of PML layer
- Spatial grid size, $\Delta x$ and $\Delta y$
- Time step, $\Delta t$ ad the total length of the simulation time.

For 2D FDTD computation, the average refractive index, n or effective index, $n_{eff}$ of the slab waveguide of a material is used rather than the actual refractive of that particular material. This can be obtained using mode-matching method available in the Fimm-wave® commercial software by Photon Design®. This method includes the approximation of refractive index in both propagation direction of vertical and horizontal confinement of the slab waveguide. The transverse section of the device is first simulated using Fimm-wave® simulation tools. It shows the intensity of light in guiding mode, confinement of light inside the slab and the effective index, $n_{eff}$. It also shows the leaky region where light is not confined inside the slab. *Fig.2.3* shows the contour plot of the TE fundamental mode of the waveguide. It shows the intensity of light confinement along the core at 1.52 μm wavelength at different etching depth.
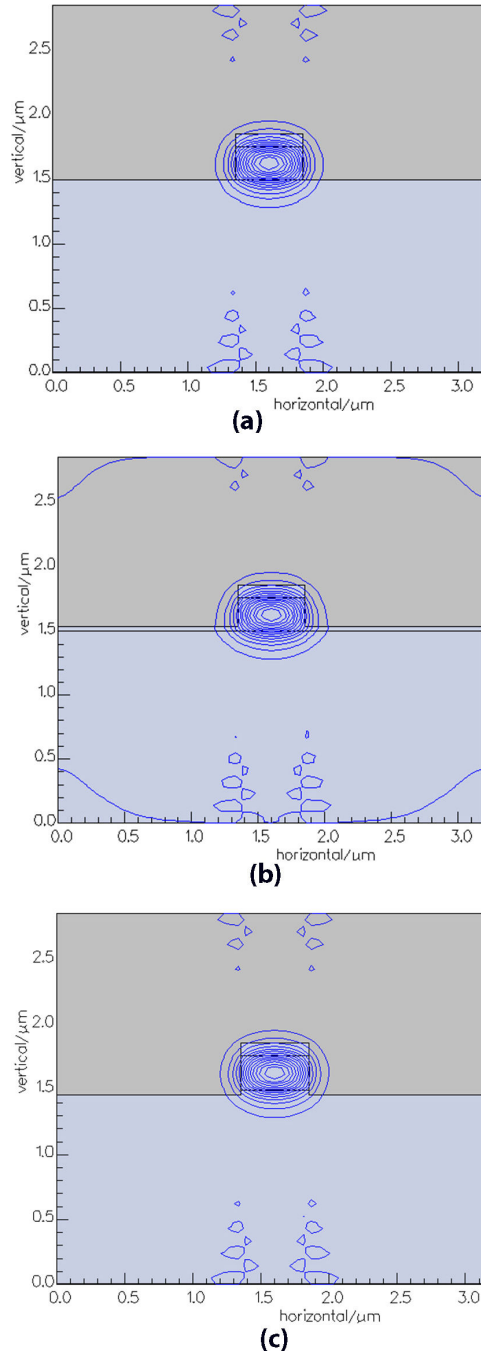
**Fig.2.3**: *Contour plot of the TE fundamental mode intensity (a) fully etched (b) shallow etched (c) deep etched*

It is suggested that the different etching depth will give rise to the abrupt change of the effective index, $n_{eff}$ at the boundary of silicon core and silica cladding (lower cladding) where some of the light are reflected back into the cladding (back scattering). This can be improved by etching slightly deeper into the lower cladding by around 20 nm-40 nm, thus reducing scattering losses.
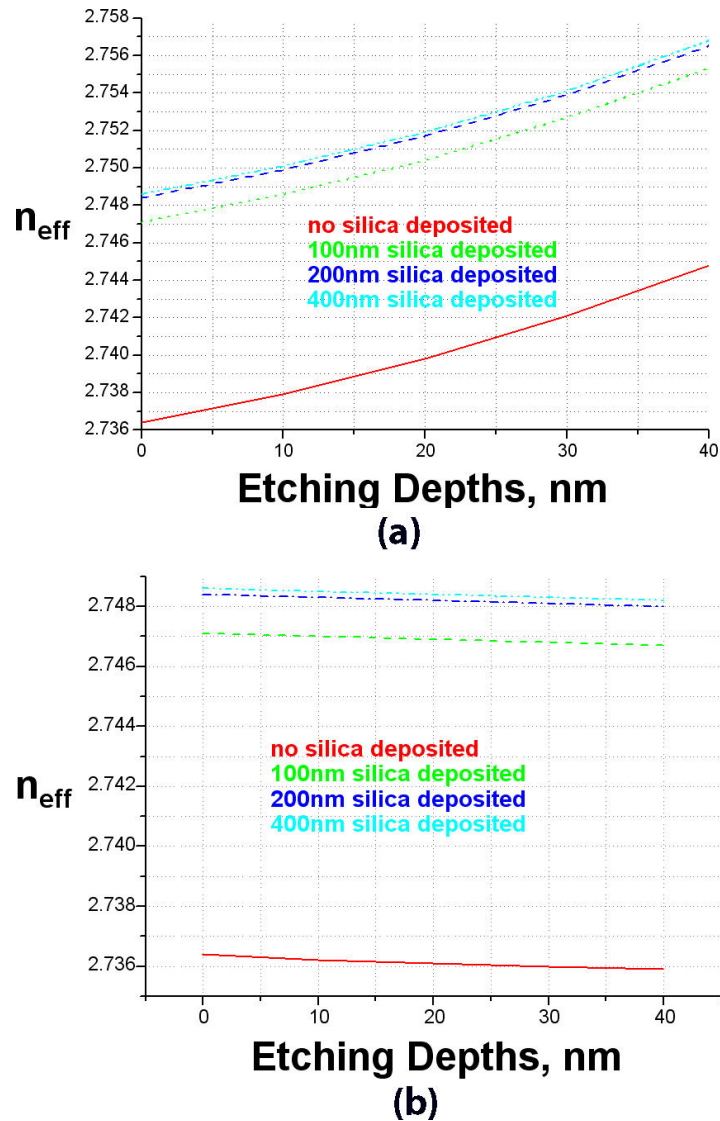
**Fig.2.4**: *The effective index, $n_{eff}$ at different etching depth for symmetric(silica deposition on top) and asymmetric waveguide(no silica deposition)- (a) shallow etched (b) deep etched*

The effective index calculated using the Fimm-wave™ simulation tool for 500 nm wide ridge waveguides at different etching depth is given in *Fig.2.4 (a) and (b)*. More profound field intensity is obtained for fully etched silicon where symmetric field distribution is obtained (*see Fig.2.3 (a)*) as compared to shallow and deep etched Silicon. Depositing Silica on top of the photonic wire can also improves the confinement of TE fundamental mode of the photonic wire significantly. From

*Fig.2.4*, 100 nm, 200 nm and 400 nm $SiO_2$ has been deposited on the photonic wire. But to reduce the device preparation complexity and process development, the slab waveguide design based on fully etched silicon is considered through out this work. By using Fimm-wave simulation tools, the calculated effective index $n_{eff}$ based on the design used for this present work is 2.97- which will be used for 2D FDTD computation. The value of $n_{eff}$ is fed into the Full-wave simulation tool by using either pulsed or continuous Gaussian source for slab waveguide. The finite computational domain is optimized in space which covering the area between 10 to 20 µm in length and 2 µm in width since large computational area will contribute to a longer simulation time and also consume more memory and power. The space must be exactly proportional to the size of the optical waveguide. The thickness of PML required for the device operating at around 1.52 µm wavelength is 0.5 µm to provide better electromagnetic wave absorption at the boundary. Other parameters that contribute to the accuracy of the simulation are determined by the choice of the spatial grid or mesh size, where smaller grid spacing gave more accurate computation. In other word, the closer the resolution in simulation to the actual device more accurate simulation will be established. In this present work, the grid size of 0.01 µm was used.
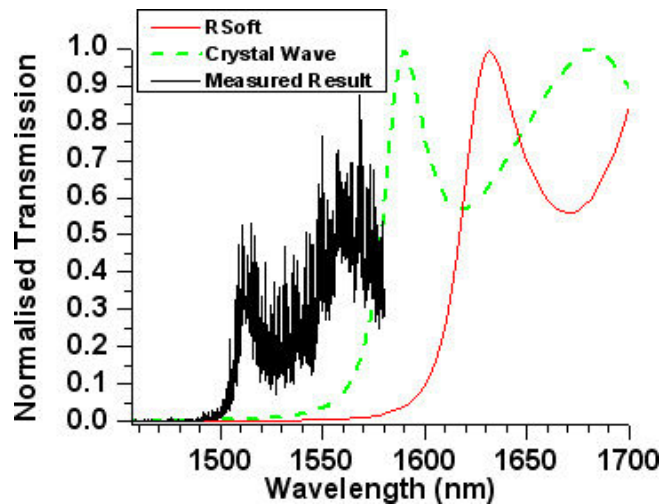


**Fig.2.5**: *An example showing a comparison between 2D FDTD computed using different simulations tools (R-soft and Crystal-wave) with the measured result*

During the second half of the computational process, the author has used Crystal Wave by Photon Design to compute all the device structures. This software is found

to be more accurate as compared to the Full-wave simulation tool. On the other hand, by using the same parameters in the Crystal Wave tool as previously used in Full-wave, the simulation time has been reduced by a factor of five and the result obtained is closer to the measured result as shown in one of the example in *Fig.2.5*. The comparison is made by using 12 period 1D PhC mirrors with diameters of 350 nm and periodic spacing of 360 nm. By looking at the band edge location of the measured result in figure 6, the 2D FDTD crystal wave shows closer result (band edge) as compared to the one computed using R-soft tools where the deviation of 83 nm is observed between the simulation and the measured result. But this is understood to be due to small deviation in the dimension of the structures produced after fabrication process as real devices. No further investigation is made in reference to the discrepancy between the different examples of commercial software, but the problem has been addressed to the relevant personnel. As a result, based on further tests carried out using different measurement run to compare the results with the simulation, the Crystal Wave software have been chosen as the relevance tools that are well-suited to the design structures used throughout this present work.
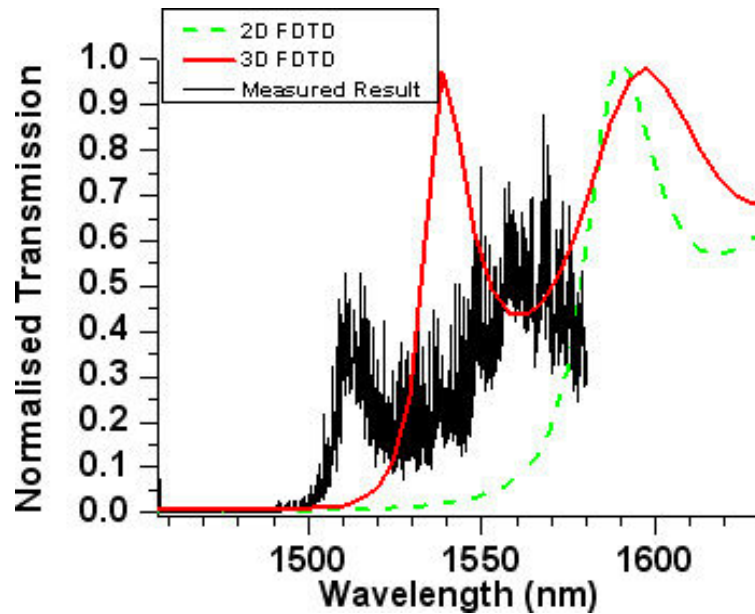


**Fig.2.6**: *An example showing a comparison between 2D and 3D FDTD simulation using the Crystal Wave simulation tool and compared also with the measured result.*

On the other hand, the 3D FDTD approach has been used occasionally to simulate the devices using the Crystal-Wave simulation tool. It produces a spectrum that is closer to the measurement result, as compared to estimation based on the 2D FDTD approach. *Fig.2.6* shows an example that compares the 2D and 3D FDTD approach based on the Crystal-Wave software, as well as with measurement results. A smaller deviation, of approximately 30 nm, in the location of the band-edge between the 3D FDTD and measured results is observed, as compared to the 83 nm difference found using the 2D FDTD approach. The difference between the 3D FDTD and the measurement results is partly due to the difference between the dimensions of the device structures (hole diameters, wire width and hole periodic spacing) simulated and the dimensions of the actual device fabricated. This problem will be discussed further in the next subsequent Chapters (*Chapter 4 and 5*).
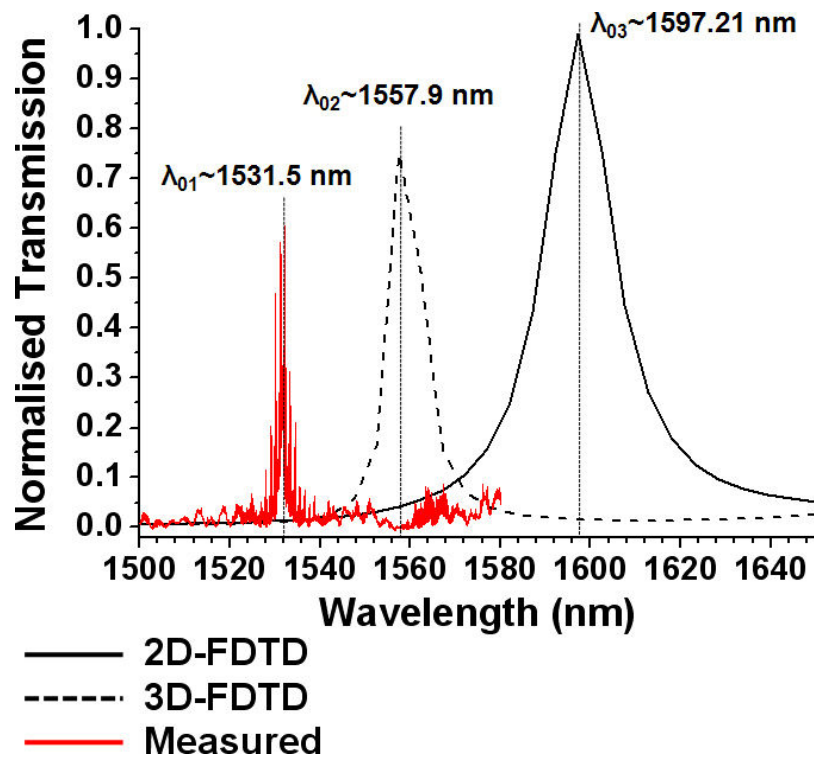


**Fig.2.7***: Another example showing a comparison between 2D and 3D FDTD simulation using the Crystal Wave simulation tool with the measured result for PhC/PhW micro-cavities.*

Another comparison has been made for the case with the micro-cavity spacer inserted between periodic mirrors. A sharp resonance was excited at around the middle of the

stop band. *Fig.2.7* shows an example of a resonance excited within the stop band. 3D FDTD approach shows closer location of the stop band at the resonance central wavelength ($\lambda_{02}$) of 1557.9 nm to the measured result which is at $\lambda_{01}$ of 1531.5 nm. Whereas 2D FDTD has a resonance which lies further at the higher wavelength region of $\lambda_{03}$=1597.21 nm. But the time taken to simulate this device structures using 3D FDTD approach is several time longer than that of 2D FDTD approach.

In summary, the 2D simulation approach is used to produce preliminary designs for the device, together with the employment of an effective index approximation based on the waveguide properties of the base material structure discussed earlier. 2D simulation helps with obtaining a better understanding of the general behavior of the device - but 3D simulation gives more accurate prediction of the results, at the expense of much greater time and energy consumption. Throughout the present work, both 2D and 3D FDTD simulations were carried out using the commercial software called Crystal-Wave ® from Photon Design.

**References:**

1.  J.D.Joannopolous, R.D.Meade and J.N.Winn,"Photonic crystals: Molding the flow of light", Princeton University Press, 1995.

2.  Roger George Jackson (2004). *Novel Sensors and Sensing*. CRC Press. ISBN 075030989X., p.28

3.  Benjamin Crowell (2006). "Vibrations and Waves". *Light and Matter online text series*., Ch.2

4.  M. Gnan, G. Bellanca, H.M.H. Chong, P. Bassi, and R. M. De La Rue, "Modelling of photonic wire Bragg gratings," *Optical and Quantum Electronics*, vol. 38, no. 1-3, pp. 133–148, 2006.

5.  J. S. Foresi, P. R. Villeneuve, J. Ferrera, E. R. Thoen, G. Steinmeyer, S. Fan, J. D. Joannopoulos, L. C. Kimerling, Henry I. Smith & E. P. Ippen, "Photonic-bandgap microcavities in optical waveguides," *Nature* **390**, 143 (1997)

6.  Ph. Lalanne and A. Talneau, "Modal conversion with artificial materials for photonic-crystal waveguides," *Optics Express*, **10**, 354-359, 2002.

7.  D. Peyrade, E. Silberstein, Ph. Lalanne, A. Talneau and Y. Chen, "Short Bragg mirrors with adiabatic modal conversion," *Applied Physics Letters*, **81**, 829-831, 2002.

8.  P. Velha, J. C. Rodier, P. Lalanne, J. P. Hugonin, D. Peyrade, E. Picard, T. Charvolin, and E. Hadji, "Ultra high reflectivity photonic bandgap mirrors in a ridge SOI waveguide," *New J. Phys. (IOP)*, vol. 8, no. 204, pp. 1–13, Sep. 2006.

9.  P. Lalanne and J. P. Hugonin, "Bloch-wave engineering for high-Q, small-V microcavities," *IEEE J. Quantum Electron.*, vol. 39, no. 11, pp. 1430–1438, Nov. 2003.

10. K. S. Yee, "Numerical solution of initial boundary value problems involving Maxwell's equations in isotropic media," *IEEE Trans. on Antennas and propagation*, 14, 302-307, 1966.

11. J. P. Berenger, "A perfectly matched layer for the absorption of electromagnetic waves," *J. Computational Physics*, **114**, No. 2, 185-200, 1994.

12. J. Buus," The effective index method and its application to semiconductor lasers", *IEEE J. Quantum Electron.*, vol. 18, no. 7, July, 1982 , pp. 1083-1089.

13. Y. Chung and N. Dagli, "An Assessment of Finite Difference Beam Propagation Method," *IEEE J. Quantum Electron*., vol. 26, no. 8, Aug. 1990, pp. 1335-1339.

14. Y.H. Cheng and W.G. Lin, "Investigation of Rectangular Dielectric Waveguides: An Iteratively Equivalent Index Method," *IEE Proceedings*, vol. 137, no. 5, Oct. 1990, pp. 323-329.

15. H. Furuta, H. Noda, and A. Ihaya, "Novel Optical Waveguide for Integrated Optics," *Appl. Optics,* vol. 13, 1974, pp. 323-326.

16. A. Kumar, K. Thyayarajan, and A.K. Ghatak, "Analysis of Rectangular Core Dielectric Waveguide: An Accurate Perturbation Approach," *Opt. Letters*., vol. 8, Jan. 1983, pp. 63-65.

17. C.M. Kim, B.G. Jung, and C.W. Lee, "Analysis of Dielectric Rectangular Waveguide by Modified Effective Index Method," *Electronic Lett*ers, vol. 22, no. 6, Mar. 1986, pp. 296-298.

18. T.F. Krauss, B. Vögele, C.R. Stanley and R.M. De La Rue, "Waveguide micro-cavity based on photonic microstructures", *IEEE Photonics Technology Letters*, **9**, pp.176-178, Feb (1997).

19. Jackson, J. D. (1962) *Classical Electrodynamics*. New York: John Wiley.

20. Jackson, J. D. *Classical Electrodynamics, 3rd ed.* New York: Wiley, p. 177, 1998.

# CHAPTER 3:

# Fabrication Processes

**Introduction**

This chapter will emphasize one of the most important parts of the thesis, which is silicon fabrication processes. Almost a quarter of the time has been dedicated to optimizing the fabrication processes, in order to improve the performance of the devices. Most of the optimization has been carried out based on previous work [14-16]. This chapter contains a description of the material used - silicon-on-insulator (SOI), the pattern transfer process (including electron beam lithography and photolithography techniques) and characterization of the device structures. It also underlines the etching processes used - i.e. dry etching techniques, mainly reactive ion etching (RIE), and wet chemical etching for SOI.

**3.1        Silicon Technology**

The silicon industry has evolved rapidly ever since it's beginning. Silicon is the base material used for many electronics applications, such as microprocessors and integrated circuits (IC). It is also the commonly used material for research and development in many CMOS technologies [1-5]. The use of silicon in photonics has evolved into a mature device technology for many applications - such as optical sensors, modulators, optical switching and non-linear optics. Silicon-on-insulator based material has became the choice for many integrated circuits (IC), due to its low losses and higher speed operation, leading to lower power consumption and increased overall chip performance. The silicon-on-insulator (SOI) wafer material is formed by a silicon layer with a silica cladding underneath the silicon core. The silica cladding

acts as a buffer layer to separate the mono-crystalline silicon device layer from the sub-micron silicon substrate. The fabrication process for silicon based photonic devices is relatively easy and straightforward, as compared to active devices such as those typically realized in complex III-V semiconductor hetero-epitaxial structure. For example, the III-V hetero-structure semiconductor material typically has several different layers with different compositions, which make it less easy to control in fabrication processes. Each layer requires a high precision pattern transfer process in order to define the correct pattern in the material. In other words, in some cases the III-V semiconductor device structure requires multi-level etching, which makes it more difficult to obtain a precise fabrication outcome. In addition, the different compositions of each layer of III-V semiconductor also imply different etch rates, resulting in irregular etching, which in turn affects verticality and the aspect ratio of the features patterned into the material. In contrast, Silicon on-Insulator is a passive material that consists of a silicon guiding layer with a silica cladding layer as a buffer underneath it. This arrangement gives freedom in term of fabrication processes, where one can control the etching process easily due to the basically simple nature of the silicon. The silicon guiding layer normally requires single-step etching, resulting in good controllability of the etching rate - using the correct choice of the mask resists to define the guiding layer. The high potential of silicon-on-insulator based material has been recognized some time ago in the worlds of optoelectronics and photonics. Its capability for giving reduced propagation losses has become a benchmark in the progress towards developing a single device with more functionality, due to the high index contrast and large wavelength windows, extending over wide range of optical frequency. In addition, SOI also enables the use of the mature metal-oxide semiconductor processing technology that gives large scale and monolithic optoelectronic integration. In other words, there are possibilities for SOI to be a platform for integrating multifunctional devices such as optical switches and sensors into a single chip. Reduction towards sub-micrometer size in the waveguide dimensions also provides a new platform for other optical functions, such as optical amplification and wavelength conversion. Development of the tight optical confinement also leads to easier access to the non-linear properties of the material at low pump power levels. On the other hand, for advanced SOI technology, integration of many optoelectronics devices on single chips must demonstrate a capability for

delivering full device functionality. In addition, the high index contrast of SOI, which is given by the refractive index of the silicon guiding layer of 3.45 and the 1.45 index value of the silica cladding of 1.45, provides strong confinement for the optical propagation through the guiding layer. Photonic wires beat photonic crystal channel guides mainly because they are intrinsically simpler and more regular. The strong optical confinement makes photonic wire waveguides suitable for more complex designs, such as sharp bends [6,7] and Mach Zehnder (MZ) structures [8]. The emergence of state-of-the-art fabrication tools, especially for SOI based material at the sub-nano-metre scale, has also motivated much research toward improving the fabrication process - thus producing low propagation loss device structures.

## 3.2        Silicon-On-Insulator (SOI) material

The Silicon-on-Insulator (SOI) material used for this projectwas provided by SOITEC- one of the leading commercial Silicon manufacturing companies. There are several types of Silicon technology available in the current market - such as UNIBOND ® [9, 10] and SIMOX ® [11]. The Silicon used for this project was UNIBOND® type material prepared using the 'SMART-CUT' technology developed by SOITEC [52].
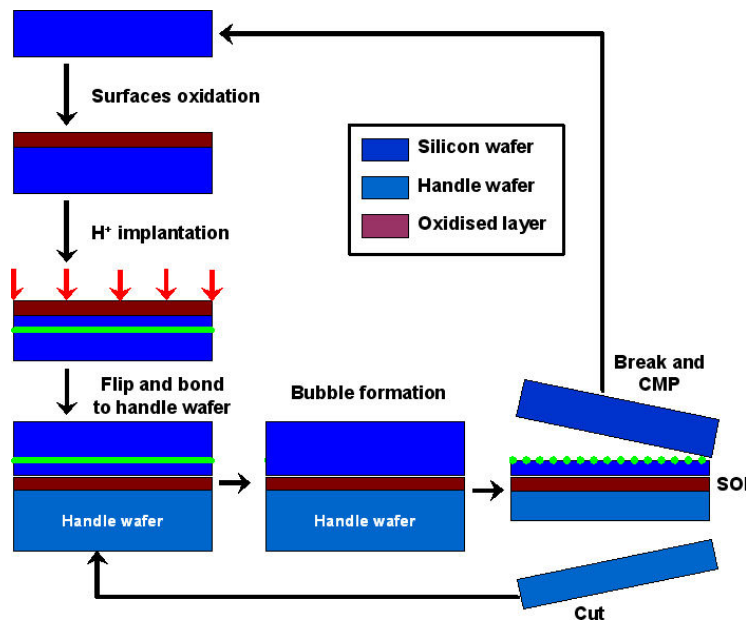


**Fig.3.1**: *SOI produced using smart cut (a) technique*

This technology is based on the wafer bonding techniques created through hydrogen implantation via protons. The SMART CUT process is divided into several steps, as

shown in *Fig.3.1*. Detailed descriptions of the process can be found in [12, 13] and references therein. The steps to produce SOI material using this method can be divided into several phases.

Step 1: Sample preparation and thermal oxidation process

The initial process of SOI sample preparation starts by growing $SiO_2$ (silicon dioxide) on the bulk silicon wafer. The $SiO_2$ buried layer (sometimes called the Bulk Oxide (BOX) layer) is used, in optical waveguides, to provide optical isolation between the Silicon core and bulk silicon underneath it.

Step 2: Hydrogen Implantation

This step includes the fracturing process that determines the thickness of the silicon layer in SOI. This process involves hydrogen implantation through the silica layer and silicon layer.

Step 3: Cleaning and Bonding process

Through the bonding process, the wafer is flipped over to be bonded onto a cleaned silicon wafer (the handle wafer). This process will form an $SiO_2$ layer sandwiched between two bulk silicon sections that will determine the thickness of the silicon guiding layer at a later stage.

Step 4: Splitting the Bonding with the 'handle' wafer

The process is initially carried out by fracturing the bonding wafer at 400-600$^o$C. At this point, a thin layer of mono-crystalline silicon remains bonded to the bulk silicon wafer, thus forming the SOI structure. Finally, in order to strengthen the chemical bonding of the SOI wafer, it is raised to a temperature of 1100$^o$C. The remainder of the silicon that has been split off can be used again for the next SMART-CUT process.
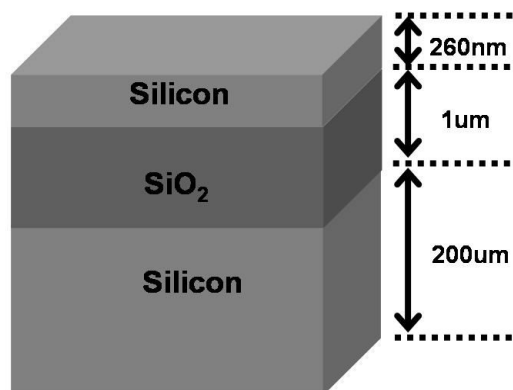


**Fig.3.2***: Cross sectional SOI wafer used in this present work*

The silicon-on-insulator (SOI) used for this present work consists of a silicon guiding layer with a nominal thickness of 260 nm and a silica buffer layer/cladding of 1 μm thickness - which are sandwiched between the silicon guiding layer and approximately 250 μm thick bulk silicon substrate, after undergoing thinning process on the bulk silicon as shown in the schematic drawing of *Fig.3.2*. The initial thickness of the bulk silicon layer when first delivered by the manufacturer, i.e. SOITEC was 700 μm. The final thinning process was carried out 'in-house' on the SOI substrates by mechanically polishing the 'bottom' bulk silicon substrate, in order to reduce the wafer thickness from 700 μm to a nominal thickness of between 250 and 300 nm. This thinning process is important for the subsequent precision cleaving process – producing the 'flat' end-facets on the sample that are required for efficient coupling in device characterization.

## 3.3 Fabrication Sequences

The development of the fabrication process for the photonic wires and photonic crystal device structures plays an important role towards the accomplishment of fabricated device structures that can be translated into a substantial agreement between the simulation and measurement outcomes. Different process cycles have been developed in line with the most current technology that became available during the project time-scale.
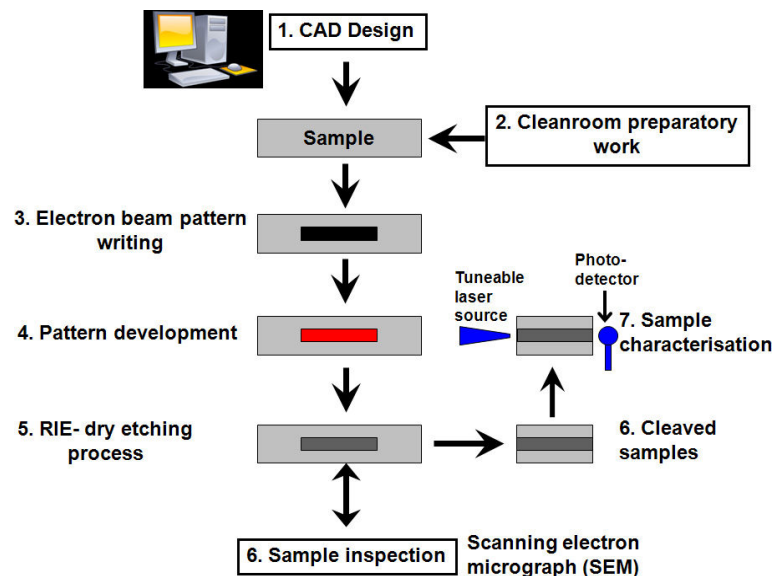


**Fig.3.3**: *General device fabrication cycles*

These cycles were optimized on the basis of previous work carried out by co-workers [14-16] - resulting in improvements towards near-perfect device structures, especially for the PhW/PhC waveguide devices used for this present work. The optimization of the SOI fabrication method was motivated by the need for producing low-loss silicon waveguides with reduced sidewall roughness. The first fabrication cycles were carried out by using PECVD (Plasma Enhanced Chemical Vapour Deposition) silica as a mask, before defining the silicon guiding layer - which involved a two-step silicon etching process. Further improvements on the end fabrication results of the device structures have been made by reducing the whole fabrication process to just a single-step silicon etching process, using stronger and more robust resist as a mask – i.e. HSQ (hydrogen silsesquoiaxane). The patterned and developed HSQ layer has been used as a mask layer in the etching of the silicon layer directly, without the need for an additional mask layer - thus reducing overall fabrication time and complexity. The reduction in the number of steps used for the silicon etching has been shown to improve the overall optical performance of the device, with reduced propagation losses that corresponded to a high quality fabrication outcome. These issues will be discussed in detail in a later section. A comparison will be made here between the two fabrications cycles used towards optimizing the devices during this present work.
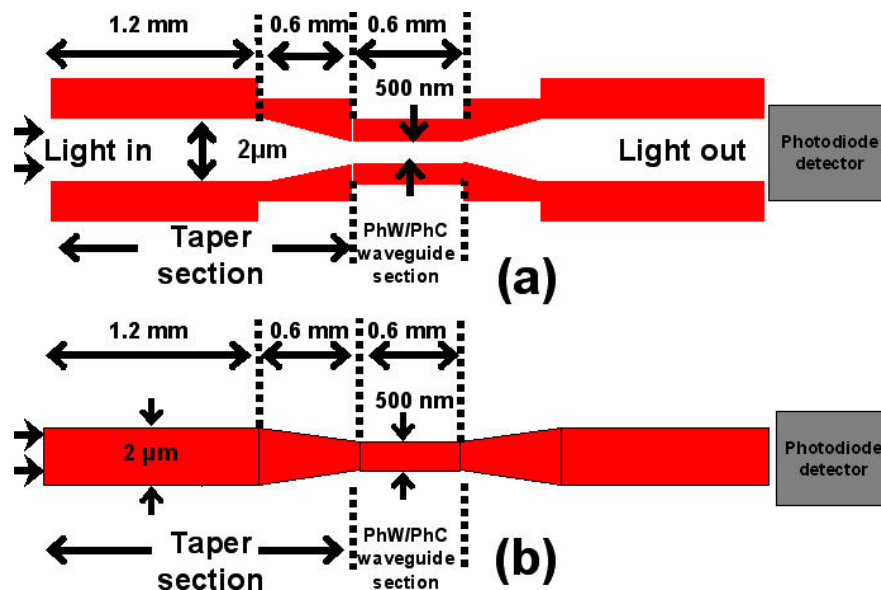


**Fig.3.4**: *L-Edit layout for the design of PhC/PhW device structures (not in scale) using (a) positive tone resist (b) negative tone resist*

A complete process cycle - including modelling, fabrication and characterization of PhW/PhC device structures is illustrated in *Fig.3.3*. The structures were first designed using a user-friendly Computer Aided Design (CAD) system tool – L-Edit version 12.3. The design file is then fractured in Computer Aided Transcription System (CATS) software that processes the GDSII (Graphite Data System II) file format. The GDSII is a binary file format representing planar geometric shapes, text labels, and some other information – which are arranged in hierarchical form. The objects are grouped by numeric attributes assigned to them, including the layer number or data type. While these attributes are designed to correspond to the "layers of material" used in manufacturing an integrated circuit, their meaning rapidly becomes more abstract, to reflect the way that the physical layout is designed. Afterwards, clean-room preparatory work was carried out – which concerned cleaning and defining the mask layer on the SOI samples for pattern transfer using electron-beam lithography (EBL). After the pattern writing process, the patterned resist was developed using active developers that react to any particular resists used, before the silicon waveguide was finally defined using dry-etch processing. The etched waveguides were then cleaved for device characterization using a tuneable laser operating at around band C (1550 μm) in the infra-red regime. Before the characterization process, it is useful to check the final etched waveguide using a scanning electron microscope (SEM) that is capable of capturing images of very small features - for further analysis of the sidewall roughness. The total size of the pattern size is partly determined by the field size of the VB6 EBL tool, in order to reduce the impact of stitching errors where the writing field boundaries will be placed over a wide waveguide. On the other hand, the length of the feeder waveguide must be longer than 1.2 mm, in order to allow moderate precision cleaving of the samples. Normally, such patterns were designed to be around 5 mm to 8 mm in length, in order to give extra freedom during cleaving. The combination of a taper section and a waveguide section was designed to be 1.2 mm long, which is sufficient for extinction of higher order modes coming from the feeder waveguide.

### 3.3.1        CATS design

The pattern layouts of the photonic wire/photonic crystal devices were designed using the commercial software L-Edit v.12 by Tanner EDA. This is a user-friendly PC-

based CAD design package. It has the capability of designing a PhW/PhC device structure, which can be divided into different cells in a hierarchical manner - thus making it easier to design a complex structure with the ability to amend any small changes in the design without the need to make big changes in the design of the whole structure. The designed pattern is subsequently converted into the GDSII file mentioned in the previous section (*section 3.3*). The GDSII file is fractured in the CATS environment before the file is then transferred to the BELLE (Beam-writer Exposure Layout for Lithographic Engineers) software system which was developed specifically to be used for EBL – and which is used to lay out the pattern on the substrates. During this stage, various parameters will be determined by the user - for example the base-dose, spot-size, the location of the pattern on the sample, beam energy and a calculation of the total job running time. The design for a complete PhW and PhC waveguide combination is shown in *Fig. 3.4*. Each design corresponds to the different resist tones used, which will be discussed in a later section. These resists can be either positive (for examples ZEP 520A and PMMA) - see *Fig.3.4 (a)* - or negative tone resists (HSQ and polymer resist such as SU8) - see *Fig.3.4 (b)*. These resists are the radiation sensitive material that defines a pattern after being exposed to radiation, which is usually a polymer, sensitized resin or a spin-on glass like HSQ. The waveguide sections are divided into several sections. The first section comprises a feeder waveguide with a dimension of 2 μm width and 1.2 mm in length - to couple light from a tuneable laser into the 500 nm wide wire waveguides located in the middle section. The feeder waveguide is subsequently tapered adiabatically at an angle of ~7° for approximately 600 μm in length, in order to attain single mode operation for the 500 nm wide waveguides situated in the middle section.
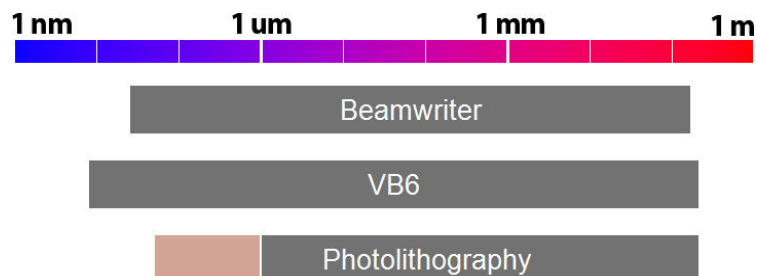


**Fig.3.5***: The scales (resolutions) of difference lithography*

These patterns are defined using direct-write electron beam lithography. Throughout the course of the present work, two different types of resist have been used

progressively to form the primary pattern layer. Both resists are radiation sensitive agents that act as a medium for transferring the pattern using EBL. The first version of the fabrication process was carried out using a positive tone resist, ZEP520A, diluted at 40% with anisol agents. This resist is known to have low molecular length as compared to other resist such as PMMA (poly-methyl methacrylate) - thus this resist is more sensitive and requires low EBL dosage [53] - which in turn reduces overall writing time and retains the high resolution for a very fine feature. The pattern area defined using this resist will become soluble - and can then be removed after the development process by using a suitable developer. During the second half of the fabrication sequence, a negative tone resist, HSQ, has been extensively used - showing a substantial improvement through reduced sidewall roughness because of a reduced number of fabrication steps. The negative tone resist reacts to the electron bombardment by becoming insoluble, which means that the exposed area remains after development using a suitable active solvent.

### 3.3.2 Electron beam Lithography Patterning

The word lithography in the perspective of optoelectronics signifies the definition of a pattern on a material structure that can possibly be made up of many different layers. The word lithography itself means 'writing on a stone' in Greek - and has come to mean writing a transferable pattern on a sample substrate or a mask plate. The patterning process plays an important role in the fabrication sequence, where several technologies have been developed, whether for research purposes or for mass-production. These technologies are based on either parallel writing (photolithography) or sequential writing (electron-beam or focused ion beam (FIB) lithography) [17-19]. The race towards reducing the propagation losses in compact photonic wire and photonic crystal (PhC/PhW) structures has relied substantially on the lithography used for such highly compact devices as optical lithography [20] and electron beam lithography [21, 22]. For instance, there are several methods provide a means for pattern transfer of a desired design such as photolithography, electron-beam lithography and ion beam lithography. A pattern transfer has been known to be a crucial step in the degradation of the original pattern created – thus in some method used, there is also a need for subsequent smoothing process cycle (carried out several times, possibly) - for example through silicon oxidation process.

In addition, Deep UV lithography (DUV) has been widely used for many years to produce complex structures for mass production [23, 24], due to its very much shorter pattern transfer time and ability to replicate the same process several times as compared to direct-write EBL. But a limitation exists in the ability of DUV to generate patterns at the highest resolutions required, hence limiting the capability of patterning sub-nanometre scale patterns. On the other hand, electron-beam lithography (EBL) requires long writing times, because it involves the writing, sequentially, of small features with ultimately high resolution. The differences between these technologies very much depend on the resolution used and the writing time that they can offer, as illustrated in *Fig.3.5*. For example, EBL can be used to design structures with minimum features down to ~10 nm or below. In contrast, for bigger feature sizes, i.e. 1-2 μm, photolithography is the desired tool - and requires the use of a mask for contact printing. Device miniaturization and a highly compact design that can offer full device functionality have pushed lithography to its limits.

|  | EBPG5-HR | VB6-UHR-EWF |
|---|---|---|
| Year | 1990 | 2006 |
| e⁻ source | $LaB_6$ filament | Thermal field emission |
| e⁻ acceleration | 20-50-100 keV | 50-100 keV |
| Resolution | 5 nm | 0.5 nm |
| Spot size | 12 nm | 4 nm |
| Writing field | 0.8 by 0.8 mm @ 50 keV | 1.2 by 1.2 mm @ 100 keV |
| Stage accuracy | 80 nm | 20 nm |

**Table 3.1**: *Details descriptions of different EBL used in this present work*

These technologies have different capabilities, depending on the minimum features used and the design complexity. For research purposes, EBL gives more flexibility, implying that most designs require changes from time-to-time – and implying that production of a new mask will cause further delay and be very costly- thus giving justification for the use of EBL in preference to other technologies, e.g. photolithography. For research purposes, electron beam lithography has become a

commonly used technique for writing a pattern on the device substrate - due to its higher resolution, greater layout design flexibility and alignment accuracy. During the present work, electron beam lithography (EBL) was used as a method for creating the pattern on the sample. It is the process of scanning the surface of the sample, consisting of either positive or negative resist, using a beam of electrons from an electron gun. The electron gun generates a beam of electrons at a suitable current density and the sharply focused beam is scanned over the sample, depositing electrons in the pattern. The amount of the electron flux required depends on the resist used, which can be either positive or negative. There have been two EBL machines available within the James Watt Nanofabrication Centre (JWNC) at Glasgow University during the course of the work for this thesis. The EBPBG5 machine had the capability of writing 30 nm size features with 125 mm square field - whereas the Vistec VB6 UHR EWF, with ultra high resolution and a capability for writing a 4 nm spot with 1.2 mm square fields, superseded the old EBPBG5 during the second half of the research. The detailed specification of these EBL machines can be found in references [25] and [26]. The basic specification of both EBL tools is shown in *Table 3.1*. During the second half of the work for this thesis, 90% of the patterning processes were performed using the newly installed Vistec VB6 tool. The migration from the EBPBG5 machine to the Vistec VB6 machine has proven to be smooth, due to the substantial similarities in the software used in the two machines.

### 3.3.3        Stitching Error

Stitching errors commonly occur in the writing process when using electron beam lithography. This occurrence is recognizable through a discontinuity or gap in either the horizontal or vertical directions of the pattern shown in *Fig.3.6*. Usually a small gap of between 10 nm and 100 nm magnitude can be seen after the pattern development process. This effect can have a significant impact on the overall performance of the device structures, in particular the 500 nm wide photonic wires, due to perturbation of the mode travelling within the photonic wire waveguides. This effect will contribute to higher propagation losses via scattering into the surrounding air, as the mode propagates through the gap or discontinuity area. This problematic issue can arise from the sample not being uniform because resist residues still remain on the under side of the sample, leading to the sample being placed at a significant tilt

angle on the sample holder in the EBL tool. This sample tilt will increase the probability of misalignment during the pattern writing process. On the other hand, writing patterns at different resolution has also been shown to increase the stitching errors.
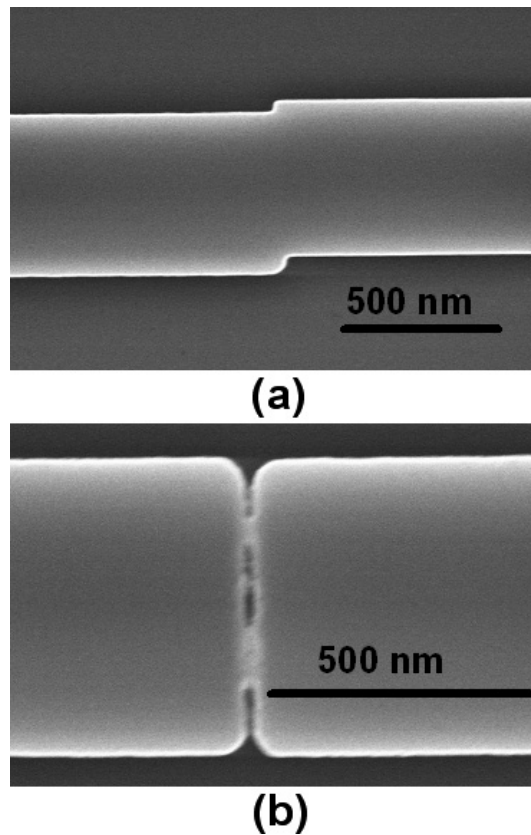


**Fig.3.6***: Examples of stitching errors that occur during the pattern writing process using an EBL tool - showing stitching problems in (a) vertical direction (b) horizontal direction.*

For example, in order to reduce the pattern writing time when using the EBPBG5 tool, the photonic wire waveguides have been written in two different layers with different resolutions. The smaller features, i.e. the photonic wire waveguides and PhC/PhW waveguide sections, were written at 5 nm resolution, whereas larger feature sections (with 2 μm feeder waveguides) were written at the much coarser 100 nm resolution. The stitching errors occurred at the interface between these layers. But the stitching errors were reduced to 10 nm by writing using the same layer, but with single resolution. Moreover, the nominal dimension of the substrate used for patterning in EBL must also be sufficiently large to give extra space for precision clamping of the

substrate in the EBL tool. At least two clamps were needed to attach the substrate to the substrate holder - to prevent it from being placed at a significant tilt angle. In the present work, the typical dimensions of SOI substrate used were *20 mm x 20 mm*, in a rectangular shape – and they were used with about a 2 mm distance from the sample edges - for clamping purposes.

### 3.3.4        Exposure Testing

In order to obtain the correct exposure dose on the pattern, an exposure dose test is carried out using the EBL tool. The exposed areas are then developed using a suitable developer (Oxylene) for positive tone resist (ZEP 502A) and TMAH (tetra-methyl-ammonium hydroxide) for negative tone resist (HSQ) - before defining the silicon guiding layer. The design and the fabrication processes for the photonic wires and photonic crystal waveguides require fine features that sometimes push the electron beam resolution to its limit. During the writing process, the electron beam is scattered by the resist and underlying area with the low density region underneath the resist causing under exposure – while the pattern in high density exposure regions of the resist will be over-exposed. In other words, the electrons are scattered and spread out as they travel far beyond the resist into the underlying substrate. The non-uniformity in the scattering dose is called the proximity effect [27-29]. It was found to be necessary to use the correction proximity effect installed in the electron beam software when executing this design, resulting in an equal dose per unit area [30, 31] for the pattern - by fracturing the shapes, especially in the highest resolution area. The details on the base dose used for each EBL machine in the present work will be discussed in *section 2.4 and 2.5* - and are very much dependent on the type of resist used  - and its condition. The rate of energy loss is inversely proportional to energy - and therefore 100 kV electrons lose half the energy per micrometer that 50 kV electrons do, so pattern transfer requires twice the dose at 100 kV as for 50 kV electrons, as illustrated by the *equation 2.1*.

$$\frac{dE}{ds} = -k\frac{\ln E}{E} \qquad (2.1)$$

Where k is a constant, E is beam energy and dE/ds is the rate of energy loss. This means that at 100 kV EBL voltage, the electron lose half the energy per micron as

compare to 50 kV electron – thus the pattern requires twice the electron dosage in 100 kV compared to 50 kV. By re-writing *equation 2.1* gave;

$$E^2 \propto s \qquad\qquad (2.2)$$

Where the depth of penetration of the electron, s varies as the square of the energy-therefore 100 kV electrons penetrates four times as far as 50 kV electrons. In other word, 100 kV electrons are desirable for designing a fine feature at high resolution as compared to 50 kV.

### 3.3.5      Dry-Etching

After carrying out the patterning process using EBL on the resist layer, the sample is transferred into the silicon waveguide core layer by reactive ion-etching (RIE) [32-33] - a technique that involves both chemical and physical interactions - to remove selected areas of material on the wafer. The moderately high energy ions generated by the chemically reactive plasma under low pressure (vacuum) conditions are used to attack the surface of the material and react with it - thus removing the area patterned by the EBL in the deposited resist. Dry-etching has the advantage over the commonly used wet-etching approach, that it can produce a strongly anisotropic profile, together with good selectivity between the mask layer and the silicon core or other material layer to be etched. The etching processes can be divided into several steps, as mentioned in [34]. A typical RIE system consists of a cylindrical vacuum chamber with the sample placed in the lower part of the chamber. There are several different types of RIE machine available, depending on how the plasma is created within the chamber. Principles of operation used include CCP (Capacitive Coupled plasma) RIE and ICP (Inductively Coupled plasma) RIE. In general, two electrodes are used to produce an electric field between the top and bottom parts of the chamber – and used to accelerate the ions towards the surface of the sample. Strong radio-frequency (RF) electromagnetic fields are initiated in the plasma at certain frequencies. The accelerating electric field will ionize the gas molecules, creating plasma. Due to use of a large voltage difference, the ions will collide with the sample, hence etching away some of the sample surface. The etching process occurs where the ions react with material at the surface of the sample. Any excess electrons are pumped out into the ground without changing any electronic state of the system [54-55]. The etching

conditions in an RIE system depend strongly on process parameters such as pressure, gas flow-rates - and the rf drive power level. Throughout the course of the present work, two different types of RIE machine have been used - a BP80 from Oxford Instruments [35] - and an STS-ICP machine from Surface Technology Systems (STS) [36]. During the first fabrication sequence, ZEP520A positive tone resist has been used to etch a silica layer before defining the silicon guiding layer. The second fabrication sequence was conducted by using negative tone HSQ resist as a mask for silicon etching, leading to a large improvement in the quality of the edges of the patterned features.

## 3.4 Fabrication Process sequence using ZEP520A

### 3.4.1 First Stage: Silica Etching

ZEP520A resist is a positive tone resist that was used during the first cycle of the work, acting as a mask for the silica layer of 200 nm in thickness – and was used by previous co-workers [14]. It is highly sensitive and highly dry-etching resistant [37]. During the first cycle of the pattern transfer process, it was used in conjunction with a Leica EBPBG5 EBL machine.
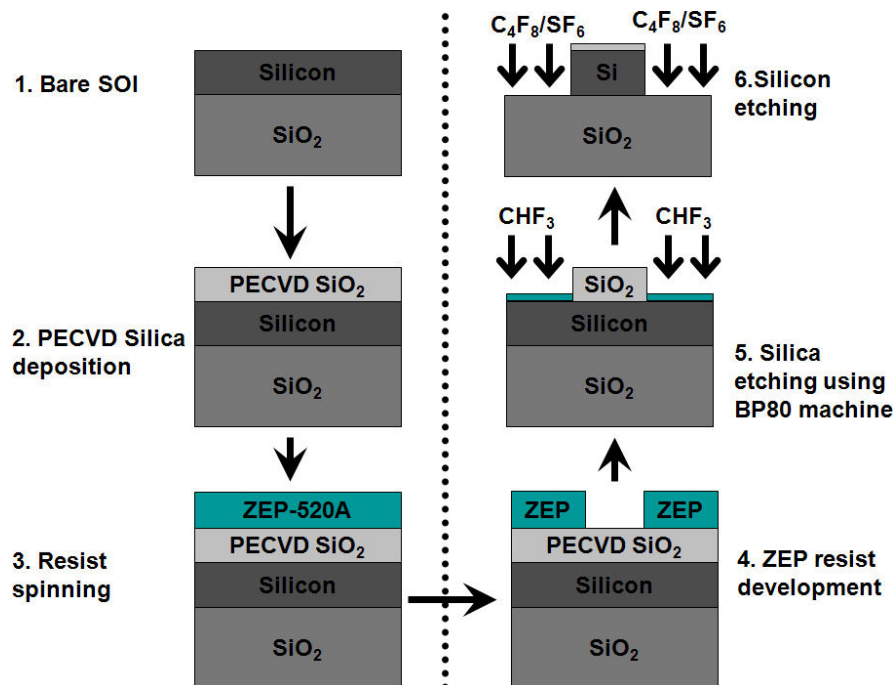


**Fig.3.7**: *First fabrication sequence using ZEP520A*

By referring to the standard process used in [14], the SOI material was initially covered with a 200 nm thick deposit of silicon dioxide ($SiO_2$), using Plasma Enhanced Chemical Vapor Deposition (PECVD) to provide intermediate masking of the pattern transfer process into the silicon layer. A complete fabrication sequence using *ZEP520A* resist and silica to etch the PECVD silica and then the silicon layer is shown in *Fig.3.7*. *ZEP520A* is a relatively soft resist, which makes it appropriate to use it as a mask layer for etching a deposited silica layer - and then using the patterned silica layer as a pattern transfer layer for defining the required pattern into the silicon waveguide layer. The need to use an intermediate mask layer, which in this case is a silica layer, protects the silicon waveguide core layer before carrying out the subsequent RIE etching process. But the ZEP resist layer degrades significantly during etch-processing - thus resulting in damage to the sidewall of the waveguide, as well as losing or distorting the smallest features of the waveguide device pattern. On the other hand, the quality of the PECVD silica layer deposited for the present work was also found to be poor, resulting in waveguides with significant sidewall roughness.

| Parameter | Low Resolution (2 mm ridge) | High resolution (adiabatic taper and wire waveguides) |
|---|---|---|
| e⁻ acceleration | 50 keV | |
| Resolution | 5 nm | 100 nm |
| e⁻ acceleration | 15 nm | 160 nm |
| Dose | 130 μC/cm$^2$ | 130 μC/cm$^2$ |
| Resolution | | |

**Table 3.2**: *Parameters used for SOI patterning using ZEP resist in EBPG5 EBL.*

In particular, in the pattern of a single row PhC/PhW waveguide micro-cavity considered for this present work, there is also found to be difficulty in controlling the hole dimensions in that particular design, due to variations in the deposited silica film thickness by $\pm15$ nm, thus affecting the etch rate of the silica film. In the first stage of the pattern transfer process, the silica layer was initially defined using ZEP520A resist. The resist was spun at 2000 rpm for 60 seconds, giving the thickness of between 120 and 140 nm. The samples were baked at 180 °C for approximately

40 minutes. Due to its longer-molecular length than other resists such as PMMA (poly-methyl methacrylate), this resist is known to be highly sensitive to the EBL exposure dose, which requires a lower EBL dose of ~130 $\mu C/cm^2$ with 50 kV electrons. In return, it effectively reduces the overall writing time, as compared to other positive tone resists such as PMMA.

In order to reduce stitching errors and writing time, the patterns were designed in two different layers having different resolutions and spot sizes, as illustrated in *Table 3.2* (refer to *Fig.3.4*).

| Parameter | Value |
|---|---|
| Machine | BP80 |
| Gas | $CHF_3$ |
| Flow | 20 SCCM |
| Pressure | 17 mTorr |
| Forward RF power | 10 Watt |
| Time | 8 minutes |

**Table 3.3**: *Standard process used for silica etching*

The patterns were then exposed at 50 kV in the EBPBG 5 EBL tool. The exposed samples were finally developed using O-xylene at 23°C for 1 minutes and rinsed with IPA for 30 seconds. The silica layer was etched using $CHF_3$ gas in the BP80 RIE machine for 8 minutes. This process required no attempt at optimization, since it had already been used by other co-workers [14, 16]. The process details are illustrated in *Table 3.3*. A typical silica etching result using ZEP as the resist layer is shown in *Fig.3.8*.
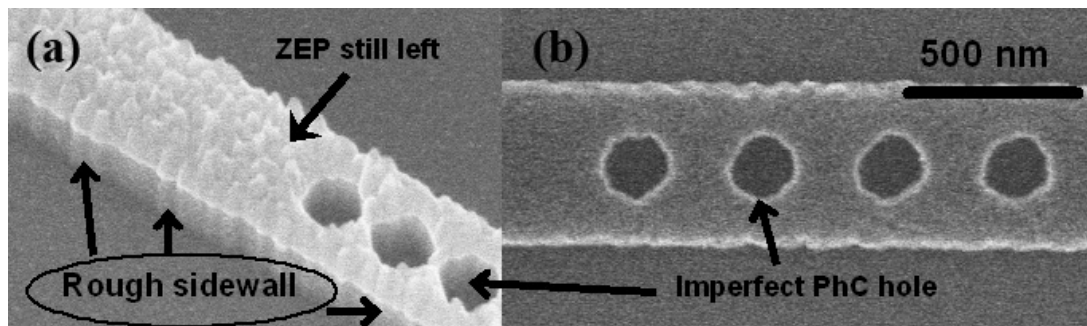


**Fig.3.8**: *SEM images showing the result after silica etching using RIE BP80 tools (a) bird eye view (b) top view*

It shows that, the patterns were transferred successfully with the verticality of the sidewall calculated to be of approximately 80° - 86° - see *Fig.3.8 (a)*. On the other hand, the roughness of the sidewall appears to be poor and imperfect shaped holes resulted from this process. The hole diameters and spacing vary by as much as 50 to 100 nm from the actual design dimensions – giving a ratio of 1:3 between the actual design and the fabricated device structures measured using SEM 4700 tools. This condition will certainly reduce the overall fabrication efficiency and reproducibility where the need to generate 1:1 pattern transfer from CATS design towards fabrication outcomes is critical- for having better comparison and device analysis between the measurement and the simulation results. On the other hand, a difference in the silica deposition rate and the quality of the PECVD film deposited has contributed to the poor repeatability and reproducibility of this process - where the waveguide and hole dimensions within the photonic wire waveguide changed in every fabrication cycle. Several attempts has been made to reduce the side-wall roughness of the waveguide - e.g. by removing the resist residues at the waveguide edges by performing oxygen ashing – but no significant improvement was obtained. This failure is believed to be due to the poor quality of PECVD silica deposited, which had grainy textures, which left grass-like features produced in the silica etching process.

### 3.4.2 Second Stage: Silicon Etching

During the second stage process, the silicon layer is etched using RIE ICP tools with the combination of $SF_6/C_4F_8$, as previously used by co-workers [16]. The silicon layer was defined using a silica mask layer.

| Parameter | Value |
|---|---|
| Machine | STS-ICP |
| Gas | $SF_6/C_4F_8$ |
| Flow | 40/90  SCCM |
| Pressure | 12  mTorr |
| Coil power | 600 W |
| Platen power | 10 W |
| Time | 49 seconds |

**Table 3.4**: *Etching process for defining silicon guiding layer using STS ICP tools*

The silicon layer is etched for 49 seconds with a silicon etching rate of 5 nm/s and *Si/SiO$_2$* selectivity of ~ 10. *Table 3.4* shows the detailed process parameters in the early stages of silicon etching using $SF_6/C_4F_8$ chemistry. *Fig.3.9* shows the hole pattern after this process. The roughness of the sidewall is still poor, resulting from the previous pattern transfer at the silica level using ZEP520A resist. But the cross-sectional view of the waveguide still shows a good vertical profile (see *Fig.3.9 (a)*) at an angle of ~80°, with a silicon layer of approximately 30 nm still left un-etched on each side of the ridge waveguide, which obviously will have some effect on the optical confinement of the silicon waveguides, due to the effective index difference at the boundary between the silicon guiding layer and silica buffer layer underneath it. Further improvement can be made in reducing the roughness of the sidewall by means of thermal oxidation with reduced propagation losses [38- 40]. But this process requires more time and needs to be investigated carefully, since the thermal oxidation process will change the basic properties of the waveguide, i.e. the effective refractive index of the waveguide - thus changing the modal distribution within that particular waveguide.
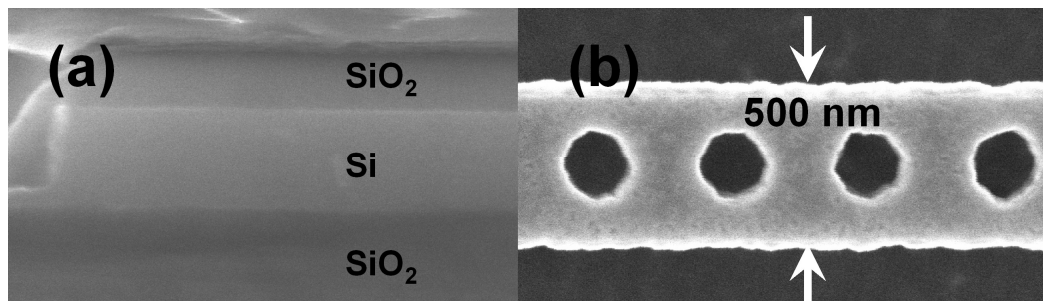


**Fig.3.9**: *SEM image of silicon after etching process using the STS-ICP tool (a) Cross sectional view (b) top view*

A near-perfect fabrication process with reduced sidewall roughness is needed, especially in the patterning of the silicon layer - and therefore there is need for a single cycle silicon patterning process, which is why the new process using HSQ resist to provide the mask layer for a single level silicon pattern transfer process has been developed.

**3.5**        **Fabrication process: Hydrogen Silses-Quioxane (HSQ)**

**3.5.1**        **RIE STS-ICP: Silicon Etching**

A stronger and more robust resist, such as HSQ (a negative tone resist), which is capable of supporting writing with very high resolution using EBL [41], is useful for pattern transfer into the silicon core layer. HSQ is a spin-on-glass material that consists of silicon, oxygen and hydrogen atoms bonded together. When high energy is applied thermally or through electron bombardment, the hydrogen atoms will be displaced, leading to the formation of a silica-like network structure [42-44]. The deposited HSQ can be developed after electron-beam exposure by using basic reagents such as KOH (Potassium Hydroxide) and TMAH (Tetra-Methyl-Ammonium Hydroxide) [42]. The fabrication process using HSQ has also proven to result in smooth sidewalls with a very low propagation loss of 0.92 dB/cm being reported in [45], which is the lowest reported propagation loss for photonic wire waveguide structures of this type. A relatively thick HSQ layer was used to provide a pattern transfer and mask layer for silicon etching. This process involves a single step reactive ion-etching process. The silicon layer is directly etched using the STS-ICP machine.
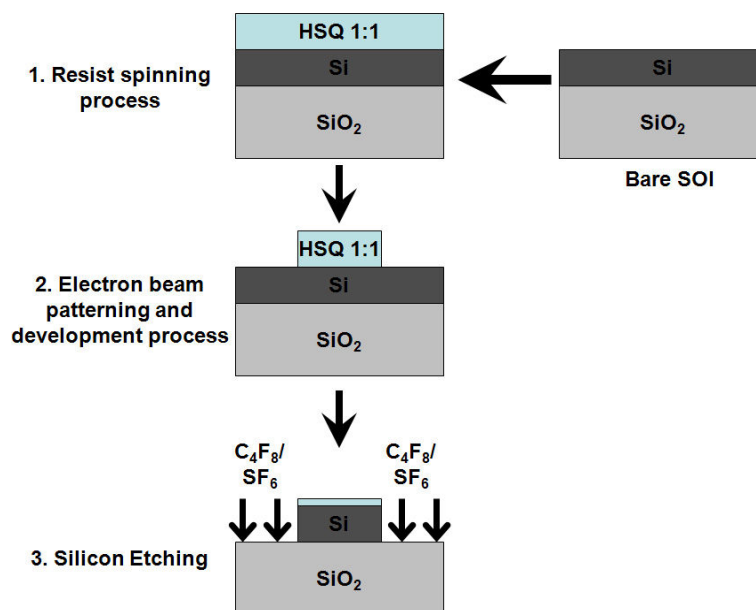


**Fig.3.10**: *Single steps process: Fabrication sequence using HSQ resist*

Most of the optimization work on the patterning process using this resist has been carried out by co-workers, with more detailed literature concerned with HSQ appearing in the references cited in [16]. During the course of this work, further optimization of the silicon etching process was needed, especially when dealing with photonic crystal structures where different hole dimensions gave different etching rates - because smaller hole sizes have lower etching rates, as compared with bigger hole sizes. This effect is due to the etching gas being trapped inside the hole longer in a smaller hole, contributing to a lower etching rate as compared to that for a bigger hole size. Therefore longer etching times, with suitable etching parameters, are necessary. The HSQ layer acts as a mask for etching of the silicon guiding layer. The HSQ used in this work had a 1:1 dilution in MIBK (Methyl-Isobuthyl-Ketone) that gave a nominal thickness of approximately 200 nm when spun at 3000 r.p.m. The fabrication process steps using HSQ to define the silicon guiding layer are shown in *Fig.3.10*.

| Parameters | EBPBG 5 Res | | VB 6 High Res.     Low Res. | |
|---|---|---|---|---|
| e⁻ acceleration | 50 keV | | 100  keV | |
| Resolution | 5 nm | 100 nm | 2.5 nm | 10 nm |
| Spot size | 15 nm | 300 nm | 6 nm | 20 nm |
| Base dose | 600 $\mu$C/cm$^2$ | | 1500 $\mu$C/cm$^2$ | |
| Writing field | 0.8 x 0.8 mm | | 1.2 x 1.2 mm | |

**Table 3.5***: Important parameters used for different EBL tools.*

The resist is spun at 3000 rpm for 60 seconds to obtain an HSQ layer with a nominal thickness of approximately 200 nm, sitting on a silicon layer. The sample is then baked at 90° C, as described in [44]. After the spinning and baking process, the patterns were exposed using an EBL tool. Initial optimization was carried out for the EBPBG5 tool - and further optimization has been carried out for the newly installed VB6 tool at a later stage. The VB6 electron-beam tool, which is capable of writing at 100 keV with a resolution of 2.5 nm has a substantially larger writing field of 1.2 mm$^2$ – and a spot size of approximately 6 nm, as compared to the previously used EBPBG5 tool. Detailed descriptions of both electron-beam tools are shown in *Table 3.5*. Dose calibration has been carried out to identify the optimum dose required for both

electron-beam tools by applying test doses ranging from 200 to 1000 μC/cm$^2$ and 1000 to 2500 μC/cm$^2$ for the EBPBG5 and VB6 tools respectively. The optimum dose was found to be 600 μC/cm$^2$ for the EBPBG5 tool and 1500 μC/cm$^2$ for VB6 tool. The difference in the dose between the EBPBG5 and VB6 tools depends very much on the resist thickness spun on the sample and the number of electron that can penetrate into the resist. For instance, the sample was written at 100 keV using the VB6 tool, whereas 50 keV was used for the EBPBG5 - which justifies the difference in the optimum base dose used.

The exposed patterns were developed using TMAH at 25% concentration in water - which has been reported to give a  higher aspect ratio and reproducibility for thicker resists, as compared to other developers such as CD26 (TMAH at 2.38% concentration in water) [44, 46].
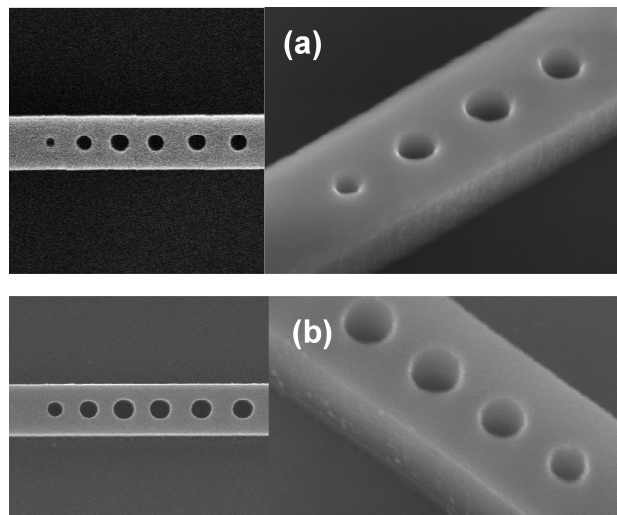


**Fig.3.11**: *SEM images of the top view and birds eye view of the waveguide structures at the optimum dose using HSQ resist patterned by (a) EBPBG5 tools (Dose =600 μC/cm$^2$) (b) VB6 tools (Dose=1500 μC/cm$^2$)*

The samples were typically developed for 30 s in TMAH, with no post exposure bake being required. It is also necessary to agitate the sample well during the process since bubbles are produced during development process. The sample is then rinsed thoroughly in water for 60 s or more; but using two beakers (30 s in each) is suggested, since any remaining developer leaves a scum on the surface of the wafer.

| Parameter | Value |
|---|---|
| Machine | STS-ICP |
| Gas | $SF_6/C_4F_8$ |
| Flow | 30/90 SCCM |
| Pressure | 10 mTorr |
| Coil power | 600 W |
| Platen power | 12 W |
| Time | 3 minutes |

**Table 3.6**: *Etching conditions for defining Si layer using STS-ICP*

A final rinse with IPA is useful, giving high aspect ratio features, since IPA has a lower surface tension than water. Careful attention has to be given during the development process, where the sample must not self-dry when transferring from beaker to beaker. *Fig.3.11* shows SEM images of the etched silicon layer with the optimum dose used for each case. It shows a great improvement, in comparison with EBBPG 5 tool, in the pattern transfer, as the 1:1 final pattern was obtained with the VB6 tool. The etching conditions used for this process sequence are shown in *Table 3.6*.
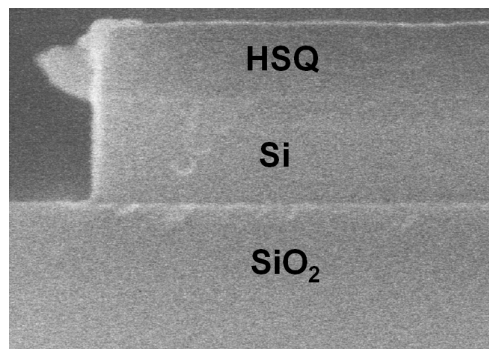


**Fig.3.12**: *Cross- sectional view of the optimized silicon etched using STS-ICP tools at one of the end cleaved facet.*

The motivation towards optimizing the sidewall verticality is the need to avoid any polarization mixing [47] that may eventually 'damage' the modal distribution of the optical waveguides. By reducing the chamber pressure during dry-etching, it is possible to reduce the undercutting of the profile at the interface between the silicon core and the silica buffer layer. By referring to *Table 3.4* and *Table 3.6*, the reduction in $SF_6$ flow from 40 to 30 SCCM has resulted in a slower etching rate and selectivity,

since $SF_6$ is the dominant 'active' gas in the chamber. This has resulted in an approximately 86° angle, with respect to the wafer plane, in terms of sidewall verticality, as shown in *Fig.3.12*. In conclusion, the newly developed process using the STS-ICP machine - with a mixture of $SF_6/C_4F_8$ and a state-of-the-art VB6 EBL tool for the patterning process - has shown great improvement, especially in terms of the reproducibility of the devices fabricated. On the other hand, the reduction in the fabrication steps from two etching steps, using PECVD silica, into just a single step etching using HSQ resist has also shown a reduction in the fabrication time. This process has shown a high degree of repeatability and high reproducibility in the device structures characterized for this present work.

**3.6**           **Photolithography - silica 'buffer' layer etching**

In this section, a brief description of the methods used to remove the silica buffer layer will be given. The removal of the silica buffer layer underneath the silicon core layer provides air bridge structures of silicon photonic wire waveguides - which have been used to increase the optical confinement of the silicon waveguides.
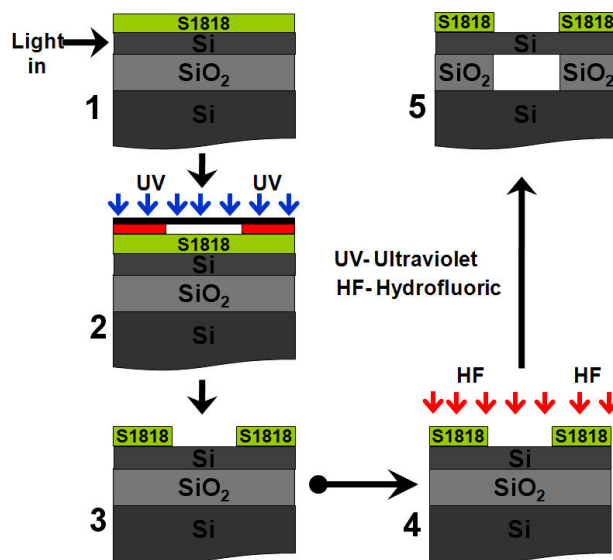


**Fig.3.13**: *Process step for etching silica buffer layer underneath the Silicon waveguides layer showing cross-sectional side view of the silicon waveguides.*

Photolithographic techniques are extensively used for patterning larger feature structures with bigger dimensions, such as waveguide structures with micrometer scale dimensions - and therefore it is suitable for opening the etch windows for removing the silica layer beneath the silicon. The optical mask was prepared by first writing, using the EBPBG5 tool, onto a chrome mask plate with alignment markers on the samples. The initial process began with deposition of S1818 photo-resist on the etched silicon waveguide pattern, using the standard process mentioned in the previous section (*see section 2.5*). The complete process for etching the silica layer is illustrated in *Fig.3.13*.

The etched silicon waveguide sample is spun at 4000 r.p.m., resulting in an S1818 resist thickness of ~1.8 μm. The sample is baked at 90°C for 30 minutes and exposed with a standard process in the MA6 mask aligner, for 4 seconds under a UV source. The samples were developed using a specific composition of micro-posit developer and RO water (1: 1) for 75 seconds. Before the etching process, the samples were post-baked at 120°C for 10 – 15 minutes, to harden the resist.
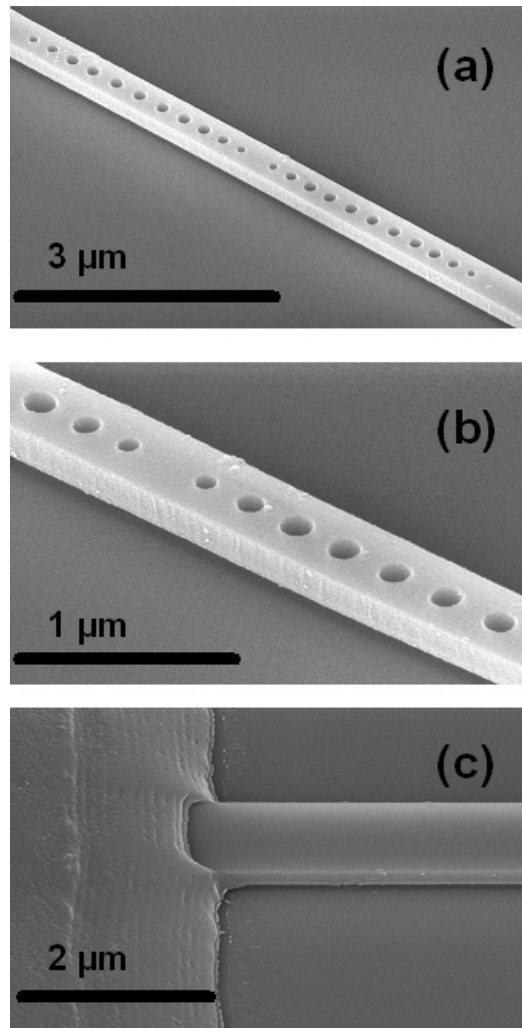
**Fig.3.14**: *SEM image with bird's eye view (angle ~30°) of the etched silica buffer layer with silicon waveguide hanging in the air showing : (a) 6 μm long suspended PhC/PhW waveguides (b) Close up of tapered hole PhC embedded in PhC/PhW waveguides, with smooth sidewall, (c) one of the end waveguides, with S1818 photo-resist still exist before removal.*

Finally the silica buffer layer was etched using dilute hydrofluoric acid (5:1) for 20-25 seconds. The etching rate of the silica was found to be around 10-13 nm/s. This process will remove approximately 300-350 nm of the silica buffer layer, leaving the silicon waveguide layer hanging in the air and supported by the two waveguide ends. *Fig.3.14* shows SEM images of the 'hanging' silicon waveguide, without a silica cladding/buffer layer underneath it. Even though the silica cladding has not been removed completely (only approximately 300 - 350 nm), but the results obtained have

shown a significant improvement in its performance. In addition, the thin layer of HSQ resist on top of the silicon has also been removed, leaving a suspended silicon-only wire suspended from its two ends.

## 3.7        Characterization and Loss Measurement Techniques

The devices were characterized using a tunable laser source covering the wavelength range from 1455 nm to 1580 nm. TE polarized light was end-fire coupled into and out of the device waveguides using x40 magnification objective lenses - and the optical signal was then detected using a germanium photodiode.
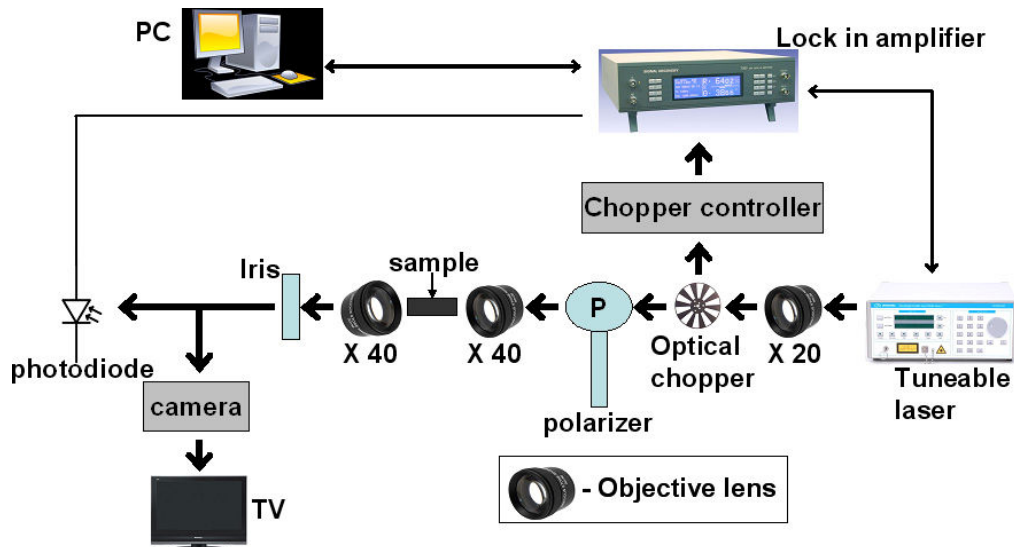


**Fig.3.15**: *Schematic drawing of the measurement set up used for device characterizations.*

The transmission response was further analyzed - and the propagation losses of the 2 μm width ridge reference waveguide were initially measured by considering the Fabry-Perot (FP) effects due to both end facets. The measurement set up is shown in *Fig.3.15*. This set-up has been used for characterizing the transmission response of the one-dimensional PhC/PhW devices. The propagation losses of this particular device originate predominantly from out-of-plane scattering due to the sidewall roughness. Initial loss measurements on the reference500 nm wide waveguide  were carried out using the Fabry-Perot (FP) resonance technique - by first making the assumption that the end facets has reasonably high quality mirror surfaces after the cleaving process,

with the reflectivity given by *equation 2.4*. The maxima and minima of the FP fringes and the total length of the cavity, without taking the input and output coupling into account, were estimated [48]. Thus the loss expression can be written as [49];

$$\alpha = -\frac{1}{L} \ln\left(\frac{1}{R} \bullet \frac{C_R - 1}{C_R + 1}\right) \qquad (2.2)$$

L – Total length of the cavity (distance of end-to-end facets forming cavity)

$C_R$ - contrast ratio of the maxima and minima in the transmission response, given by

$$C_R = \sqrt{\frac{T_{\max ima}}{T_{\min ima}}} \qquad (2.3)$$

T is the transmission response that corresponds to the maxima or minima values due to FP fringe effects.

R- Reflectivity of the end facets, given by;

$$R \sim 31 \% \text{ where } R = \left(\frac{(n_{si} - 1)^2}{(n_{si} + 1)^2}\right) \qquad (2.4)$$

$$\text{where } n_{si} = 3.45$$

This equation implies that, for single mode waveguide operation, a larger difference between the maxima and the minima gives lower propagation losses through the waveguides. A combination of an optimum fabrication recipe, used together with a reduction in sidewall roughness, has contributed to the low propagation losses. As shown in *Fig.3.16*, the free spectral range (FSR) of ~1 nm for each resonance corresponds to a combined length in the waveguides of ~ 5 mm - which includes the 2 μm wide feeder waveguides, adiabatic taper sections and 500 nm PhC/PhW waveguides sections. In some cases, the incoherent characteristics of the transmission maxima and minima suggest the existence of multimode propagation conditions [**50**] - due, for example, to fabrication inaccuracy. So determination of the propagation losses using this method becomes increasingly difficult. Based on Eq. 2.4, the estimated propagation losses for 500 nm un-patterned photonic wire waveguides using the cut-back approach [51] was measured to be 0.91 ± 0.15 dB/cm at λ~1520 nm, as shown in *Fig.3.17* as already been measured by [45]. The propagation losses obtained in the present work are relatively close to the current state-of–the art propagation losses achieved in some work [56-58] - although recently propagation losses of 0.9 dB/cm have been reported by others in [45] - as also shown in *Fig.3.17*.
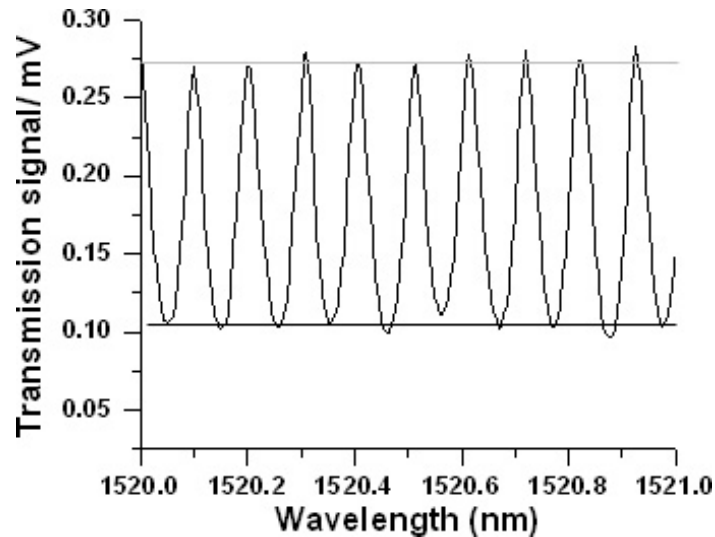
**Fig.3.16***: Characterization of the transmission response for*

*2 μm un- patterned wire waveguides.*

Reduction of the propagation losses through the use of the newly developed HSQ process represents a substantial improvement, as compared with the previously used process based on ZEP resist - which gave typical propagation losses of 15 dB/cm.
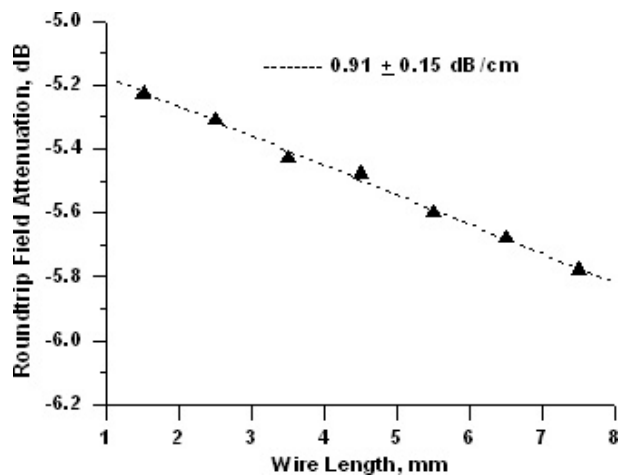


**Fig.3.17***: Loss attenuation for different wire length*

In addition, I shall not discuss the causes of the propagation losses in detail here, since the main target of the fabrication processes developed in the present work is to improve the reproducibility and repeatability of the fabricated devices.

## 3.8        Summary

The use of standard fabrication processes for device pattern writing via different types of EBL tool has been accomplished. The RIE dry-etching methods used have shown great improvements in defining the PhW/PhC waveguide structures. Different fabrication cycles have shown great improvements in the form of reductions in the sidewall roughness - where the initial results using ZEP resist have improved through use of the newly developed HSQ fabrication cycle. On the other hand, the newly installed state-of-the-art Vistec VB6 EBL tool - with its greater capabilities, e.g. of writing larger fields (1.2 x 1.2 mm) with a high resolution of 1.25 nm, has enabled high quality pattern transfer. A combination of these technologies, together with well developed processes used by previous workers [14-16], has proven to reduce sidewall roughness without the need for extra process such as thermal oxidation/etching cycling. Further attempts at optimizing the process have not been made, since the current process used shows great consistency in performance. In addition, standard processes used for wet chemical etching - in particular silica etching for membrane structures - have shown good controllability of the etching rate.

**References:**

1. Theis, T. N., "The future of interconnection technology", *IBM Journal of Research and Development*, vol. 44, no. 3, pp. 379-390, 2000.

2. Bogaerts, W., Dumon, P., Wiaux, V., Wouters, J., Beckx, S., Taillaert, D., Luyssaert, B., Van Campenhout, J., Van Thourhout, D., and Baets, R., "Nanophotonic waveguides in silicon-on-insulator fabricated with CMOS technology", 1st Flanders Engineering PhD Symposium, Belgium, pp. 63, 2003.

3. Jalali, B., Yegnanarayanan, S., Yoon, T., Yoshimoto, T., Rendina, I, and Coppinger, F., "Advances in Silicon-on-insulator Optoelectronics", *IEEE Journal of Selected Topics in Quantum Electronics*, vol. 4, no. 6, pp. 938-947, 1998.

4. Masini, G., Colace, L., and Assanto, G., "Si based optoelectronics for communications", *Material Science and Engineering B*, vol. B89, pp. 2-9, 2002.

5. Soref, R. A., and Lorenzo, J. P., "All-silicon active and passive guided-wave components for λ = 1.3 μm and 1.6 μm", *IEEE Journal of Quantum Electronics*, vol. QE-22, no. 6, pp. 873-839, 1986.

6. Ahmad, R.U., F. Pizzuto, G.S. Camarda, R.L. Espinola, H. Rao and R.M. Osgood. *IEEE Photonics Technol. Lett.* **14** 65, 2002.

7. Espinola, R.L., R.U. Ahmad, F. Pizzuto, M.J. Steel and R.M. Osgood. *Opt. Expr.* **8** 517, 2001.

8. F.Ohno,T Fukazawa, T.Baba,"Mach Zehnder Interferometer composed of μ-bends and μ-branches in a Silicon photonic wire waveguide", *Japanese Journal of Applied Physics*,vol:44, No:7A, pp.5322-5323, 2005.

9. Bruel, M., "Silicon on insulator material technology", *Electronics Letters*, vol. 31, no. 14, pp. 1201-1202, 1995.

10. T. W., Reed, G. T., Vonsovici, A., Evans, A. G. R., Routley, P. R., and Josey, M. R., "0.15 dB/cm loss in Unibond SOI waveguides", *Electronics Letters*, vol. 35, no. 12, 199.

11. M. J., Dolan, R. P., Jiao, J., and Nakai, T., "Thin-layer SIMOX for future applications", Proceedings IEEE International SOI Conference, pp. 106-107, 1999.

12. M. Bruel, B. Aspar, and H. Auberton, "Smart-cut: A new silicon on insulator material technology based on hydrogen implantation and wafer bonding," *Japanese Journal of Applied Physics*, Part 1: Regular Papers and Short Notes and Review Papers, vol. 36, no. 3 SUPPL. B, pp. 1636–1641, 1997.

13. "SOITEC Unibond Process." [Online]. Available: http://www.semiconductor-technology.com/projects/soitec bernin/soitecbernin2.html

14. H.M.H.Chong, "Photonic Crystal and Photonic Wire Structures for Photonic Integrated Circuits," Ph.D. dissertation, University of Glasgow, 2004

15. E.A.Camargo, "Switchable Devices Based on Photonic Crystal Channel Waveguides," Ph.D. dissertation, University of Glasgow, 2004

16. Marco Gnan, "Photonic Wire Devices in Silicon-on-Insulator," Ph.D.dissertation, University of Glasgow, 2007.

17. S. Thoms and D. S. MacIntyre, "Electron Beam Lithography Course." [Online]. Available: http://www.elec.gla.ac.uk/jwnc/index.php?module= page&dir= Ebeam Docs&page=CourseOverview.html

18. A. S. Jugessur, "Photonic Crystal Microcavity Filters Embedded In Ridge Waveguide Structures," Ph.D. dissertation, University of Glasgow, 2004.

19. P. Rai-Choudhury, Handbook of Microlithography, Micromachining and Microfabrication. SPIE, 1997, vol. 1: Microlithography.

20. M. Notomi, A. Shinya, S. Mitsugi, E. Kuramochi, and H. Ryu, "Waveguides, resonators and their coupled elements in photonic crystal slabs," *Opt. Express* 12, 1551-1561 (2004),

21. E. Kuramochi, M. Notomi, S. Hughes, A. Shinya, T. Watanabe and L. Ramunno, "Disorder-induced scattering loss of line-defect waveguides in photonic crystal slabs," *Phys Rev B*. **72**, 161318 (2005).

22. Bogaert W,Dumon P,Luyssaert B,Bienstman P," Nanophotonic Waveguides in Silicon-on-Insulator Fabricated with CMOS Technology," *Journal of Lightwave Technology*, Volume 23, Issue 1, pp 401-412, January 2005.

23. Dumon,P et all," Low-Loss SOI Photonic Wires and Ring Resonators Fabricated With Deep UV Lithography," *IEE Photonic Technology Letter*, Volume 16, No 5, May 2004.

24. Parikh, M., "Corrections to proximity effects in electron beam lithography. I. Theory", *Journal of Applied Physics*, vol. 50, no. 6, pp. 4371-4377, 1979.

25. M.Settle, M.Salib, A.Michaeli and T.Krauss," Low loss silicon on insulator photonic crystal waveguides made by 193nm optical lithography", *Optics Express*, Vol. 14, No. 6, March 2006.

26. "Vistec Lithography." [Online. Available: http://www.vistec-litho.com]

27. Ma, S. K. S., Parikh, M., and Ward, W., "Proximity corrections in a raster scan electron lithography machine", *Journal of Vacuum Science Technology*, vol. 19, no. 4, pp. 1275-1278, 1981.

28. Groves, T. R., "Efficiency of electron-beam proximity error correction", *Journal of Vacuum Science Technology B*, vol. 11, no. 6, pp. 2746-2753, 1993

29. Watson, G. P., Fetter, L. A., and Liddle, A., "Dose modification proximity effect correction scheme with inherent forward scattering corrections", *Journal of Vacuum Science Technology B*, vol. 16, no. 6, pp. 2309-2312, 1997.

30. Hintermaier, M., Hofmann, U., Hubnerm B., Kalus, C. K., Knapek, E., Koops, H. W. P., Schlager, R., Seebald, E, and Weber, M., "Proximity correction using computer aided proximity correction (CAPROX): Evaluation and application", *Journal of Vacuum Science Technology B*, vol. 9, no. 6, pp. 3042-3047, 1991.

31. Abe, T., and Takigawa, T., "Proximity effect correction for high-voltage electron beam lithography", *Journal of Applied Physics*, vol. 65, no. 11, pp. 4428-4434, 1989.

32. Schwartz, G. C., and Schaible, P. M., "Reactive ion etching of silicon", *Journal of Vacuum Science and Technology*, vol. 16, no. 2, pp. 410-413, 1979.

33. 19. Jin, W., and Sawin, H. H., "Feature profile evolution in high-density plasma etching of silicon with $Cl_2$", *Journal of Vacuum Science and Technology A*, vol. 21, no. 4, pp. 911-921, 2003.

34. M. Sugawara, Plasma Etching: Fundamentals and Applications. Oxford University Press, 1988.

35. "STS, Surface Technology Systems." [Online]. Available: http://www.stsystems.com.

36. "Oxford Instruments." [Online]. Available: http://www.oxford-instruments.com.

37. "ZEP520 Series EB Resists." [Online]. Available: http://www.zeonchemicals.com/electronicmaterials.aspx?id=11683099

38. Jansen, H., Gardeniers, H., de Boer, M., Elwenspoek, M., and Fluitman, J., "A survey on the reactive ion etching of silicon in microtechnology", *Journal of Micromechanics and Microengineering*, vol. 6, pp. 14-28, 1996.

39. 25. Lee, K. K., Lim, D. R., Kimerling, L. C., Shin, J., and Cerrina, F., "Fabrication of ultralow-loss Si/SiO$_2$ waveguides by roughness reduction", *Optics Letters*, vol. 26, no. 23, pp. 1888-1890, 2001.

40. 26. Lee, K. K., Lim, D. R., Luan, H-C., Agarwal, A., Foresi, J., and Kimerling, L. C., "Effect of size and roughness on light transmission in a Si/SiO$_2$ waveguide: Experiment and model", *Applied Physics Letters*, vol. 77, no. 11, pp. 1617-1619, 2000.

41. H. Namatsu, T. Yamaguchi, M. Nagase, K. Yamazaki, and K. Kurihara, "Nano-patterning of a hydrogen silsesquioxane resist with reduced linewidth fluctuations," *Microelectronic Engineering*, vol. 41-42, pp. 331–334, 1998.

42. H. Namatsu, T. Yamaguchi, M. Nagase, K. Yamazaki, and K. Kurihara, "Nano-patterning of a hydrogen silsesquioxane resist with reduced linewidth fluctuations," *Microelectronic Engineering*, vol. 41-42, pp. 331–334, 1998.

43. F. C. M. J. Van Delft, "Delay-time and aging effects on contrast and sensitivity of hydrogen silsesquioxane," *Journal of Vacuum Science and Technology B: Microelectronics and Nanometer Structures*, vol. 20, no. 6, pp. 2932–2936, 2002.

44. W. Henschel, Y. M. Georgiev, and H. Kurz, "Study of a high contrast process for hydrogen silsesquioxane as a negative tone electron beam resist," *Journal of Vacuu*m Science and Technology B: Microelectronics and Nanometer Structures, vol. 21, no. 5, pp. 2018–2025, 2003.

45. M. Gnan, S. Thoms, D. S. Macintyre, R. M. De La Rue, and M. Sorel, "Fabrication of low-loss photonic wires in silicon-on-insulator using hydrogen silsesquioxane electron-beam resist," *Electronics Letters,* vol. 44, pp. 115-116, 2008.

46. Y. M. Georgiev, W. Henschel, A. Fuchs, and H. Kurz, "Surface roughness of hydrogen silsesquioxane as a negative tone electron beam resist," *Journal of Vacuum Technology*, vol. 77, no. 2, pp. 117–123, 2005.

47. E. D. Finlayson, J. M. Heaton, B. M. A. Rahman, and S. S. A. Obayya, "Polarization conversion in passive deep-etched GaAs/AlGaAs waveguides," *Journal of Lightwave Technology*, vol. 24, no. 3, pp. 1425–1432, 2006.

48. Walker, R. G., "Simple and accurate loss measurement technique for semiconductor optical waveguides", *Electronics Letters*, vol. 21, pp. 581-583, 1985.

49. Zappe, H. P., "Introduction to semiconductor integrated optics", Artech House, 1995.

50. Walker, R. G., "The design of ring-resonators for integrated optics using silver ion-exchanged waveguides", PhD thesis, University of Glasgow, 1981.

51. Kapon, E and Bhat, R.,"Low-loss single-mode GaAs/AlGaAs optical waveguides grown by organometallic vapor phase epitaxy", *Applied Phys. Lett.* 50(23), pp. 1628-1630, 8 June 1987

52. http://www.soitec.com/en/technology/

53. Macintyre, D., and Thoms, S., "Introduction to Ebeam lithography", Lecture notes, University of Glasgow, 2004.

54. Coburn, J.: Plasma Etching and RIE: Fundamentals and Applications.

55. M.Sugawara and B.L Stansfield", Plasma Etching: fundamentals and applications", Oxford University Press, 1998, ISBN 019856287X, 9780198562870

56. Y. A.Vlasov, S. J. McNab, "Losses in single-mode silicon-on-insulator strip waveguides and bends", *Optics Express*, **12** (**8**), 2004.

57. S. J. McNab, N. Moll, Y. A. Vlasov, "Ultra-low loss photonic integrated circuit with membrane-type photonic crystal waveguides", *Optics Express* **11**, (**22)** , 2003.

58. V.Almeida, R. Panepucci, M.Lipson,"Nanotaper for compact mode conversion", *Optics Letters*, **28**, 2002.

# CHAPTER 4:

# Photonic Crystal (PhC) / Photonic Wire (PhW) Micro-cavities

**4.1        Introduction**

It has been of major interest in recent research to produce faster optical processing for a variety of telecommunications applications and for other applications of high performance optoelectronics. The combination of one-dimensional photonic crystal structures (PhC) in narrow photonic wire (PhW) waveguides- realized in high refractive-index contrast materials such as silicon-on-insulator (SOI), is one of the main contenders for provision of many compact devices on a single chip. This development is due to the ability of silicon technology to support monolithic integration of optical interconnects - and thereby to form fully functional photonic devices incorporated into CMOS chips. The high index contrast of the combination of a silicon core with a surrounding cladding of silica and/or air provides strong optical confinement, leading to the realization of more compact structures, small device volumes, sharp bends, abrupt Y-junctions and Mach Zehnder structures [1-6, 19]. On the other hand, the manipulation of the refractive index of silicon by means of the thermo-optic effect and electro-optic effects for compact modulators has also been demonstrated in both PhW- and PhC-silicon based devices [7, 8, 20-21]. The large thermo-optic coefficient of silicon is a key point for the design of optical modulators that exploit the thermo-optic effect. In order to obtain a wide range of device functionality, the reduction of propagation losses in narrow wires is equally important, although there are still performance limitations determined by fabrication processes [9, 18].  Recently losses as low as 0.92 dB/cm for a very narrow wire have

been reported [10]- through the use of hydrogen silsesquioxane (HSQ) resist and a reduction, through stage-tilt compensation techniques, of stitching errors produced during the electron-beam lithographic patterning process [11]. Compact single-row PhC structures embedded in PhW waveguide micro-cavities could become essential components for wavelength selective devices, especially for possible applications in WDM systems [22-24] and also in non-linear and slow light experiments [35-38]. Compact micro-cavity optical filters can be produced by inserting a short spacer section between photonic crystal mirrors. Moderately high resonance Q-factor values are needed for possible applications such as wavelength de-multiplexing, non-linear behavior [25] and all-optical switching [26]. The very high Q-factor values achieved in some recent work [27] are not necessarily useful in practical situations such as DWDM telecommunications where the channel separation (e.g. 50 GHz) is typically much larger than the full-width half-maximum (FWHM) of approximately- 200 MHz that corresponds to a Q-factor of 1 million. Recently Q-factor values as high as 8,900 have been obtained for the type of device structure considered in the present *Chapter* - by tapering the photonic crystal mirrors inside the cavity, as reported in reference [28]. The high quality factor and confinement of light in a small volume, V, are important for optical signal processing and filtering purposes, implying large Purcell factor values. Early work by Foresi et.al [12] demonstrated micro-cavity operation with two identical periodic hole mirrors embedded in a suspended photonic wire type waveguide - and a quality-factor (Q-factor) value of 500 was obtained. Since then, large increases in Q-factor have been obtained by tapering carefully within the cavity, thereby reducing modal mis-match effects at the interfaces between the PhC mirrors and the cavity spacer section [13-14, 31-34, 44]. At the same time, it was shown that the length of the cavity spacer section must be adjusted precisely to obtain the best results. A growing interest in designing high-Q, photonic-wire embedded in photonic crystal micro-cavities has therefore emerged [15,16], although only moderately high Q-factor values, such as ~18,700, together with sufficiently large transmission, approximately 85% in our case [17], are sufficient for possible applications such as Dense Wavelength Division Multiplexing (DWDM) - and non-linear optical functionality such as all-optical switching. Although, in some work, a Q-factor as large as $10^8$ has already been achieved in different configurations, such as micro-toroids [40], micro-discs [41], Photonic Crystal Cavities [42-43], but the much larger

modal volumes of some device [40] gives Q/V values of approximately $5.10^4(\lambda/n)^3$. On the other hand, Q-factor values as high as $10^6$ were also achieved [42-43] in micro-cavities that were fabricated on membranes Thus there has been a race toward designing ultra small micro-cavities structure with extremely high Q-factor value that can offer small modal volume, close to a theoretical limit of $V= (\lambda/2n)^3$. In some recent work [16], a Q of 58,000 with the modal volume of approximately $0.6(\lambda/n)^3$ has been achieved but the optical transmission at this resonance condition was rather small. Therefore, this chapter will describe the detailed design and characterization of ultra-small PhC/PhW device structures that exhibit high quality-factors with large optical transmission fators - which will be practical for some telecoms applications, as already mentioned. They are realized through the introduction of tapering both within and outside cavity, with several holes of different sizes and spacing.

## 4.2        1D Photonic Crystal/Photonic Wire Devices

### 4.2.1        The Initial Design of Mirrors

Photonic crystal (PhC) mirror structures consisting of several periods of identical and periodically spaced holes with various diameters, $d$, and periodicity, $a$, were embedded in photonic wire waveguides.
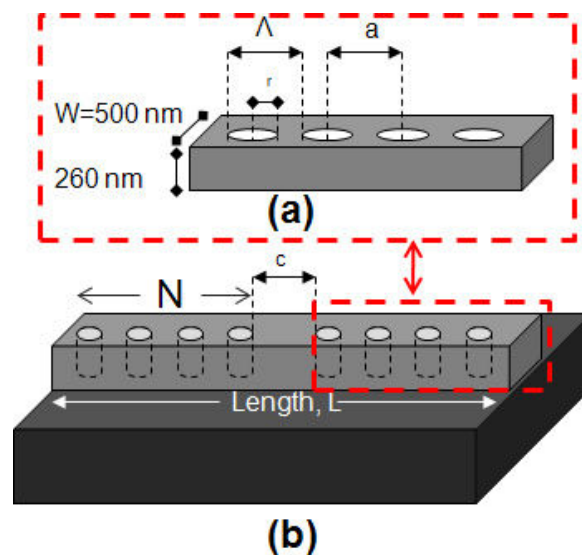


**Fig. 4.1:** (a) *The schematic drawing of the PhC embedded on the wire using standard conventions/parameters (b) The dimension of the device used for 3D-FDTD PhC simulation*

The structure modelled had N holes embedded in a 500 nm wide silicon core with a thickness of 260 nm. Silica of thickness 1 μm was used as a buffer layer below the silicon core as shown in *Fig.4.1 (b)*. The description of the mirrors and micro-cavity is defined by the standard convention/parameters: hole radius (*r*), hole diameter (*d*), periodic (*a*), grating period (Λ), wire width (*w*), cavity inside spacer dimension (*c*) and number of periodic mirror holes inserted (N), as illustrated in *Fig.4.1 (a)*.

The basic structure forming the mirrors shown in *Fig. 4.1* was simulated using both 2D and 3D versions of the finite-difference time-domain (FDTD) approach. For 2D FDTD, the effective index method was used to calculate the average refractive index of the simulated device. The value of effective index, $n_{eff}$ of 2.97 is constantly used throughout this work- which was calculated using Fimm-wave ® simulation tool. On the other hand, for 3D FDTD simulations, the values used for the refractive indices of the silicon core and the silica buffer layer were 3.45 and 1.45 respectively - where the actual dimensions of the device considered for the 3D FDTD modeling are shown in *Fig.4.1 (b)*. This device was designed for operation at around 1520 nm.

An Initial investigation of the basic properties of the mirror consisting of several periodic structures, without any spacer/micro-cavity section placed between the mirror sections was conducted. This investigation was crucial for optimization of the performance of the device by varying parameters such as the hole diameters, periodic spacing and the number of hole used in the mirrors before introducing the spacer in the latter to form a micro-cavity. Those parameters are very importance in order to couple and trap light strongly and efficiently within the cavity region.

Based on the initial design shown in *Fig.4.1*, 2D and 3D FDTD simulation has been carried out for the design, without and with a micro-cavity present. For the case where no cavity was introduced, the investigation has concentrated on the characteristics at the band edge and the way that it behaves - as some parameters such as hole diameter and periodic spacing between the hole, are varied. The total length, L of the device required to produce reflectivity is much shorter than that of comparable Bragg grating structures [47]. In other word, a much smaller number of holes is required to produce strong mirror reflectivity, as compared to the external 'teeth' grating as already discussed in Chapter two.
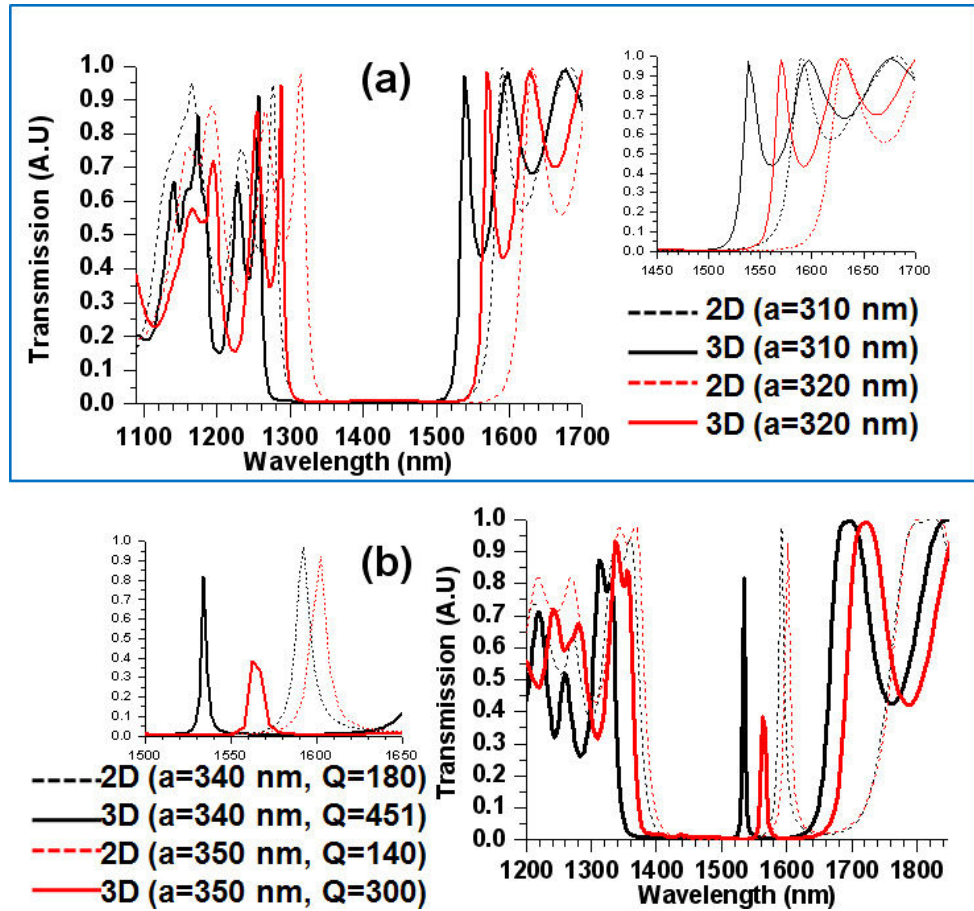
**Fig. 4.2**:*2D and 3D FDTD computed spectra for device (a) without micro-cavity and N=12 (b) with micro-cavity and N=6 (periodic mirrors at each side of the micro-cavity) where c=400 nm.*

*Fig.4.2 (a)* shows a comparison of 2D and 3D simulations for a 12-hole periodic structure that does not have the spacer section required for micro-cavity behavior. This structure has been produced using periodic hole (centre-to-centre) spacing of 310 nm and 320 nm, selectively. The stop band width obtained in the simulation was 280 nm for 3D computation and 300 nm for 2D computation. This difference is to be expected, since 2D FDTD calculation were based purely on estimation of the refractive index by taking an average refractive index of the SOI, whereas 3D FDTD results were calculated on the basis of actual device structures - where the actual refractive index values of the material and of its surroundings were used, rather than just estimation. In addition, 10 nm variation of the periodic spacing of the hole produces a shift of 30 nm and 40 nm in the stop band edges in the case of 2D and 3D FDTD respectively. Based on the results, the middle of the stop band lies around the

wavelength of 1400 and 1440 nm, respectively. From this simulation result, the stop band can obviously be tuned by varying the hole periodic spacing. Therefore, in order to tune the stop band to the wavelength of interest, which in this case is around 1550 nm, bigger estimated hole spacing of around 350 nm is required. Thus the middle of the stop band is shifted the middle of the stop band to be around the wavelength of 1550 nm. The correct choice of hole periodic spacing is important for the next stage of the design work, when the spacer is introduced symmetrically in the middle section of the periodic mirror - thus producing a sharp resonance peak that lies in the middle of the stop-band around the wavelength of interest of 1550 nm. *Fig.4.2 (b)* shows a comparison of 2D and 3D computational results for a structure when the spacer is introduced in that particular device with c=400 nm. The cavity is inserted between two periodic mirrors with N=6 for the case of hole periodic spacing of 340 and 350 nm. A sharp resonance transmission peak appears around the middle of the stop-band at a wavelength of around 1535 nm and 1565 nm, based on 3D FDTD in respect to the hole periodic spacing of 340 and 350 nm- with a shift of approximately 30 nm in the resonance wavelength for a 10 nm increase in the periodic hole spacing. The Quality factor values for that particular resonance peak are calculated to be 300 and 451. On the other hand, with reduced time and power consumption, 2D FDTD shows higher transmission, with Q-factor values of around 140 and 180 for periodic spacing of 340 and 350 nm, respectively. In this section, it is shown that 3D computational result shows a more pronounce and predictable trend, with transmission less than 50% and a Q-factor of around 400. A correct choice of hole diameters and periodic spacing also plays an important part in calibrating the resonance peak to the wavelength of interest of around 1550 nm. This performance can be further enhanced by means of tapering within and outside the cavity, which will be discussed in the later section.

### 4.2.2      Early results

The devices were fabricated using standard direct-write electron-beam lithography and dry-etching processes – and the process parameters were adjusted to reduce sidewall roughness. *Fig.4.3* shows a scanning electron micrograph (SEM) of the device after etching, with nominal dimensions of $r = 75$ nm, $d = 150$ nm and $a = 320$ nm. The device was measured using a tuneable laser covering the range from

1457 nm to 1583 nm. TE polarised light was end-fired coupled in and out the waveguide. The signal is detected using Germanium photodiode. The laser source used for this experiment had a limited wavelength scanning range of 1450 nm to 1580 nm. Since the predicted stop-band is bigger than the available range of the laser source, it is only possible to see the band edge of the stop band for filtering analysis purposes.
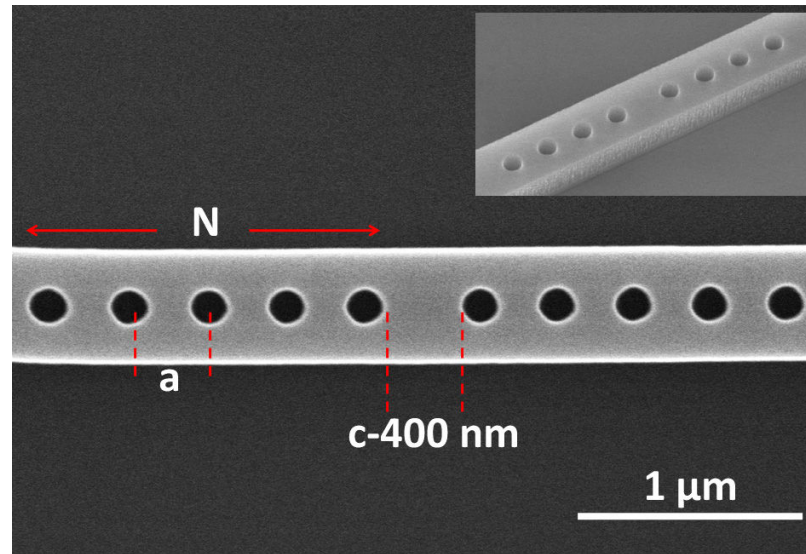


**Fig.4.3:** *Scanning electron micrograph (SEM) of the photonic crystal consisting of N hole mirror embedded in the 500 nm wire waveguide with cavity length, c. (inset is the "bird's-eye" view of the device with smooth sidewall). In this particular example, N=5 and a=370 nm.*

This band-edge shows that stop-band filters can be controlled at by using different hole periodic spacing. *Fig.4.4 (a)* shows experimental transmission measurements of the stop-band for rows of 12 periodic holes, with slightly different periodicity values. A shift of 30 nm in the band-edge transmission is observed for 10 nm variation in the periodicity. Furthermore, 3D FDTD computation *(see Fig 4.2(a))*, shows good agreement of the band-edge position with the measured transmission as shown in *Chapter 2 (section 2.2)*. For instance, it also shows a small deviation of the wavelength at the stop-band edge by approximately 5-10 nm. In contrast, 2D simulation shows much bigger deviation, more than 50%, in comparison with the measured transmission. Furthermore, increasing the periodicity of the row of holes by

10 nm, resulted in a small shift of the entire stop-band as well as resonance by approximately 20 nm. This shift of the stop band in particular is due to the increase in the total length of the periodic mirror. As the period of the hole structure increases to 390 nm, the band edge moves to a higher frequency. *Fig.4.4 (b)* shows the experimental transmission of a PhC micro-cavity inserted between mirrors with N = 6 periods. The same characteristics at the band-edge are observed for this case, where different periodicity causes a shift in the resonance peak, as predicted by both 2D and 3D computation.
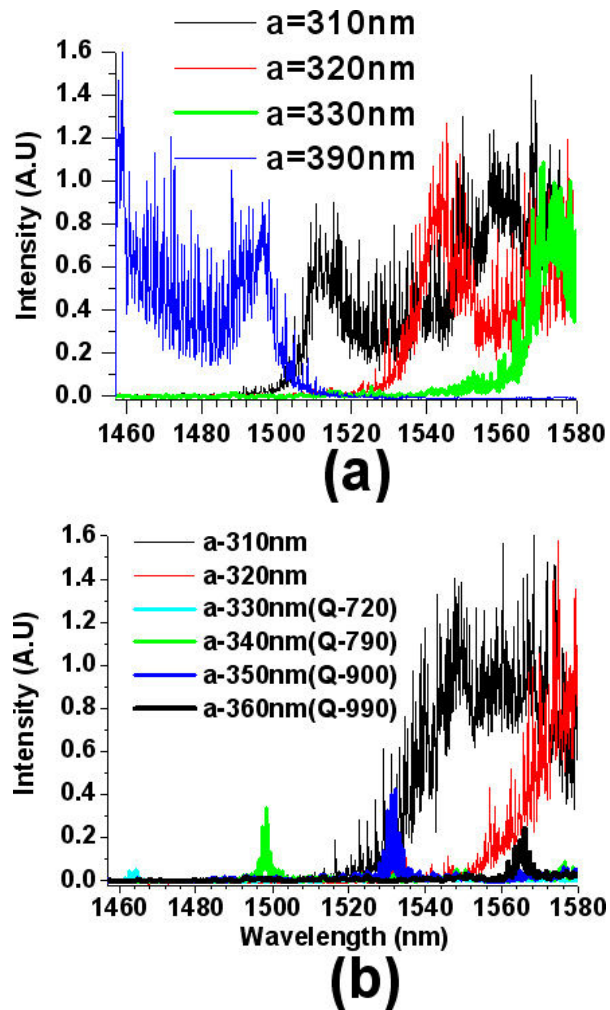


**Fig.4.4***: (a) Measurement for N=12, d=150 nm with different periodicity, a (b) Measurement of a single cavity with N=6, d=150 nm, c=550 nm at different periodicity, a*

As the periodicity is varied in 10 nm steps, the resonance peak also shifts by 30nm towards longer wavelengths – and with an increased in Q-factor value. In other

words, varying the cavity size will shift the resonance and change the Q-factor of that particular cavity. As predicted by 3D computation, increasing the size of the cavity between the mirrors produces a resonance peak with reduced Q-factor. A Q-factor of 990 has been observed for a = 360 nm. This value is slightly higher than that predicted by 3D computation, which is probably due to running the simulation at low resolution in order to reduce the computational time taken for a single run. The measured transmission also shows shifts in the resonance towards the band-edge by 30nm, for a 10 nm variation in the hole periodicity. In practice, although the 3D simulation give a better idea of the required device dimensions for the device, but the fabrication runs typically show a variation of 30-60 nm in the structure dimensions (measured using Scanning Electron Micrograph- SEM) including the hole diameters, periodic spacing and cavity length from the actual design. It is therefore essential to bracket the hole diameter, the hole periodic spacing, a, hole diameters, d and cavity length, c for each fabrication run.

## 4.3        Mode Mismatch in 1D PhC/PhW Devices

The mode mismatch at the interface between the PhC waveguide region and the unstructured photonic wire waveguide is known to contribute to the problem of obtaining high Q-factor values of PhC micro-cavities. This problem is mainly due to the significant reflection and scattering losses that occur at the abrupt transition for the mode when going from the unstructured wire guide into the PhC hole mirror regions. Therefore gradual modal conversion is needed via the use of rows of holes of different diameters and spacing at the transition between the unstructured wire waveguide and the PhC hole mirrors (taper outside cavity), as well as at the transition between the PhC mirrors and the micro-cavity spacer region (taper within cavity). Lalanne and co-workers [13] have proposed a model where losses originate from the modal mismatch with the existence of genuine non-leaky guided modes. In addition, the leaky mode also contributes towards losses, as light travels from the un-patterned wire into the mirror sections. In the case of 1D PhC hole structures, the vertical and lateral size are optimized in order to obtain as smooth as possible modal transition. The Lalanne model assumes that the field in the PhC waveguide is a linear combination of a propagating PhC mode in each of two contra-directions.

According to this model, the losses due to the incident wave travelling from the wire waveguide into the PhC hole structure has experienced triple scattering process where:

- The incident wave is first scattered into the PhC mode propagating in the positive z-direction with efficiency, η
- This PhC mode is coupled back into the counter-propagating PhC mode without any loss
- This counter propagating PhC mode is scattered back into the wire waveguide with efficiency, η (reciprocity theorem and symmetry of the structure)
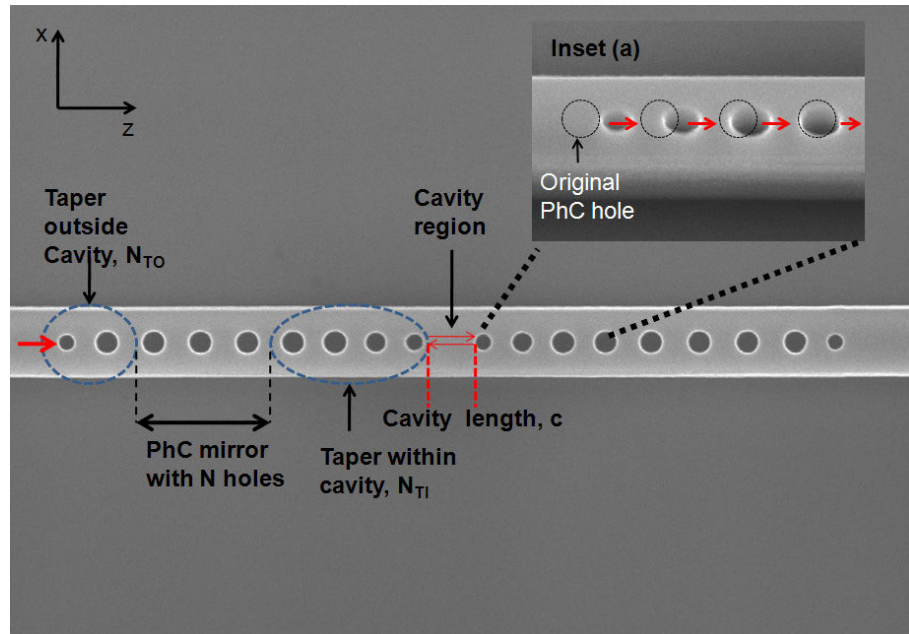


**Fig.4.5:** *SEM image and a schematic drawing of 1D PhC/PhW device structures showing tapering both within and outside cavity to enhance both transmission and Quality factors with inset (a) SEM image of a taper structures with a change in a hole diameter and a shift of the initial PhC hole mirror and inset*

The model of Lalanne and co-workers [13] has shown that by using only tapering within the cavity, a significant increase in the Q-factor value, approaching 60 000 can be obtained, but the normalised optical transmission reported for cavities with this Q-value is very low [16, 28]- approximately less than 20% transmission. This concept has been used in the design of the 1D PhC micro-cavity structures with the convention

used throughout the present work being based on the definitions superimposed on the SEM image shown in *Fig.4.5*. The tapering using different hole sizes helps in reducing the modal mismatch at the entrance of the un-patterned wire, since the effective index at that particular interface changes gradually, as it enters through smaller holes into the mirror region. This gradual interchange reduces losses significantly, so as to preserve the optical transmission as well as Q-value. The requirement of using tapered PhC hole structures with hole diameters smaller than those used in the PhC mirrors is obligatory. The smaller holes provide an equivalent of a dielectric layers with progressive changes in the effective indices of the fundamental mode of the impinging wave travelling from the conventional wire waveguide into the PhC mirror. On the other hand, the mode matching approach will match the fundamental mode of the ridge waveguide to the evanescent mode of the mirrors and also will match the evanescent mode of the mirror to the cavity mode in the spacer section. The evanescent mode is laterally confined within the waveguide, due to the high index contrast between the silicon and its surrounding cladding.

Using gradual graded hole tapers both outside and within the cavity help to retain the fundamental mode travelling from the ridge waveguide into cavity section and finally the output section. Tapering within the cavity section used in the present work consists of several holes of different diameters and spacing between them. In other work [16], the use of a tapered hole arrangement within the cavity has shown an enhancement of Q-factor approaching 60,000 – but the transmission at this resonance condition is rather small, i.e. less than 20%. In the work of reference [16], variation of the number of periodic mirror holes has significantly contributed to this result – where the Q-value increased, together with a reduction in the optical transmission. Therefore to maintaining the optical transmission, while at the same time enhancing the Q-factor, is necessary, or at least desirable, for use in telecommunication applications such as WDM, switching and non-linear optics. This is where the design of tapering outside cavity plays an important role in maintaining the optical transmission. In the present work, a combination of tapered arrangements will show further effective enhancement in both the Q-factor and the optical transmission.

### 4.3.1 Device Optimisation- Tapering Within and Outside the Cavity

Optimization of the actual hole dimensions used in the tapered section is the most crucial part of obtaining high performance in terms of high optical transmission and large resonance Q-factor. Tapering of the holes used within the cavity effectively enhances the Q-factor of the resonance. Initial 2D and 3D FDTD simulations used to investigate the effect of inserting such taper structures into the mirrors have shown further enhancement in optical transmission and Q-factor value – although at this point the Q-factor calculated was still low.
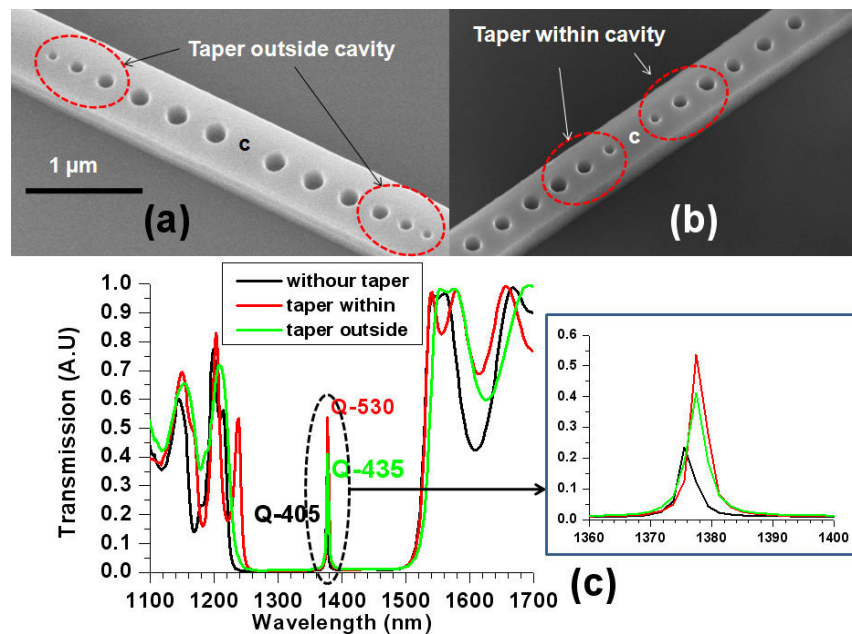


**Fig.4.6:** *(a) SEM image of a taper outside the cavity (b) SEM image of taper within the cavity (c) 3D computed transmission of single cavity with different taper structures (inset is the close up of the resonance peak for each taper arrangement)*

In comparison, a 3D FDTD computation can provide more accurate results than 2D FDTD, when compared with the measured results. But due to the power and time consumption issues discussed in *Chapter 2 (section 2.2),* 2D computation is the preferred approach for obtaining a preliminary assessment of the behaviour of the device structures before the 3D approach is implemented. *Fig.4.6 (a) and (b)* show SEM micrographs of a typical device with taper structures embedded outside and within the cavity. From 3D FDTD computational results, tapering outside the cavity-

as shown in *Fig.4.6 (b)* has increased the computed transmission by a factor of two. The computed transmission is further increased, by another 25%, as the taper within the cavity is introduced – as also shown in *Fig.4.6 (b)*. Furthermore, the Q-factor of a particular resonance has increase significantly to 530 as compared with a value of 405 for the structure without tapering effects.

Therefore, at this point, 3D FDTD computation has shown that either form of tapered structure used provide a suitable platform for designing device structures that exhibit large resonance Q-factor, together with high optical transmission. By using tapered holes within and outside the cavity separately it has been shown that a significant increase in the Q-factor value, by 95, can be observed for the case of tapering within the cavity. Whereas tapering outside the cavity has produced a small increase in the Q-value, of approximately 30. Therefore tapering outside cavity does not have much impact on the Q value. But the combination of both tapering arrangements has the capability of improving the optical transmission by as much as 50%. Therefore a combination of both tapering within and outside cavity can have a high impact on both improving Q-value as well as optical transmission by using a correct combination of hole diameters, aperiodic spacing and cavity length of the tapered hole. The detailed of design is discussed in the *next section*. Computation has shown convincingly that enhancing the transmission and resonance via tapered hole structures is very important. At this point, the measured device has shown a good controllability of resonance and small enhancement of transmission at the resonance peak by means of different hole tapered arrangement.

Moreover, improvement can be obtained, in terms of increased light throughput and the Q-factor of the resonance peak by tapering within the cavity and also between the cavity mirrors and the exterior waveguide sections, as predicted by 3D computation. For instance, the Q-factor and transmission of the device are mostly determined by the cavity length, the arrangement and hole diameters in the tapered sections. Therefore, it is very important to find the correct parameters for the design, in order to enhance the Q-factor and transmission spectrum. The number of periodic mirror holes outside the taper regions – and the deliberate variation of the hole diameter within the taper regions also play an important role in determining the behaviour of the transmission and the Q-factor. Longer cavities and multiple cavity

arrangements with taper structures are expected to play a significant role in increasing the optical throughput as well as the Q-factor.

On the other hand, 2D and 3D computational simulation give a predictable trend for the actual device behaviour. 3D computational results gave closer with the results for measured devices compared to 2D computational method. Improvement can be made, in terms of increased light throughput and of enhancement of the Q-factor of the resonance peak, by tapering within the cavity – as predicted by 3D computation. For instance, the Q-factor and transmission of the device are mostly determined by the size of the cavity, hole diameter and the arrangement of the taper. Therefore, it is very important to find the correct parameters for the design, in order to enhance the Q-factor and transmission spectra. The number of periodic mirror holes outside the taper region and the different hole diameters within the taper region also play an important role in determining the transmission and the Q-factor. Use of a longer cavity and multiple cavity arrangements with the tapered structures previously mentioned are expected to play a significant role in increasing the light throughput, as well as the Q-factor.

## 4.3.2　　　Taper: The Final Design

The tapered hole sections used in the present work are based on developing a design for a variable PhC structure with holes of different size and centre-to-centre distance, in order to minimize the propagation losses at the interface between a narrow photonic wire waveguide, in particular one that is 500 nm wide and the PhC mirror sections - thus enhancing both the Q-factor and the optical transmission. An appropriate choice of aperiodic hole dimensions is necessary at the transition regions to provide a gradual effective index change into the mirror region. To minimise the losses, this design uses holes of different diameters, with progressive hole size variation. The smaller holes effectively generate artificial dielectric layers with progressively varying effective indices. The smaller holes used at the entrance to the mirror will effectively reduce the modal mismatch - thus enhancing the optical transmission as well as, possibly the Q-factor value. The tapered hole structure design considered in the present work is shown in *Fig.4.7*. This taper is used at the entrance of the conventional 500 nm un-patterned wire waveguides into the periodic mirror

sections, which have hole diameters of d=182 nm and periodic spacing a, of 350 nm.
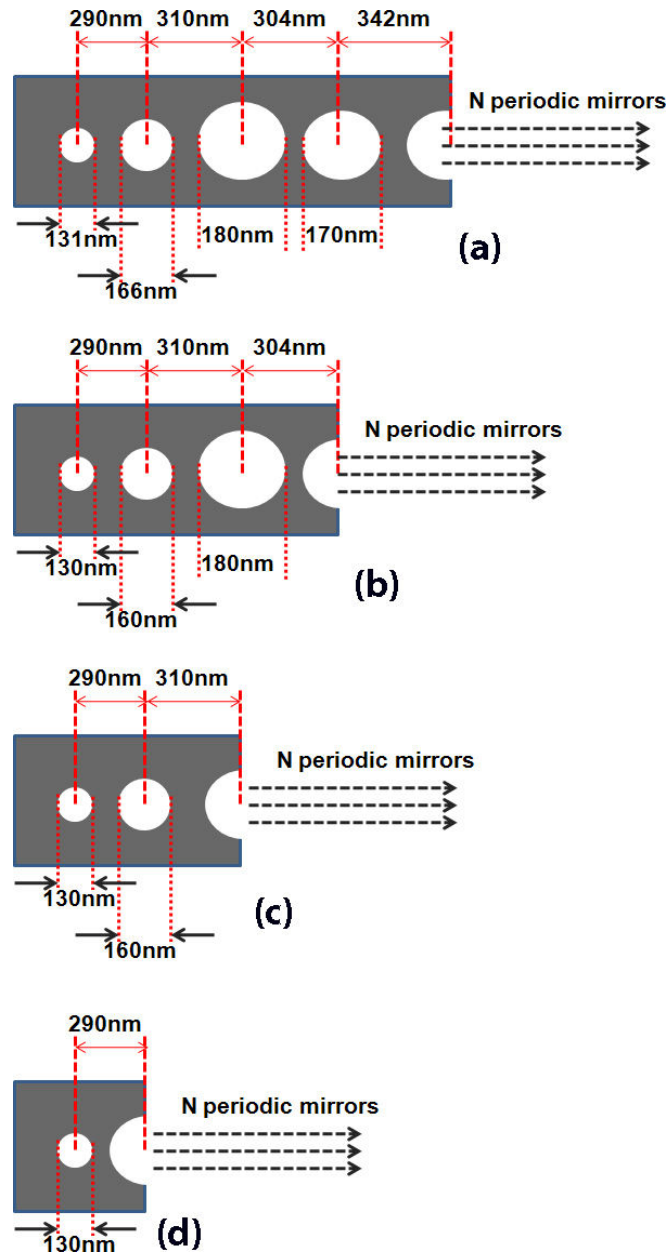


**Fig.4.7:** *The proposed design for the tapered hole of different diameters and aperiodic spacing used in this present work with (a) four hole taper (b) three hole taper (c) two hole taper (d) one hole tapered*

The choice of that particular hole arrangement in the periodic mirror regions is due to the appearance of the middle of the stop band, together with the resonance peak produced - which fall within the optical wavelength range of around 1520 nm (*see Fig.4.4 (b))*. This choice is important since the characterisation tool – a tuneable laser

- used throughout the present work has a limited range, of between 1457 nm and 1583 nm. The tapered hole structure used in this work will provide an insight for the analysis of the behaviour of the resonance peak produced, especially in terms of the optical transmission and Q-factor value.
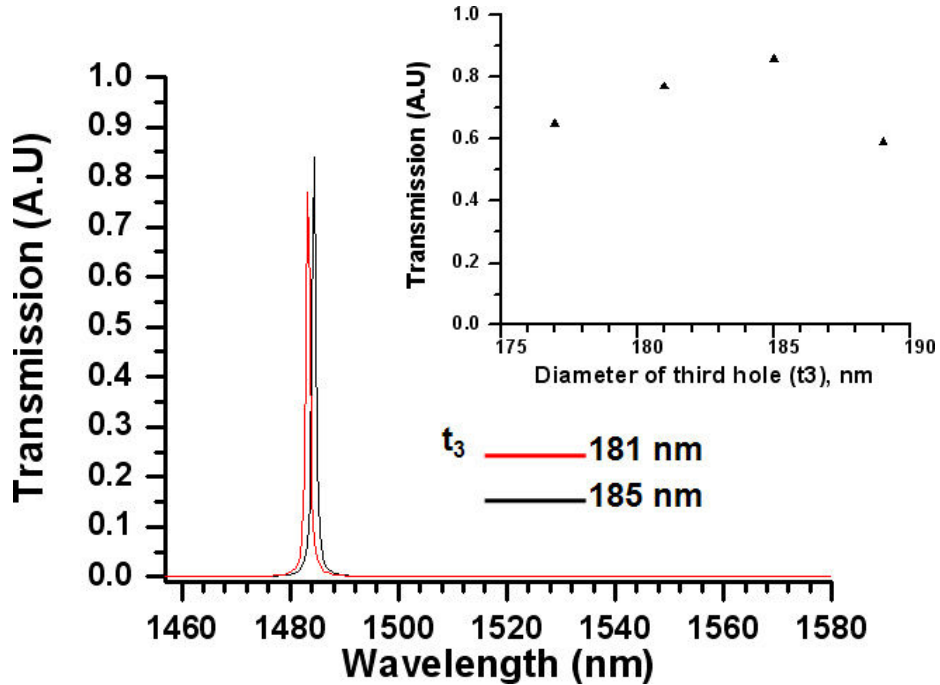


**Fig.4.8:** *2D FDTD calculation for different hole size used for $t_3$ (third hole) for c=400 nm, N=4 and $N_{TI}$=3 without tapering outside cavity, $N_{TO}$ and N with Q-factor of approximately 3000 in all cases.*

If the number of holes used in the aperiodic tapered section is three or four, then the optimisation is concentrated on the third hole, namely $t_3$ , since the bigger holes used will have a significant effect on the Optical transmission, i.e. where an increase in the transmission of approximately 10% is calculated, as shown in *Fig.4.8*. But no significant effect on the Q-factor value is estimated from having bigger holes in $t_3$

### 4.3.3        Effect of Tapering Within and Outside Cavity:

Tapering within the cavity has been convincingly shown to have a significant impact on the Q-factor value. By using only hole tapering within the cavity- and with no hole tapering outside the cavity - it was possible to use  2D FDTD simulation to look at the impact of having different numbers of holes in the periodic mirror sections. The results of this investigation are shown in *Fig.4.9 (a)* where, as the number of periodic mirror holes, N, increased from three to eight, an enhancement of the Q-value was

obtained. The drawback is that a rapid reduction in optical transmission is also observed, whereas the highest optical transmission was calculated at N=4. The optical transmission was reduced to approximately 11% - but with a high Q-factor value of approximately 15,000. Enhancement of the optical transmission is obtained for N=4 with $N_{TO}$=2, where the optical transmission obtained is approximately 85%.
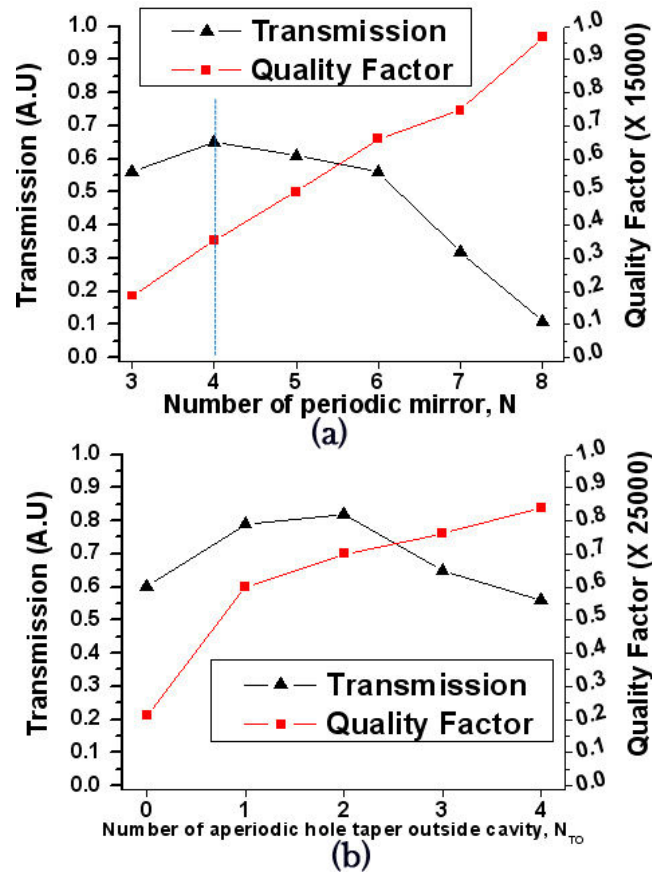


**Fig.4.9:** *2D FDTD calculation for $N_{TI}$=4, c=400 nm showing a variation of optical transmission and Q-factor value for (a) different number of periodic mirror holes without any tapering outside cavity (b) for N=4 with different number of aperiodic hole taper used outside cavity in conjunction with the taper design shown in Fig.4.7*

This optical transmission is obtained together with the high Q-factor value of approximately 17,500, as shown in *Fig.4.9 (b)*. It is also shown that, integration of tapering outside the cavity helps in preserving an optical transmission factor of more than 50%. Therefore, it is important that to use the correct choice of hole dimensions in the periodic mirror sections - and both tapering within and outside cavity helps with retaining the high performance of this particular type of device structure.

**4.4** **High-Q and Large Transmission PhC/PhW Micro-cavities**

**4.4.1** **Results and Discussions of using one hole tapered outside cavity**

Achieving high Q-factor values, together with large transmission, depends very much on the choice of the correct hole parameters including hole diameters, the periodic spacing of the hole mirrors, aperiodic spacing and holes of different size in the tapering section - and cavity length. Optimization has been carried out – in which different combinations of periodic sections hole and aperiodic taper arrangements have been investigated. In order to reduce the modal mismatch within the cavity, the number of aperiodic tapered holes within the cavity is optimized to four, while reducing to just one hole in the tapers outside cavity. This structure, consisting of a single hole for tapering outside the cavity gave a significantly larger value for the Q-factor at certain cavity lengths as compared to the result with medium Q-factor reported in [39]. The tapered hole sections, outside and within the cavity, have two and four aperiodic holes of various diameters and centre-to-centre hole distance respectively, A 3D Finite-Difference Time-Domain (FDTD) modeling approach has been used to simulate the device.
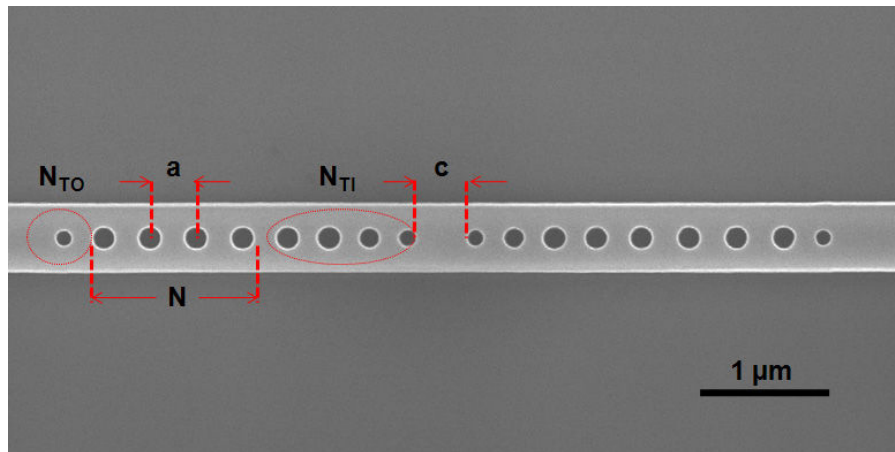


**Fig.4.10**: *SEM image of the device with one hole tapered outside cavity embedded in a 500 nm PhW waveguide with period, a (centre-to-centre hole distance), cavity length, c (inside length between the two holes in the middle of the periodic mirrors) - and taper regions with a number of aperiodically located holes*

A photonic crystal mirror structures consisting of four periods of holes with diameters, *d*, of 182 nm and periodicity, *a*, of 350 nm were embedded in a 500 nm

wide, rectangular cross-section, silicon photonic wire with a thickness of 260 nm as previously mentioned briefly in *section 3.1.1.* In *Fig. 4.10*, two sections, each using four aperiodically-located and tapering holes within the cavity have been used, with respective hole diameters of 170 nm, 180 nm, 166 nm and 131 nm – with centre-to-centre hole distances of 342 nm, 304 nm, 310 nm and 290 nm, respectively. Whereas one-hole aperiodic tapered sections outside the cavity have- hole diameters of 130 nm, with centre-to-centre hole distances of 290 nm have been used. This arrangement will later on be used as the basic parameters for the aperiodic holes used in the tapering sections (within and outside the cavity) of the devices.
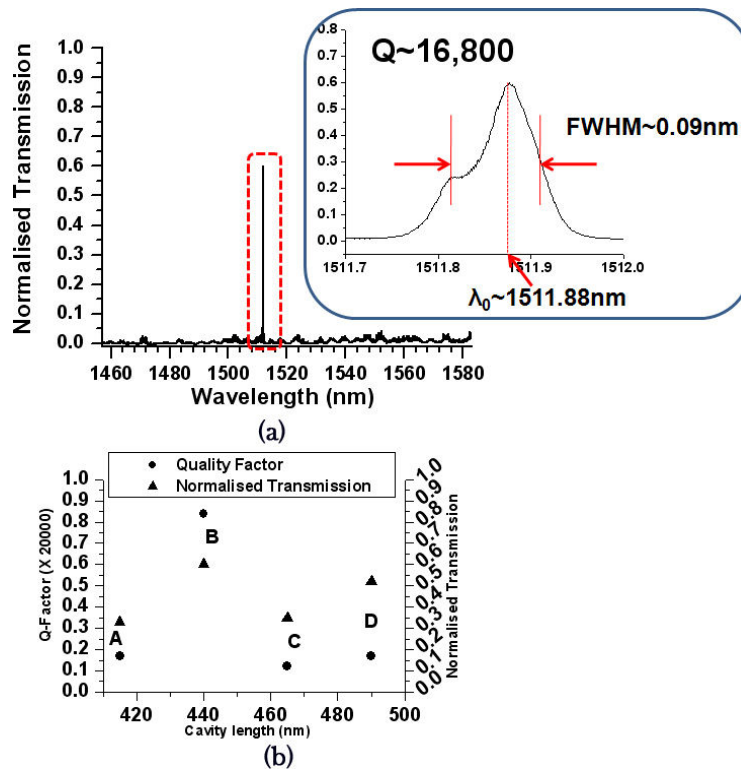


**Fig.4.11:** *(a) Measured result for tapering arrangement shown in Fig.4.10 with cavity length=440 nm (inset: the expanded horizontal scales of the resonance) (b) Variation of Q values and normalized optical transmission at various cavity lengths,c for this device structure with A (c=415 nm), B (c=440 nm), C (c=465 nm) and D (c=490 nm).*

Based on this design structure, a variation in cavity length and number of holes in the taper will be investigated further, which corresponds to the change in Q-factor and optical transmission. In this particular design where N=4, $N_{TO}$=1 and $N_{TI}$=4 – *see*

*Fig.4.10*, the measured results for the one-hole exterior taper arrangement are shown in *Fig.4.11* with a significant improvement on the Q-value at cavity length, c= of 440 nm.An estimated value of a Q factor of 16,800 has been measured for this device at a cavity length of 440 nm. A normalized transmission of around 60% at the resonance wavelength of 1511.88 nm and FWHM~0.09 nm have also been obtained with this particular cavity length. The Q-factor values measured at cavity lengths of 415 nm, 465 nm and 490 nm respectively were 3400, 3000 and 2400 - at resonance wavelengths of 1498.31 nm, 1528.36 nm and 1549.62 nm respectively. The normalized transmissions at this particular wavelength were measured to be approximately 30%, 35% and 50% respectively-see *Fig-4.11(b)*. The trend of the resonance is different, when compared to the previous design arrangement. In this design, the high Q-factor value was only obtained at the cavity length, c, of 440 nm. Therefore, carrying out a formal optimization on the device could be a good approach in order to investigate the characteristics of different tapered hole arrangement to maximize the Q-values and optical transmission for this particular design.

### 4.4.2        Results and Discussion for two hole tapered outside cavity

On the other hand, as one more hole is added at the tapering section outside cavity, further enhancement is obtained. The performance enhancement obtained is partly due to further reductions in modal mis-match effects at the interfaces between the un-patterned photonic wire and the PhC cavity region, as mentioned in references.
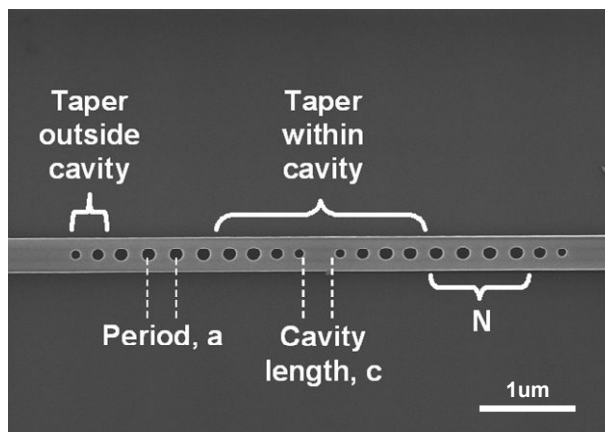


**Fig.4.12:** *SEM image of the tapered PhC micro-cavity embedded in a PhW waveguide with period, a (centre-to-centre hole distance) of 370 nm, cavity length, c=400 nm - and taper regions with a number of aperiodically located holes where $N_{TI}$=4 and $N_{TO}$=2 and N=4.*

In certain limited ranges of cavity length, a combination of these parameters with the hole transition section designed for maximum transmission for light entering or leaving the periodic section - i.e. with transitions both outside and within the cavity, high transmission on-resonance and high resonance Q-factor can be obtained. In this section, the tapered hole sections, outside and within the cavity, have two (taper outside cavity, $N_{TO}$) and four aperiodic holes (taper within cavity, $N_{TI}$) of various diameters and centre-to-centre hole distance respectively, as shown in *Fig. 4.12*.
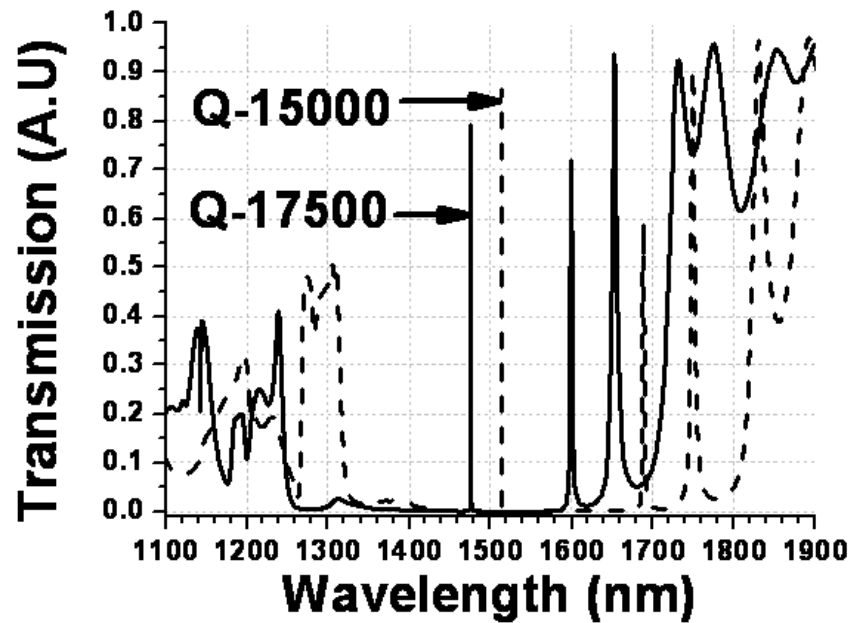


**Fig.4.13**: *Transmission spectra of the tapered periodic mirrors with cavity length, c=390 nm (continuous line-FWHM~0.08 nm) and c=415 nm (dash line-FWHM~0.1 nm) using 3D FDTD method.*

A 3D Finite-Difference Time-Domain (FDTD) modeling approach has been used to simulate the device. A periodic photonic crystal mirror structures consisting of 4 periods of holes with diameters, *d*, of 182 nm and periodicity, *a*, of 350 nm were embedded in a 500 nm wide, rectangular cross-section, silicon photonic wire with a thickness of 260 nm as shown in *Fig. 4.12*. Two sections, each using four aperiodically-located and tapering holes within the cavity have been used, with respective hole diameters of 170 nm, 180 nm, 166 nm and 131 nm – with centre-to-

centre hole distances of 342 nm, 304 nm, 310 nm and 290 nm, respectively. This arrangement is the same as initially introduced in *section 4.3*. Although somewhat surprising, our limited observations and simulation have indicated that upwards and downwards variation in hole size , i.e. the use of 180 nm second hole diameter instead of, for example, 168 nm has given slightly larger Q-factor and transmission values. Whereas the two-hole aperiodic tapered sections outside the cavity have  hole diameters of 160 nm and 130 nm respectively, with centre-to-centre hole distances of 310 nm and 290 nm, respectively. *Fig. 4.13* shows the transmission spectra for this design arrangement computed using the 3D FDTD approach, together with cavity lengths, respectively, of c = 390 nm and c = 415 nm.  A Q-factor of approximately 15,000 was calculated, with the impressive transmission value of nearly 90%, at a resonance peak wavelength of 1517 nm, for the c = 415 nm cavity. On the other hand, a Q-factor of nearly 17,500, with transmission of around 80% was observed for the c = 390 nm case at resonance wavelength of 1476.2 nm. A shift in the resonance frequency by approximately 40 nm was thus obtained for a 25 nm difference in cavity length.
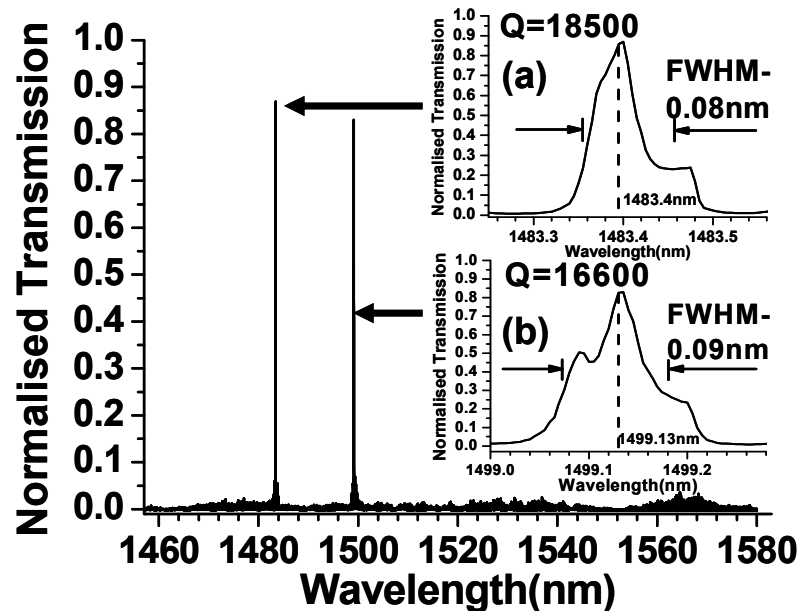
**Fig.4.14**: *Measurement result for (a) resonance frequency at λ=1483.4 nm for c=390 nm (b) resonance frequency at λ=1499.13 nm for c=415 nm*

The experimental results were normalized with respect to an identical, but unstructured, nominally 500 nm wide PhW waveguide without any holes embedded in it. *Fig. 4.14* shows the measured transmission spectrum for a tapered PhC micro-cavity embedded in a PhW waveguide, with cavity lengths of 390 nm and 415 nm - corresponding to the simulation results given in *Fig. 4.13*. The estimated experimental Q-factor values were 18,500 and 16,600, with a measured transmission of around 85% - and these values were obtained at resonance central wavelengths of 1483.4 nm and 1499.13 nm, with FWHM values of ~0.08 nm and ~0.09 nm respectively – see the insets in *Fig. 4.14 (a) and (b),* which have expanded horizontal scales.
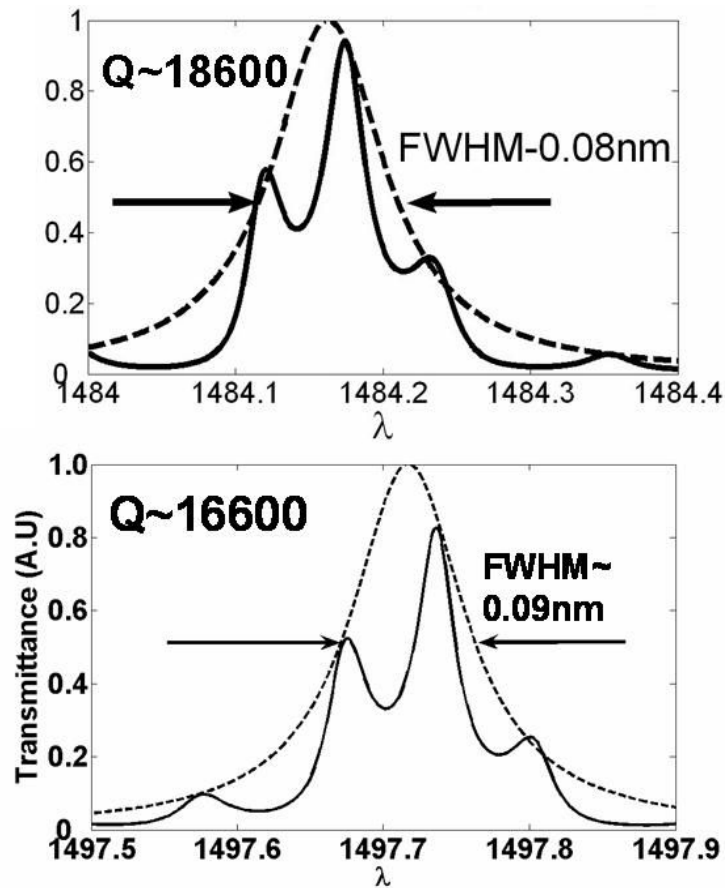


**Fig.4.15**: *Examples of transmittance of a micro-cavity calculated as "isolated" (dashed curves) and embedded in a full length waveguide that matches the experimental dimensions (continuous curves), obtained using a TMM model. The micro-cavity has the cavity length of c=415 nm corresponding to the experimental result of Fig.4.14 (b).*

The distance between the points of the arrows has been used to obtain, in a reasonably conservative manner, the estimates of the resonance quality factors, via the 3 dB points. The ambiguity in extracting the Q-factors from direct experimental measurements is due to the presence of fine structure superimposed on the resonance of the isolated micro-cavity. This fine structure is due to the Fabry-Perot cavity produced by the cleaved end-facets of the waveguides. In order to retrieve the Q-factor of the micro-cavity, a model based on the Transfer Matrix Method (TMM) was also investigated [29, 30]. We have found that a TMM model that matches the experimental dimensions yields a transmission spectrum that remains "enveloped" by the Lorentzian resonance of the micro-cavity-, considered as an isolated device, over a range of plausible Q-factor values as shown in *Fig.4.15*. Therefore the determination of the Q-factor by the approach shown in *Fig.4.14* can be considered as an appropriate procedure.

In addition, optimizing the fabrication process plays an important part in reduced propagation losses due to the sidewall roughness. Furthermore, obtaining accurate patter transfer between the initial design and the fabricated device is also crucial. Even a slight difference in the device dimension will affect the whole performance of the fabricated device.
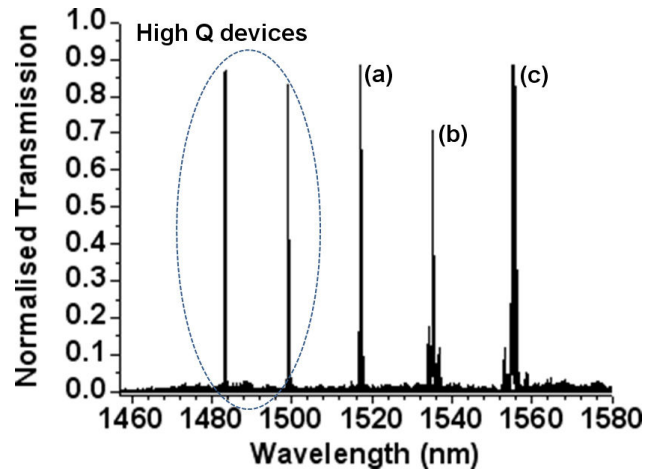


**Fig.4.16**: *Measured transmission of the tapered 1D PhC micro-cavity at different cavity length, for $N_{TI}=4$ and $N_{TO}=2$ (a) c=440 nm (Q~7000) (b) c=465 nm (Q~5000) (c) c=490 nm (Q ~ 3000), the dotted circle one is the previous results shown in Fig.4.14 corresponds to c=390 nm and c=415 nm with Q values of 18,500 and 16,600.*

*Fig.4.16* shows the measured transmission spectra for different cavity lengths, c. Variation of the cavity length by 25 nm give rise to the uniform shift in the resonance transmission towards a longer wavelength. The resonance, appear approximately at the central wavelength, $\lambda_0$ of 1517 nm, 1535 nm and 1555 nm respectively. A shift of 18 nm in the central wavelength of the resonance peak is observed. Q-factor values of 7000, 5000 and 3000 were also measured for different cavity lengths, respectively, of 440 nm, 465 nm and 490 nm respectively - with a transmission of more than 70% in all cases. The Q-factor value progressively decreases from 7000 to 3000 as the cavity length increases by 25 nm, in step with a shift of 18 nm in the spectral position of the resonance peak. It should also be noted that the shift in the resonance peak that corresponds to a 25 nm variation in the length of the cavity is larger in the simulation, at 30 nm, as compared with the measured shift of around 16 nm. This is due to the difference in the dimension of the fabricated device and the actual design by ~6 nm as measured conservatively using the Hitachi S4700 Scanning Electron Microscope (SEM). Therefore, tapering both within and outside the cavity has proven that obtaining high Q-factor values, together with large transmission, is possible with the correct choice of hole parameters in the periodic sections - as well as aperiodic hole arrangements in the tapered sections.

## 4.5       Ultra High-Q: Advancing the performance of PhC/PhW Micro-cavities

### 4.5.1       Design and FDTD simulations

In order to obtain the required high performance in this device, the correct choice of cavity length, the hole diameters and the combination of periodic and aperiodic hole spacing is necessary. Tapering within and outside the cavity through the use of holes of different diameters and aperiodic spacing has been used to enhance the Q-factor, while simultaneously maintaining a useful optical transmission level – i.e. the tapered period and hole diameter transition sections, both outside and within the cavity, were designed to maximize the transmission for light entering or leaving the periodic mirror sections. In this section we report the use of mirrors having N periodically
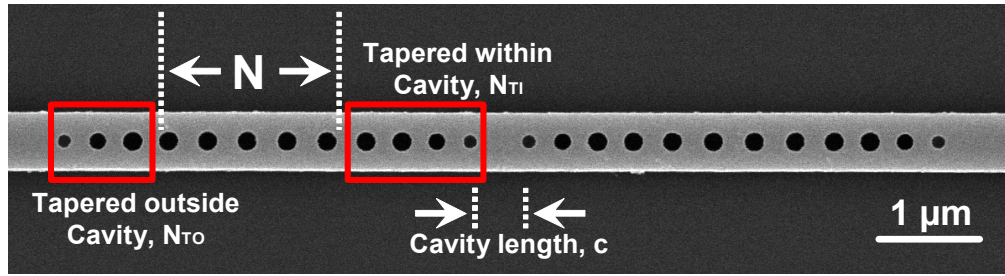
**Fig.4.17**: *Scanning electron micrograph (SEM) image of the tapered PhC micro cavity embedded in a PhW waveguide with N=5, cavity length, c=400 nm, $N_{TI}$=4 and $N_{TO}$=3*

spaced holes,, with diameters of 182 nm and a periodic spacing of 350 nm between them. A scanning electron micrograph (SEM) image of a typical cavity is presented in *Fig.4.17*. The figure shows a 500 nm wide photonic wire micro-cavity formed by two mirrors, each of which includes five periodically spaced PhC holes that have the same diameter. Gradually tapered hole arrangements are used, with different diameters and aperiodic spacing designed to produce a significantly enhanced Q-factor value through reductions in propagation losses and scattering that occur locally at transitions within and outside the cavity.
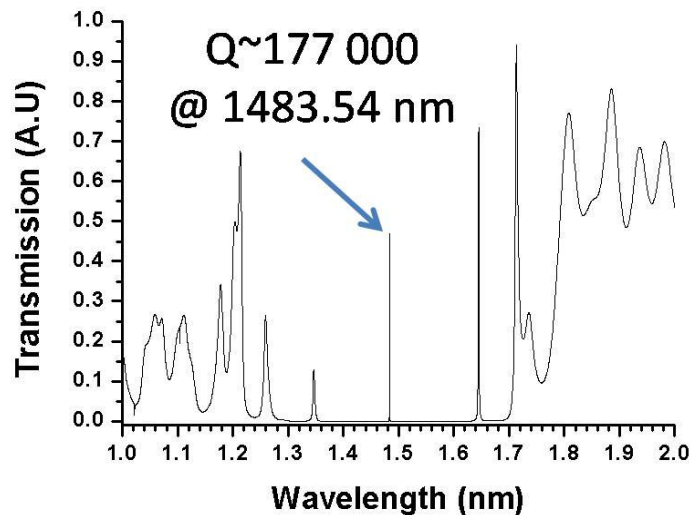


**Fig.4.18**: *Calculated transmission spectrum for N = 5, with $N_{TI}$ = 4 and $N_{TO}$= 3, obtained using a 2D FDTD approach, giving a Q-factor value of approximately 177,000 at a resonance frequency of 1483.54 nm and cavity length, c, of 425 nm.*

Such tapered hole arrangements are made to reduce losses associated with abrupt changes in the modal distribution at the interfaces between the periodic mirror sections and the wire waveguide outside the micro-cavity region, as well as the spacer section within the cavity. Four-aperiodically located and tapered holes form the transition sections within the cavity – and have diameters of 170, 180, 166, and 131 nm respectively — with centre-to-centre hole distances of 342, 304, 310, and 290 nm respectively. – whereas the three-hole aperiodic tapered sections outside the cavity have hole diameters of 131, 166 and 185 nm respectively, with centre-to-centre distances of 275, 305 and 314 nm respectively. A 2D FDTD approach has been used to simulate the device. *Fig.4.18* shows the transmission spectra for this design arrangement, computed using a 2D FDTD approach and assuming a cavity length of ~425 nm. A Q-factor of 177,000 was computed at a resonance wavelength of 1483.54 nm, with a transmission level of approximately 48% at this particular cavity length.

### 4.5.2  Optical Characterization of the High Performance PhC/PhW Micro-cavities

The waveguide patterns were defined using an approximately 200 nm thick layer of hydrogen silsesquioxane (HSQ) negative-tone resist. The devices were fabricated using single-step direct-write electron beam lithography in a Vistec VB6 machine at 100 keV electron energy, with proximity correction at a base dose of 1500 $\mu C/cm^2$. This VB6 beam writer has the capability of writing a 1.2 mm by 1.2 mm field at 1.25 nm resolution. In addition, extra care has to be taken to reduce the potentially significant impact of field stitching errors on the pattern produced – i.e. to ensure the flatness of the sample during the writing process. The patterns were finally transferred into the silicon guiding layer by using an inductively coupled plasma (ICP) reactive ion etching process. $SF_6/C_4F_8$ combined chemistry was used to etch the silicon layer, contributing to obtaining silicon waveguides with smooth side-walls. The devices were characterized using a tunable laser that was capable of covering the wavelength range from 1.45 μm to 1.58 μm.
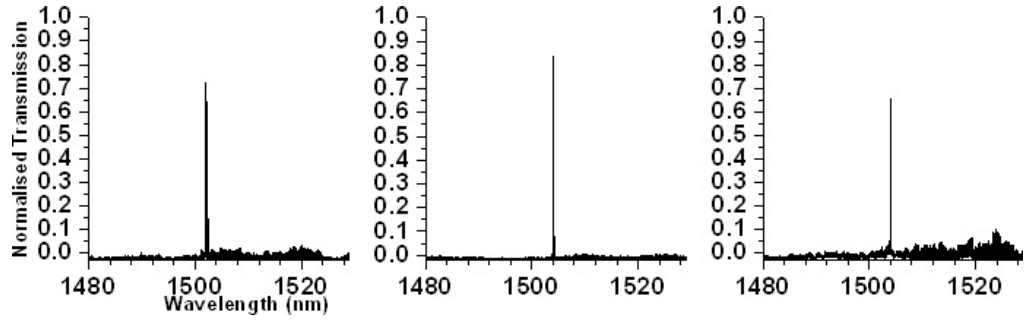
**Fig.4.19**: *Transmission spectra for N = 4 and $N_{TI}$ = 4 with (a) $N_{TO}$=1 (b) $N_{TO}$=2 (c) $N_{TO}$=3 – with a cavity length, c = 450 nm.*

TE polarized light was end-fire coupled into and out of the device waveguide – and the optical signal was detected using a germanium photodiode. The experimental results were normalized with respect to an identical, but unstructured, 500 nm wide wire waveguide without any holes embedded in it. *Fig.4.19* shows measured results for N=4, $N_{TI}$=4 with a different number of holes used in the tapered section outside the cavity. $N_{TO}$ varies from one to three while retaining a cavity spacer length, c, of 450 nm. The measured Q-factor values were 8000, 21,500 and 19,000 respectively, with normalized transmission values of 73%, 83% and 65% respectively. It shows that for N=4, the highest Q factor achieved was obtained with $N_{TO}$=2.
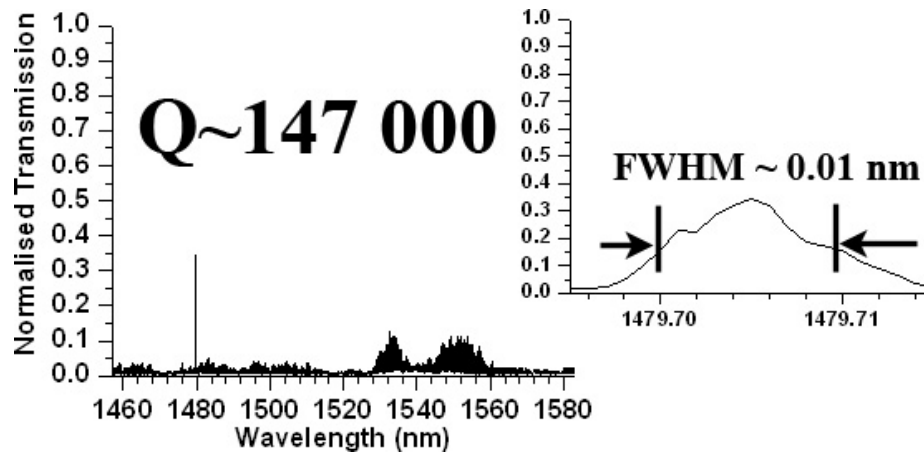


**Fig.4.20**. *Measured transmission spectra for N = 5 with $N_{TI}$ = 4 and $N_{TO}$= 3 corresponded to simulation result in fig. 2 with Q of approximately 147,000 at resonance wavelength of 1479.705 nm*

Further enhancement of the Q-factor value has been obtained through the use of N=5, together with three hole aperiodic tapering outside the cavity and $N_{TO}$ as shown in *Fig. 4.17*. *Fig.4.20* shows the measured transmission spectrum of the device with a

cavity length of 425 nm – corresponding to the simulation result in *Fig. 4.18*, with $N_{TO} = 3$.

**Table 4.1**: *Comparison of Simulated and Experimental value of different taper outside cavity, $N_{TO}$ for N=5 and $N_{TI}=4$*

| $N_{TO}$ | Simulation | | Experimental | |
|---|---|---|---|---|
| | $Q$ | $Tx$ | $Q$ | $T(N))$ |
| 1 | 65,000 | 0.72 | 51,000 | 0.65 |
| 2 | 95,000 | 0.69 | 79,000 | 0.52 |
| 3 | 177,000 | 0.48 | 147,000 | 0.34 |
| 4 | 74,000 | 0.35 | 62,000 | 0.25 |

The estimated experimental quality factor value of ~147,000 was measured at the resonance wavelength of 1479.705 nm, with full width half maximum (FWHM) of ~ 0.01 nm. A normalized transmission of approximately 34% has been measured for this particular resonance. Substantially higher normalized transmission coefficient values have been measured, in conjunction with the somewhat smaller Q-factor value of 79,000 for the particular device with $N_{TO}=2$, as shown in *Table 4.1*. This table also shows a comparison of the simulation and measured results for N=5 and $N_{TI}=4$, using different numbers of holes in the tapered sections outside the cavity, $N_{TO}$. In this particular design, a reduction in optical transmission is observed with additional hole taper sections outside the micro-cavity, together with a significant enhancement in the Q-factor value. This result is probably due in part to the increase in the length of the device, including the aperiodic tapered hole sections that contribute to the increased propagation losses. Although we have also looked at more extended cavities that have longer spacer lengths, the present design retains the use of a short cavity that has a spacer section that is shorter than an optical wavelength in the medium. The Q-factor achievable is strongly dependent on the number of holes in the tapered sections outside the cavity, together with the length of the cavity spacer section.

### 4.5.3 Reproducibility of an Ultra High Performance PhC/PhW Micro-cavities

Optimizing the fabrication process is one of the critical aspects for production of high performance device structures. The process of single step patterning using HSQ resist as a mask for Silicon etching has proven to be reliable as reduction in sidewall roughness has reduced propagation and out of plane scattering losses significantly. This process has been shown to have a very high degree of repeatability, with an estimated average dimensional variation of 1.5 nm, as reported in Section 5.4.1. This result is due to the very high quality of the machines employed, such as the VB6 EBL tool. For instance the STS-ICP machine also features a sophisticated electronic control for the etching process. An important issue that needs to be taken into account towards producing ultra-high Q-factor value micro-cavity devices is their reproducibility and repeatability in term of device fabrication and characterization. Achieving an ultra-high Q-factor value of over 100,000 in the device structures discussed in the earlier section (*section 4.5.2- Fig.4.20 and Table 4.10*) based on different fabrication runs provides a better insight into the device performance. The precision of the fabrication processes needs to be analysed further to justify the achievement of high Q-factor values. For instance, the Q-factor value for this particular device has been measured to be approximately 90,000 using a different characterization set-up [48]. Therefore, several in-house fabrication and linear characterization processes have also been carried out for these device structures using the same procedure as discussed in *Chapter 3*. The fabrication run were carried out using different wafer of similar layer structures to provide consistency. For simplicity, the device considered is shown in *Fig.4.17* with the $NT_0=3$, $NT_I=4$, N=5. The results of *Fig.4.20* show a great improvement in the Q-factor value of approximately 147,000, with reasonable optical transmission, as compared to previous results [48]. We have also achieved approximately the same Q-factor values for several different fabrication runs, as shown in *Fig.4.20 [i]*.
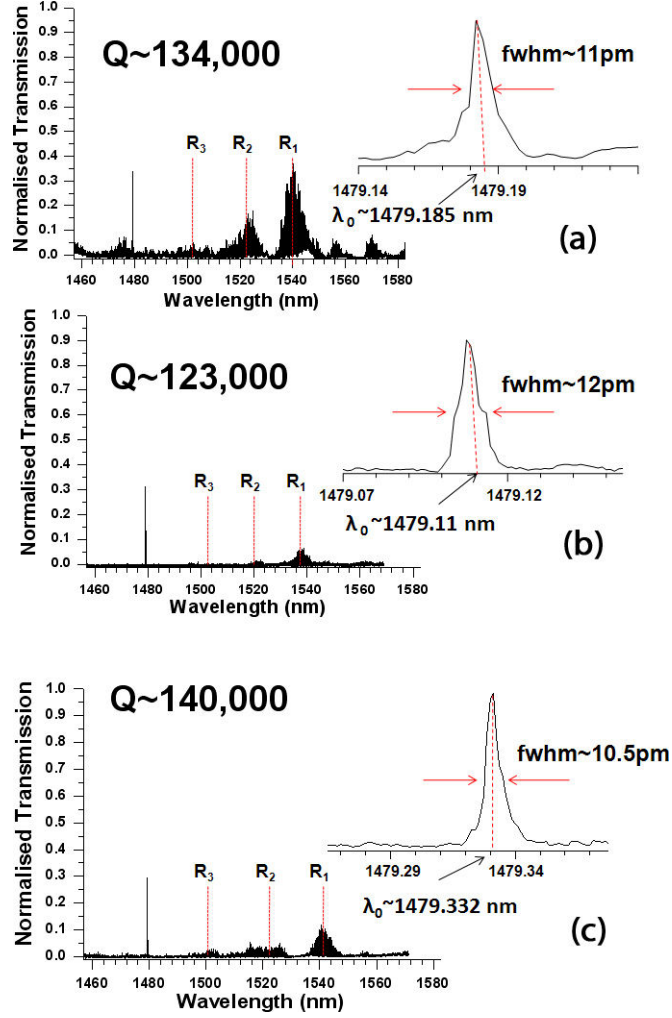
**Fig.4.20 [i]**. *Measured transmission spectra for N = 5 with $N_{TI}$ = 4 and $N_{TO}$= 3 using different fabrication runs within 6 months periods in comparison with the results obtained in Fig.4.20 carried out on April January 2008 (a) March 2008 (b) May 2008 (c) July 2008*

The ultra Q-factor values obtained were within the range 120,000 to 150,000, based on the different fabrication and characterisation runs carried within the stipulated time periods. These devices were characterised further, as reported in [49] - with Q-values of approximately 90,000 for the same device structures being obtained using different experimental set-ups. Based on a Fabry Perot model [50, 51], the Q-factor associated with the cavity formed by two identical mirrors with reflectivity, R, is given by:

$$Q = \frac{\pi}{1-R}\left[\frac{2Ln_g}{\lambda_0} - \frac{\lambda_0}{\pi}\left(\frac{\partial\phi}{\partial\lambda}\right)_{\lambda_0}\right] \qquad (4.1)$$

where $n_g$ is the group index of the ridge guide mode and L is the defect cavity length between the two smallest holes in the micro-cavity region. By introducing the penetration length into the distributed mirrors (equation 4.2):

$$L_p = -\lambda_0{}^2 \left[ \left(4\pi n_g\right)\left(\frac{\partial \phi}{\partial \lambda}\right)_{\lambda_0} \right] \qquad (4.2)$$

equation 4.1 can be re-written as:

$$Q = \frac{k_0}{1-R} n_g \left(L + 2L_p\right) \qquad (4.3)$$

where $L_{eff} = L + 2L_p$ is the effective cavity length. Detailed description and analysis of equation 4.1 to 4.3 can be found in reference 50. By using this equation, the measured reflectivity of this particular device is given as approximately 0.9998. This record reflectivity, R was achieved with a device having the small footprint of approximately 10 μm x 0.5 μm. With this R value, one should expect that the optical transmission is almost null or zero at other frequencies than the resonance wavelength. But in the measured results shown in *Fig.4.20 and 4.20 (i)*, resonance-'like' features were observed at wavelengths between 1520 nm and 1555 nm, which may be due to Fabry-Perot effects produced by the end-cleaved facets.

Based on the Eq. 4.4, for the peak spacing of multiple FP resonances seen in *Fig.4.20 [i]* which will be referred to as resonances $R_1$, $R_2$ and $R_3$, the cavity length for a particular uniform resonance spacing is given by [52, 53] - giving the famous equation used in analysis of FP effects in laser cavities ;

$$L = \frac{\lambda_0{}^2}{2 \, \delta\lambda \, n_g} \qquad (4.4)$$

*Where:*

        *L*        *- Cavity Length of the FP effect associated with multiple resonances*

        *λ*        *- Central wavelength of the associated resonances*

        *δλ*      *- Distance between two adjacent resonance peaks*

        *$n_g$*      *- Group refractive index (note: in this case the $N_g = N_{si} = 3.45$- this is based on the assumption of $N_g$ is big enough which approximately equal to actual $N_{si}$ – no further attempt is made at this stage to calculate the actual $N_g$)*

*Where $n_{eff}$ is given by;*

$$n_g = n_{eff} - \lambda \frac{dn_{eff}}{d\lambda_0}$$

By fitting the value of the observed resonance spacing between $R_1$ and $R_2$ in each case *(referring to Fig.4.20 [i]- (a to c) )* of approximately 22 nm, 17 nm and 24 nm into equation 4.4, the cavity lengths that correspond to this spacing are calculated to be approximately 15 µm, 19 µm and 16 µm respectively. The resonance-like features that are associated with this particular cavity length, based on Equation 4.4 above, are somewhat peculiar, since it is rather difficult to establish the origins of these features. One possibility might be due to the existence of the lateral stitching errors discussed in *Chapter 3 (see section 3.3.3)* that occur during the patterning process when using EBL. But the FDTD simulation approach used for these particular device structures as obtained in *Fig. 4.18* does not show this feature within the stipulated stop band since it does not include the sample ends in the structure that is modelled. Therefore no FP effects are expected in the simulations results. Further tests to model this structure using the FDTD approach for several different lengths ranging from 5 to 30 µm still show results similar to those obtained in *Fig.4.18*. Therefore the existence of the resonance-like features (by referring to $R_1$, $R_2$ and $R_3$ in *Fig.4.20 [i] (a to c)* may be due to the fabrication uncertainties.
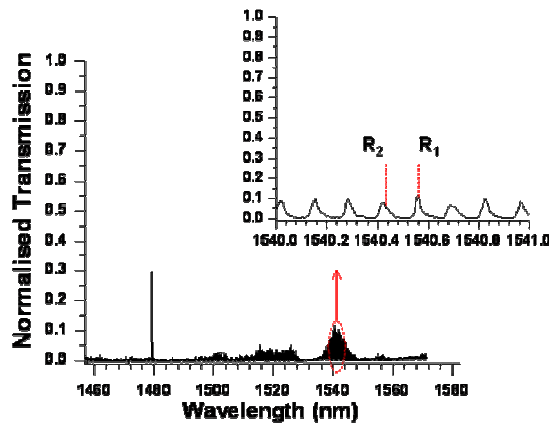


**Fig.4.20 [ii]**. *One example (close up view) showing fine features associated with the FP effect due to the end cleaved facet.*

Furthermore, based on the *Fig.4.20 (ii)*, when looking closely (zoom view) on the fine features within the system and using equation 4.4, these features that associated to the FP multiple resonance seen in *Fig.4.20 (ii)* which referred to as Resonance $R_1$ and $R_2$,

the cavity length, L for a particular uniform resonance spacing is calculated to be approximately 2.5 μm which matched the actual sample length.

## 4.6        Suspended wire SOI PhC/PhW Micro-cavities

The high-Q optical micro-cavities that confines light in small volume, V at optical wavelength scales are significantly importance for telecoms applications such as signal processing, slow light and modulators. Several High Q values have been reported for different designs consideration but requirement for achieving high Q value together with large optical transmission in small modal volume is increasingly importance. As previously discussed within this chapter, high Q-factor values have successfully been obtained. But for this kind of structures, most of the designs are based on the silicon waveguides sitting on a silica buffer layer. Although high optical confinement within the silicon photonic wire is desirable, the situation has not been optimized, since there is a large difference between the refractive index of the upper cladding (air) and the silica cladding underneath the silicon core - producing a vertically non-symmetrical type structure - and, reducing the optical confinement within the core waveguide. This reduced confinement is due to the fact that the evanescent field of the mode lies un-evenly between the upper and lower cladding. Therefore providing a symmetrical core waveguide with exterior identical media, with same refractive index, is required. Many attempts have been made to fabricate and measure the optical properties for different photonic crystal structures suspended in the air [43, 45-46], but there is still many issues surrounding its mechanical stability and fabrication complexity. Although in some cases, the air-bridge type of structures has also known to reduce propagation losses. The motivations towards designing membrane PhC/PhC waveguides are to increase optical confinement within the wire waveguides as well as to reduce the propagation losses that this structure can provide. In this presentation we will present our recent results on our design for high-Q photonic crystal/photonic wire waveguides suspended in the air- creating air bridge structures.

## 4.6.1        Design Considerations and 2D FDTD approach

Planar one dimensional photonic crystal micro-cavities embedded in 500 nm photonic wire waveguides have been realized recently with high Q-value of approximately

18 500 and large normalized transmission of nearly 85% - *see section 4.4.2*. This value achieved with silicon guiding layer sitting on a silica buffer layer. The details descriptions of this design can be found in that section. *Fig.4.21* shows SEM image of this particular device with silica cladding underneath it removed- creating air bridge type of structures *(See inset Fig.4.21)*. The silica layer removed from underneath the silicon core was measured to be approximately 1 μm as specified by the manufacturer of the sample - SOITEC, which provide enough optical isolation within the core waveguide.
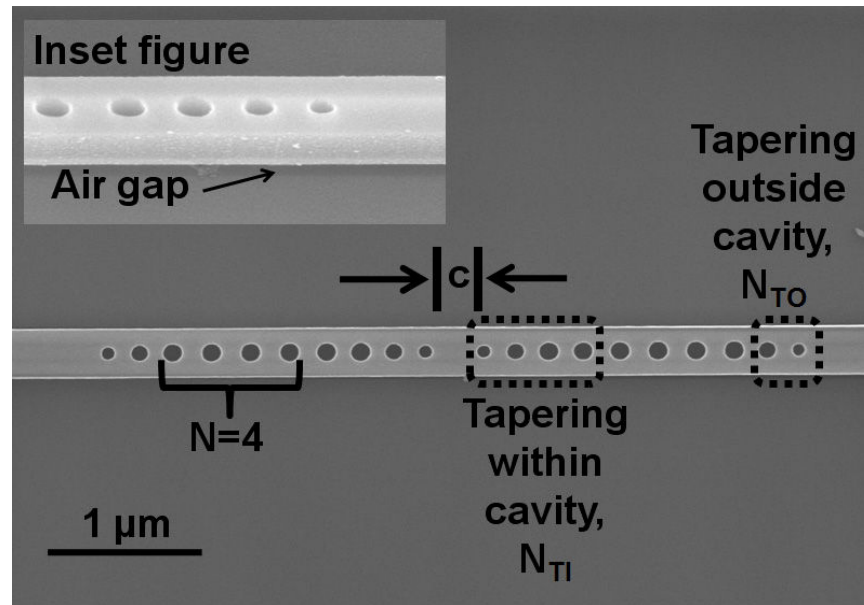


**Fig.4.21**: *SEM image of an air bridge type of a tapered single row PhW/PhW waveguides with cavity length, c, four hole tapered within cavity, $N_{TI}$ and two hole tapered outside cavity, $N_{TO}$. Inset is the bird's eye view (angle ~ 25°) of the suspended PhC/PhW micro-cavities.*

For comparison purposes, the design used for the suspended wire is the same as previously used in *section 4.4.2 (see Fig.4.12)*. It consists of a four periodic hole mirror separated by a micro-cavities spacer between them. Four and two aperiodic hole tapers were inserted within cavity and outside cavity to reduce modal mismatch between an un-patterned wire and the periodic hole section. 3D FDTD simulations have been carried on one of the device structures similar to our devices in *section 4.4.2* - but with the silica buffer layer having removed. This device has a periodic mirror, N= 4 with hole diameters of 182 nm and periodic spacing between

hole of 350 nm. The tapered within cavity and outside cavity have four and two aperiodically placed hole respectively.
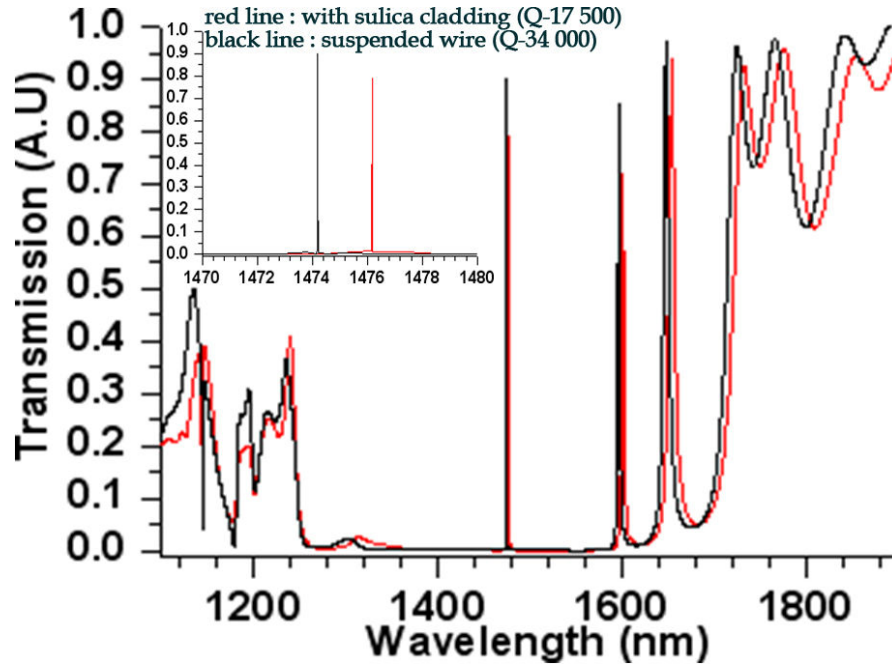


**Fig.4.22***: 3D FDTD computed for the tapered one dimensional PhC micro-cavities embedded in 500 nm wire waveguides with cavity length, c ~ 390 nm for suspended wire (black line) and without removing silica buffer layer cladding (red line).*

*Fig.4.22* shows a comparison of the tapered photonic crystal micro-cavities embedded in 500 nm photonic wire waveguides simulated using 3D Finite difference time domain (FDTD) approach for suspended wires and the one with silica buffer layer. The simulated result using 2D FDTD approach shows further enhancement in the Q-factor value from 17 500 to 34 000 for the suspended wire in comparison with the one of silica buffer layer still exists underneath the silicon guiding layers. The shifts of the resonance by approximately 3 nm were also measured toward shorter wavelength for this design arrangement with the increased in optical transmission by almost 10%. The shift in particular is due to the reduction in the effective refractive index of the silicon- thus shifting the resonance towards longer wavelength as the silica layer removed.

### 4.6.2          Experimental results and Discussions

The devices were fabricated using direct-write Vistec VB6 electron beam lithography and dry etching technology. They were characterized using tunable laser covering the range from 1457 nm to 1580 nm. The TE polarized was end-fire coupled into and out of the waveguides and was detected using germanium photo-detector.
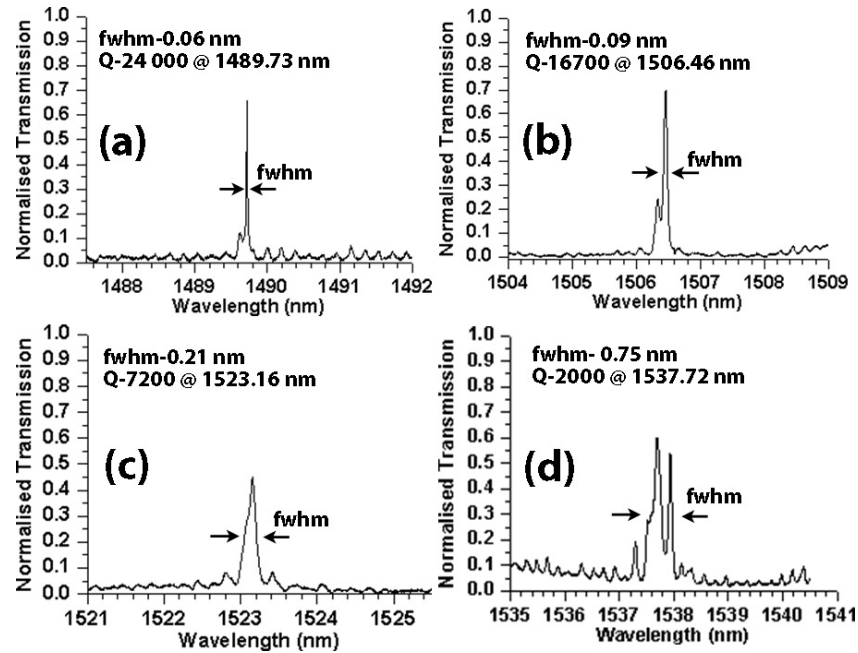


**Fig.4.23**: *Measurement result for suspended PhC/PhW micro-cavities in a suspended wires with $N_{TI}=4$ and $N_{TO}=2$ and cavity lengths, c (a) 390 nm (b) 415 nm (c) 440 nm (d) 465 nm*

An experimental results corresponding to the simulation result obtained using 3D FDTD approach used in *Fig.4.22* are shown in *Fig.4.23*.The optimum Q-value of approximately 24 000 have been obtained at the cavity length, c of 390 nm – with normalized transmission of 65%. A uniform shift of approximately 16.7 nm towards longer wavelength is also obtained for a 25 nm increased in the cavity length, which has shown greater flexibility for the tuning capability of the device. The Q-value dropped rapidly as the optical transmission also dropped by approximately 25%. Therefore, by using a correct choice of cavity length, together with the use of optimised hole diameters and tapered hole parameters, high-Q value and large transmission are observed.

In other word, as a cavity length increased from 390 nm to 465 nm, the Q-value has reduced from 24 000 to 2000 together with the reduction in the normalized optical transmission. *Table 4.2* shows a comparison of the structures shown in *Fig.4.21* with our previous results – without removing the silica buffer layer (*section 4.2.2- see Fig 4.12*). *Table 4.2* shows a significant improvement in the Q-factor value, although a slight drop in the normalised optical transmission is also observed for the case of cavity length, c=390 nm. The experimental results – shows that the reduction in Q-value from 18,500 to approximately 24,000 with the suspended wire type of structures at the cavity length of 390 nm – but this value is not as high as we initially expected due to other issues relating to our design arrangement and the need of optimizing our fabrication processes. Somewhat surprisingly, at longer cavity lengths (440 and 465 nm), the Q-value obtained is much lower for the suspended wire, which shows that the Q-value drop more rapidly for this case as compared to the non-suspended wire.

| Cavity length, c/(nm) | With silica buffer cladding | | Suspended wire waveguides | |
|---|---|---|---|---|
| | $Q$ | *Normalized Transmission* | $Q$ | *Normalized Transmission* |
| 390 | 18 500 | 0.85 | 24 000 | 0.67 |
| 415 | 16 600 | 0.82 | 16 700 | 0.71 |
| 440 | 9 000 | 0.71 | 7 200 | 0.45 |
| 465 | 5 900 | 0.83 | 2 000 | 0.58 |

**Table 4.2***: Comparison of the measured results for the suspended wire waveguides and the one with silica cladding still exist underneath the wire waveguides.*

At some point the Q-value dropped from 9,000 to 7,200 for c=440 nm and 5,900 to 2,000 for c=465 nm. Based on this result, it has been shown that it looks plausible that Q-factor values as high as 500,000 can be achieved with the correct combination of the number of periodic mirrors, cavity length and aperiodic hole tapered within and outside cavity for this kind of structure. The enhancement in the Q-value in this particular design- is due to the increase in the optical confinement – thus enhancing

the field intensity of the mode confined within the small micro-cavities. On the other hand, the effective refractive index changes due to the air gap underneath the silicon guiding layer have also shown a shift in the resonance frequency by approximately 3 nm. In this case, 3D FDTD approach used to simulate those devices has shown sufficiently good agreement with the measured results.

## 4.7        Summary

This chapter in particular has placed an emphasize on the design of tapered holes, where a correct choice of hole parameters was used for both tapering outside and within the cavity, in order to achieve ultra high Q-factor values together with useful optical transmission. The initial designs using both tapering arrangements- which were designed separately - showed that tapering can enhance either the optical transmission or the quality factor value. With the correct choice of tapered hole structure, the Q-value and optical transmission have been significantly increased. Four hole tapers within the cavity have been used for Q-factor enhancement whereas variable number of holes in the tapers outside the cavity has been used to enhance the optical transmission. Initially, one hole tapers have been used with Q-factor values of approximately 16,000 – and with normalised transmission of 60% - were achieved experimentally. But this value was further increased to approximately 18,900, with nearly 85% normalised transmission. By adding the number of restricted mirrors to five (5) and three (3) hole tapers outside the cavity, the Q-value has been increased to approximately 147,000, together with normalised transmission of 35%.

In one example, removing the silica cladding underneath the silicon waveguide has also shown an improvement in the Q-factor value by almost 25%, which is particularly due to the increase in the optical confinement within the silicon waveguide – as provided by the symmetrical vertical design of the silicon with air as both the  upper and lower cladding.

**References:**

1. Ahmad RU, Pizzuto F, Camarda GS, Espinola RL, Rao H, and Osgood RM, 'Ultra compact corner-mirrors and T branches in silicon-on- insulator', *IEEE Photonics Technology Letters*, vol. 14, no. 1, January, 2002.

2. F.Ohno, T. Fukuzawa and T. Baba," Mach–Zehnder Interferometers Composed of μ-Bends and μ-Branches in a Si Photonic Wire Waveguide", *Japanese Journal of Applied Physics* , Vol. 44, No. 7A, 2005, pp. 5322–5323.

3. Richard De La Rue, Harold Chong, Marco Gnan, Nigel Johnson, Iraklis Ntakis, Pierre Pottier, Marc Sorel, Ahmad Md Zain, Hua Zhang, Edilson Camargo, Chongjun Jin, Mario Armenise and Caterina Ciminell 'Photonic crystal and photonic wire nano-photonics based on silicon-on-insulator', *New Journal of Physics*, **8**, (2006) 256.

4. E. A. Camargo, H. M. H. Chong, and R. M. De La Rue, 'Highly compact asymmetric Mach-Zehnder device based on channel guides in a two-dimensional photonic crystal', *Appl. Opt.,* **45**, pp. 6507-6510, 1$^{st}$ Sept (2006).

5. E.A. Camargo, H.M.H. Chong and R.M. De La Rue, 'Four-port coupled channel-guide device based on 2D photonic crystal structure', *Photonics and Nanostructures - Fundamentals and Applications*, 2(3), $^{pp}$. 207-213, December (2004).

6. Hua Zhang, M. Gnan, N.P. Johnson and R.M. De La Rue, 'Ultra-Small Mach-Zehnder Interferometer Devices in Thin Silicon-on-Insulator', *Integrated Photonics Research and Applications (IPRA),* Uncasvil$^{le}$, Conn., USA, April (2006).

7. H. M. H. Chong and R. M. De La Rue, "Tuning of photonic crystal waveguide microcavity by thermooptic effect," *IEEE Photon. Technol. Lett., vol. 16, no. 6, pp. 1528–1530, Ju*n. 2004.

8. M. W. Geis, S. J. Spector, R. C. Williamson, and T. M. Lyszczarz, "Submicrosecond submilliwatt silicon-on-insulator thermooptic switch," *IEEE Photon. Technol. Lett.*, vol. 16, no. 11, pp. 2514–2516, Nov. 2003.

9. T. F. Krauss and R. M. De La Rue, "Photonic crystals in the optical regime—Past, present and future," *Progress Quantum Electron.*, vol.23, no. 2, pp. 51–96, Mar. 1999.

10. M. Gnan, S. Thoms, D.S. Macintyre, R.M. De La Rue and M. Sorel, 'Fabrication of low-loss photonic wires in silicon-on-insulator using hydrogen silsesquioxane electron-beam resist', *Electronics Letters*, 44(2), 115 - 116, 17$^{th}$ Jan (2008).

11. M.Gnan, D.S. Macintyre, M.Sorel, R.M. De La Rue, and S.Thoms, "Enhanced stitching for the fabrication of photonic structures by electron beam lithography", *J. Vac. Sci. Technol. B*, 2007, 25, p . 2034

12. J. S. Foresi, P. R. Villeneuve, J. Ferrera, E. R. Thoen, G. Steinmeyer, S. Fan, J. D. Joannopoulos, L. C. Kimerling, Henry I. Smith & E. P. Ippen, "Photonic-bandgap microcavities in optical waveguides," *Nature* **390**, 143 (1997)

13. P. Lalanne and J. P. Hugonin, "Bloch-wave engineering for high-Q, small-V microcavities," *IEEE J. Quantum Electron.*, vol. 39, no. 11, pp. 1430–1438, Nov. 2003.

14. C. Sauvan, G. Lecamp, P. Lalanne, and J. P. Hugonin, "Modal reflectivity enhancement by geometry tuning in photonic crystal micro-cavities," *Opt. Express*, vol. 3, no. 1, pp. 245–255, Jan. 2005.

15. T.Asano, B.S.Song, S.Noda," Analysis of the experimental *Q* factors (~1 million) of photonic crystal nanocavities", *Optics Express*, **14**, 1996-2002 (2006)

16. P. Velha, E. Picard, T. Charvolin, E. Hadji, J. C. Rodier, P. Lalanne and D. Peyrade, 'Ultra-High Q/V Fabry-Perot microcavity on SOI substrate', *Optics Express*, **15** (24), 16090-16096, 26th November (2007).

17. Ahmad Rifqi Md Zain, Marco Gnan, Harold M. H. Chong, Marc Sorel and Richard M. De La Rue, "Tapered Photonic Crystal Microcavities Embedded in Photonic Wire Waveguides With Large Resonance Quality-Factor and High Transmission', *IEEE Photonics.Technology Letts*, **20** (1), 6 − 8, 1st January (2008).

18. S.Noda, M.Imada, M.Okano, S.Ogawa, M.Mochizuki, and A.Chutinan, 'Semiconductor 3D and 2D photonic crystals and devices', *IEEE Journal of Quantum Electronics*, vol. 38, no. 7, pp. 726-735, July 2002.

19. W.Bogaerts, D.Taillaert, B.Luyssaert, P.Dumon, J.Van Campenhout, P.Bienstman, D.Van Thourhout, R.Baets, V. Wiaux, and S.Beckx, 'Basic structures for photonic integrated circuits in silicon- on-insulator', *Optics*

*Express*, Vol. 12, No:8, pp.1583-1591, April 2004.

20. C. Angulo Barrios, V. R. Almeida, R. Panepucci, and M. Lipson," Electrooptic Modulation of Silicon-on-Insulator Submicrometer-Size Waveguide Devices ", *Journal of Lightwave Technology*, vol. 21, no. 10, pp. 2332-2339, October 2003.

21. C.A.Barrios, V.R.Almeida, and M.Lipson," Low-Power-Consumption Short-Length and High-Modulation-Depth Silicon Electrooptic Modulator," *Journal of Lightwave Technology*, Vol:21, No:4, pp. 1089-1098, April 2003.

22. AS Jugessur, R.M.De La Rue, P.Pottier,' One dimensional periodic photonic crystal microcavity filters with transition mode matching features embedded in ridge waveguide", *Electronics Letters*, Vol:39, No:4, pp. 367-369, February 2003.

23. M.Palamaru and Ph.Lalanne,"Photonic crystal wavaguides: Out of plane losses and adiabatic modal conversion", *Applied Physics Letters*, Vol. 78, No. 11, pp. 1466-1468, March 2001.

24. D.Peyrade, E.Silberstein, Ph Lalanne, A.Talneau and Y.Chen,"Short Bragg mirrors with adiabatic modal conversion", *Applied Physics Letters*, Vol. 81, No. 5, pp. 829-831, July 2002.

25. M. Notomi, K. Yamada, A. Shinya, J. Takahashi, C. Takahashi, and I. Yokohama," Extremely Large Group-Velocity Dispersion of Line-Defect Waveguides in Photonic Crystal Slabs", *Physical Review Letters*, Vol:87, No:25, pp. 1-4, December 2001.

26. Q.Xu and M.Lipson," All-optical logic based on silicon micro-ring resonators", *Optics Express*, vol. 15, no. 3, pp 924-929, February 2007.

27. Y.Akahane, T.Asano, B.S.Song, and S.Noda," Fine-tuned high-$Q$ photonic-crystal nanocavity", *Optics Express*, Vol:13, No:4, pp. 1202-1214, February 2003.

28. P.Velha, J.C.Rodier, P.Lalanne, J.P.Hugonin, D.Peyrade, E.Picard, T Charvolin, E.Hadji," Ultra high reflectivity photonic band-gap mirrors in a ridge SOI waveguide", *New Journal of Physics* (IOP), vol. 8, no. 204, pp 1-13, September 2006.

29. S.Combrié, E.Weidner, A.DeRossi, S.Bansropun, S.Cassette, A.Talneau and H Benisty, "Detailed analysis by FP method of slab photonic crystal line-defect

waveguides and cavities in aluminium-free material system", *Optics Express*, vol. 14, no. 16, pp. 7353-7361, August 2006.

30. W.Liang, L.Yang, J.K.S. Poon, Y. Huang, K.J.Vahala, and A.Yariv," Transmission characteristics of a FP etalon–microtoroid resonator coupled system", *Optic Letters*, Vol. 31, No. 4, pp. 510-512, February 2006.

31. Lalanne and A. Talneau: "Modal conversion with artificial materials for photonic-crystal waveguides", *Optics Express*, vol. 10, no. 354, 2002.

32. A. Talneau, Ph. Lalanne, M. Agio and C.M. Soukoulis: "Low-reflection photonic-crystal taper for efficient coupling between guide sections of arbitrary widths", *Optics Letters*, vol. 27, 1522-1524, 2002.

33. T.D. Happ, M. Kamp and A. Forchel: "Photonic crystal tapers for ultracompact mode conversion", *Optics Letters*, vol. 26, 1102-1104, 2001.

34. P. Sanchis, J. Martí, J. Blasco, A. Martínez and A. García: "Mode matching technique for highly efficient coupling between dielectric waveguides and planar photonic crystal circuits", *Optics Express*, vol. 10, pp. 1391-1397, 2002.

35. T.Baba and D.Mori,"Slow light engineering in Photonic crystals", *J. Phys. D: Appl. Phys.* **40** (2007) 2659–2665.

36. A.Figotin and I.Vitebskiy,"Slow light in Photonic Crystals", *Waves in Random and Complex Media* Vol. 16, No. 3, August 2006, 293–382

37. T.F.Kraus,"Slow Light in Photonic Crystal Waveguides", *J. Phys. D: Appl. Phys.* **40** (2007) 2666–2670

38. C.Monat, B.Corcoran, M.Ebnali-Heidari, C.Grillet, B.J. Eggleton,T.P. White, L.O'Faolain and T.F. Krauss," Slow light enhancement of nonlinear effects in silicon engineered photonic crystal waveguides", *Optics Express*, 17 (4), 2944-2953, 16th February 2009.

39. A.Samarelli, A.R.Md Zain, M.Gnan, H.Chong, M.Sorel, R.M.De La Rue, P.Frascella, C.Ciminelli and A.Armenise,"Single Row SOI-based Photonic Crystal/Photonic Wire Micro-cavities with Medium Q-factor and High Transmission", Integrated Photonics and Nanophotonics Research and Applications IPNRA 2007, OSA Technical Digest, paper IWD5, Salt Lake City, 8th July 2007.

40. D. K. Armani, T. J. Kippenberg, S. M.Spillane, K. J. Vahala , "Ultra-high-Q toroid microcavity on a chip" ,*Nature*, 421, 2003.

41. M. Soltani, S. Yegnanarayanan and A. Adibi, "Ultra-high Q planar silicon microdisk resonators for chip-scale silicon photonics", *Optics Express*, **15**(8) 2007.

42. T. Tanabe, M. Notomi, E. Kuramochi, "Measurement of ultra-high-Q photonic crystal nanocavity using single-sideband frequency modulator" , **43(3),** 2007,

43. T. Tanabe, M. Notomi, E. Kuramochi, A. Shinya, H. Taniyama, "Trapping and delaying photons for one nanosecond in an ultrasmall high-Q photonic-crystal nanocavity", *Nature Photonics*, **1,** 2007.

44. P.Lalanne, C.Sauvan and J.P.Hugonin ,"Photon confinement in photonic crystal nano-cavities", *Laser and Photonic Review*, 1-13, September 2008.

45. L.O.Faolain, X.Yuan, D.Mcintyre, S.Thoms, H.M.H.Chong, R.M. De La Rue and T.F.Krauss,"Low loss propagation in photonic crystal waveguides", *Electronics Letters*, 42 (25), December (2006).

46. S. Noda, M. Fujita and T. Asano, "Spontaneous-emission control by photonic crystals and nanocavities" *Nature Photonics,* **1**, 449 (2007)

47. M.Gnan, G.Bellanca, H.M.H.Chong, P.Bassi and R.M.De La Rue," Modeling of Photonic Wire Bragg Gratings", *Optical and Quantum Electronics*, 38, pp.133-148, January 2006.

48. A.R. Md Zain, M. Gnan, H. Chong, M. Sorel, and R.M. De La Rue, " Tapered Photonic Crystal Micro-cavities Embedded in Photonic Wire Waveguides with Large Resonance Q-factor and High Transmission", IEEE Photon. Technology Letters 20, 6 January (2008).

49. M. Belotti, M. Galli, D. Gerace and L.C. Andreani, A. R. Md Zain, N. P. Johnson, M. Sorel and R. M. De La Rue,"All-optical Switching in Silicon-on-Insulator Photonic Wire Nano-cavities", IEEE/LEOS Winter topical meetings, Inssbruck, Austria, p.p 30-31, 12-14 January 2009.

50. Sauvan C, Lalanne P and Hugonin J P," Slow-wave effect and mode-profile matching in photonic crystal micro-cavities" *Phys. Rev.* B, **71** 165118, 2005

51. P.Lalanne, C.Sauvan and J.P Hugonin," Photon Confinement in photonic crystal nano-cavities", Laser an Photonic Review, Wiley Inter-Science, 1-13 (2008)

52. Optical waves in layered media, P. Yeh, LIVRE, J. WILEY EDITIONS, 1988

53. Waves and Fields in Optoelectronics, Herman.A.Haus, Prentice Hall, in Solid State Physical Electronics, 1984.

# CHAPTER 5:

# Photonic Crystal (PhC) / Photonic Wire Extended Cavities and Coupled Micro-cavities

This Chapter will place its emphasize on the design of an extended Fabry-Perot (FP) cavity spacer and coupled micro-cavity combination, with two micro-cavities embedded so as to split two sets of mirrors. One of the main aims of the work described was to provide the basic building block for designing a possible temperature dependent filter, in which the spacer section between two cavities is capable of providing tuning capability - without the needs of heating the silicon waveguide. This design is possibly applicable for telecoms applications such as wavelength division multiplexing (WDM). The freedom to choose a wavelength of interest is an important requirement. In addition, coupled cavities will provide a basic building block for designing more complex multiple cavity structures, where three or more micro-cavities are embedded between periodic mirrors. Two or more resonances excited within the stop band can be selected at any particular wavelength of interest. For the extended cavity condition, tapering within and outside cavities is used to enhance the Q-factor together with obtaining greater optical transmission - whereas tapering in the coupled micro-cavities design arrangement is used to increase the coupling strength of the device.

## 5.1        Introduction

PhCs are periodic structures that are known to be capable of controlling the propagation of light through a medium [1-3]. Thus PhCs have become a promising

platform for realising Photonic Integrated Circuits (PIC) components, reducing the size and power requirements of the optical components. Among several applications such as Wavelength Division Multiplexing (WDM), micro-cavity laser and LED's [4-7], one of the capabilities that PhC devices can provide is selective management of several wavelengths – hence making them potentially useful for telecommunications applications such as WDM and add-drop filtering. One of the challenges for PhC researchers is to develop structures that can minimise the losses due to the modal mismatch that occurs as light travels from un-patterned waveguides into PhC regions. To take into account the finite lateral size of the structure, several simulations have been carried out by using the2D FDTD method. This technique has been used to calculate the transmission and reflection spectra of single reflector and whole filter structures, both in free space and in finite width waveguide structures. In this way, the number of rows in each periodic reflector and the size of the reflector in the transverse direction have been optimised. To obtain a high level of accuracy, a very small discretization step is required and a very large number of time steps have to be calculated, requiring a long CPU time and large memory occupancy. Although 2-Dimensional PhC device are commonly used for applications such as beam-splitters, couplers, lenses and power dividers [8-12], 1D PhC/PhW devices can provide extra freedom in the design of more complex devices with smaller size and higher Q-factor – approaching 150,000 as demonstrated in *Chapter Four*. This Q-value have been achieved through the micro-cavity design arrangement, with a cavity length of around 400 to 500 nm. But designing devices with a longer spacer – such as an extended cavity and multiple micro-cavities – is desirable for having extra freedom to choose a resonance at a wavelength of interest through the multiple resonances excited within the stop-band. This performance can be achieved through the use of 1D PhC/PhW extended cavity structures where the micro-cavities that have been described in the previous chapter are further extended by several micrometres in cavity length – covering, in this work, the range from 2 μm to 9 μm. Multiple resonances were excited within the band-gap. These multiple resonances can be controlled through variation of the parameters such as the cavity length and hole dimensions. This design has considerable potential for practical applications such as wavelength division multiplexing (WDM) in telecom applications. A waveguide with a Fabry-Perot (FP) cavity formed by a several micrometres long spacer section

between two mirrors has been realised based on 2D photonic crystal structures [13-14]. By using the several different cavity spacer lengths investigated in this Chapter, one of several longitudinal (axial) modes of the cavity can be selected to match the operating wavelength required, i.e. to fall within the range of 1520 nm to 1580 nm required for typical WDM applications, switching purposes and non-linear optics. The large free spectral range (FSR) between the resonances excited means that such structures have the capability of tuning the resonances through thermo-optical effects where, for example, heating the silicon waveguide to approximately 300°C should be sufficient to scan the resonance across the whole wavelength available within that range. In addition, through the use of the correct choice of tapering both within and outside cavity, it can be expected that enhancement the Q-factor value – together with obtaining large optical transmission – will be possible, implying that viable scanning channel-drop filter devices could be produced.

On the other hand, the resonance excited by a short micro-cavity can also be manipulated by splitting the single resonance into two or more resonances by using coupled multiple cavity arrangements [15-16]. In addition, coupled micro-cavity structures can provide a useful platform for DWDM applications – where two or more micro-cavities can be coupled together and used to split the single-cavity resonance into a number of resonances that depends directly on the number of micro-cavities used. This type of device is also potentially useful for filter function synthesis in telecommunication applications, sensing, non-linear optical functionality and in obtaining slow-light propagation [16-19, 22]. Such structures consist of two or more cavities coupled through periodically spaced hole mirrors. The multiple coupled-cavity combinations produced split the selected single cavity resonance frequency into a number of resonances that depends on the number of cavities used in the design [18]. Tapering of the PhC hole structures within and outside photonic crystal/photonic wire micro-cavities has also been shown to yield a substantial improvement in the quality factor and optical transmission at the resonance frequencies. For applications that require a filter response with a nearly level pass-band and steeper skirts at the edges of the pass-band, the coupling strength between cavities must be carefully controlled – and additional cavities may be required to optimize the response [20, 29].

## 5.2        Device Descriptions for PhC/PhW Extended Cavities

In this present work, the extended cavity structures proposed have cavity lengths ranging from 2 μm to 9 μm. In order to obtain the high performance required, the appropriate choices of cavity length, hole diameter and periodic or aperiodic spacing between holes are required. On the other hand, the use of tapering within and outside the cavity, as discussed in *Chapter Four (see section 4.3)*, still plays an important role. At a particular extended cavity length, a combination of parameters with appropriate hole transition sections for light either entering or leaving the periodic sections, high transmission and high Q-values of the resonances can be obtained. In this *Chapter*, extended cavities will be described that have spacer sections with spacer lengths in the range from 2 μm to 9 μm and photonic crystal mirrors consisting of 4 periods of holes with diameters, *d*, of 182 nm and periodicity, *a*, of 350 nm. The photonic crystal mirrors are embedded in the 500 nm wide silicon photonic wire core. *In Fig.5.1.*, two sections, each using four aperiodically-located and tapering holes within the cavity, have been used, with hole diameters of 170 nm, 180 nm, 166 nm and 131 nm – and centre-to-centre hole distances of 342 nm, 304 nm, 310 nm and 290 nm, respectively.
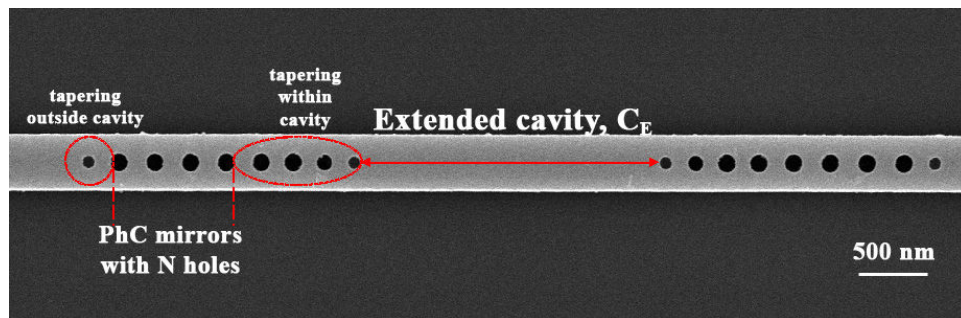


**Fig.5.1**: *SEM images of a single row PhC extended cavity with tapering effects both within and outside the cavity.*

This configuration has been used as a taper hole arrangement within the cavity, which has been shown to enhance the resonance quality factor – as discussed in *Chapter 4 (section 4.4)*. For instance, the number of aperiodically spaced holes used in the tapering outside cavity section is also a crucial parameter that determines the behavior of the transmission spectrum at resonance. The number of holes used in the aperiodic

taper sections may vary between one and four holes with different diameters, modifying the guided light distribution at the entrance to the periodic mirror sections. The device structure considered is shown in *Fig.5.1,* where cavity spacer section, $C_E$, was extended further, resulting in multiple reflections within the cavity region and producing multiple resonance effect. In this particular design, the same hole configuration as previously discussed in *Chapter 4* is used, where one-hole aperiodic tapered sections outside the cavity have an additional hole diameter of 130 nm, with centre-to-centre hole distances of 290 nm. This carefully chosen aperiodic hole arrangement has produced a significant impact on the Q-factor value and optical transmission. *Fig.5.1* also shows an SEM image of the device with tapered arrangements of aperiodic holes within and outside the cavity, with reasonably smooth sidewalls. Initially, a 2D Finite Difference Time Domain (FDTD) computation, together with an effective index approach was used to produce preliminary designs. A fully 3D FDTD approach was used subsequently, at high resolution, to simulate the device. This approach gives considerably more accurate predictions, but with much larger computational time and power requirements. The extensive memory requirement of several tens of gigabytes and time consumption are still a major concern when using the 3D-FDTD approach – and parallel or cluster computing is clearly very desirable. Comparisons of 2D and 3D computational results have been made where the spectral differences were analyzed further.

## 5.3      2D and/or 3D FDTD Approach

## 5.3.1      Short Extended Cavity Arrangement

For easier discussion and analysis, the extended cavities considered will be divided into three distinct configurations, namely the short extended cavity, the medium extended cavity and the long extended cavity. The short extended cavity has a spacer section that ranges from 2 μm to 4 μm, whereas the medium and long extended cavities range from 5 μm to 6.5 μm and 7 μm to 9 μm in length respectively. Starting with the short extended cavity design, 2D FDTD has been used to simulate the device structures over a wide range of wavelengths, covering the range from 0.5 μm to 3 μm. *Fig.5.2* shows the transmission spectra of the particular device shown in *Fig.5.1,* but with two hole tapered sections outside the cavity – with the wavelength spectrum

ranging from 1200 nm to 1700 nm. As expected, for a short extended cavity length, the number of resonances excited within the stop band very much dependent on the cavity length, as is shown when the cavity length is progressively increased from 2 µm to 3.5 µm in the 500 nm in steps as shown in *Fig.5.2*. (2D FDTD simulation results), the number of resonances excited increases from three to four; with approximately equal separation between the resonances in each case.
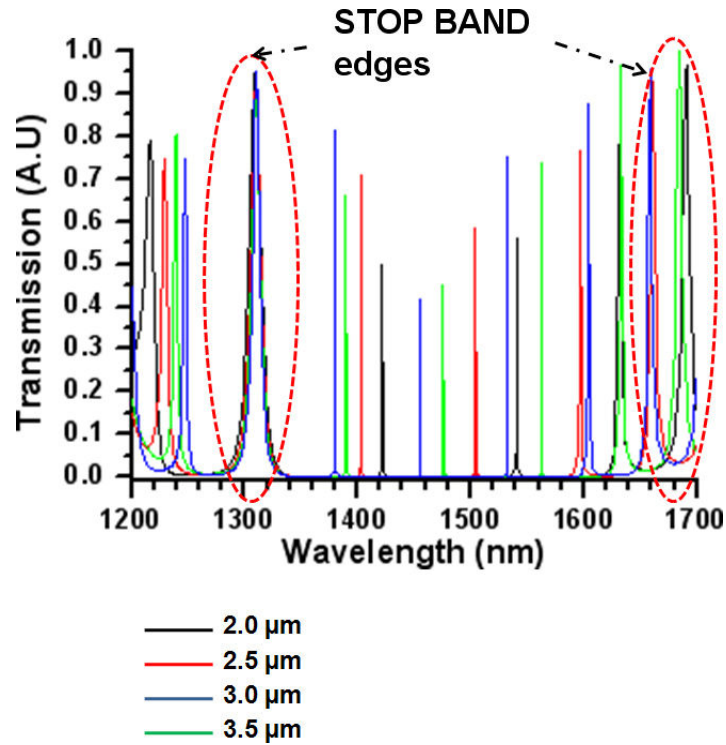


**Fig.5.2**: *The optical transmission spectra computed using 2D FDTD approach for short extended cavity ranging from 2 µm to 3.5 µm over wide wavelength/frequency range.*

The average free spectral range (FSR) value for the resonance decreases from approximately 120 nm to 101 nm, 86 nm and 75 nm with respect to the cavity length, $C_E$ of 2 µm, 2.5 µm, 3 µm and 3.5 µm shown in *Fig.5.2* and *Fig.5.3* (zoom-in). *Fig.5.3* shows a 'zoom-in' of the optical transmission spectra of the resonance falling within that limited range (related to the capabilities of the tunable laser used in this present work) for discussion and comparison with the experimental results in later section. It is also shown that, for each cavity resonance condition, the Q-factor calculated is highest for the resonance wavelength that falls within this range – which related to the capabilities of the tunable laser used in this present work as compared to

other neighboring resonances. The Q-values of 2200 (at $\lambda_0$-1540.79), 7500 (at $\lambda_0$ 1504.25 nm), 7200 (at $\lambda_0$-1455.05 nm) and 11,000 (at $\lambda_0$-1475.62 nm) were calculated using 2D FDTD approach respectively for cavity lengths of 2 μm, 2.5 μm, 3 μm and 3.5 μm.
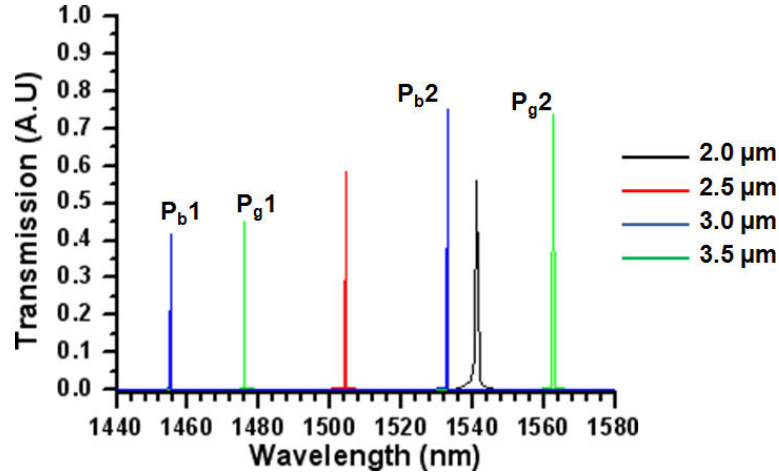


**Fig.5.3**: *A 'zoom-in' of the optical transmission spectra deduced from Fig.5.2 for comparison with measurement result in later section ($P_b$- resonance for blue line and $P_g$-resonance for green line)*

The optical transmission coefficients calculated at that resonance wavelength were 56.2%, 58.3%, 45.2% and 41.6% respectively for the same set of cavity spacer length. But due to the limitation on the characterization set-up used throughout the present work shown in *Chapter3* in which the tunable laser used had a limited range which ranging from 1457 nm to 1583 nm, the analysis and detailed discussion will only be restricted within or around that range for comparison with the measured results.

### 5.3.2        Medium Extended Cavity Arrangement

As the cavity length increases towards the medium extended cavity range (i.e. between 5 μm to 6.5 μm), the number of resonances excited within the stop band have increases, implying more FP reflectivity within the cavity, as shown in *Fig.5.4*. This behavior is partly due to the increase in the Fabry-Perot (reflectivity) excited within the longer spacer region as the cavity length increases – so that more resonances will be excited within that specific stop-band. For this type of device, a comparison will be made on the impact of incorporating tapering both within and outside the cavity.
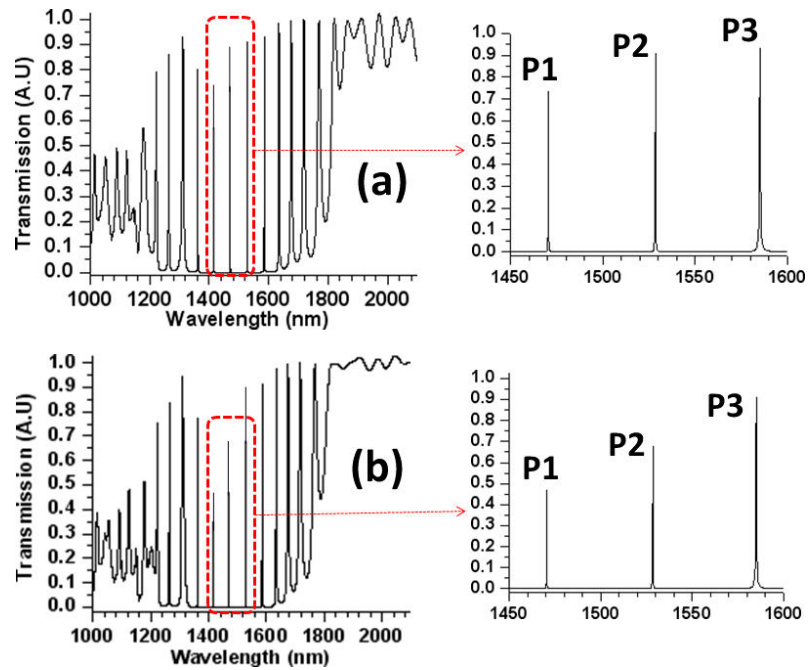
**Fig.5.4**: *2D FDTD simulation approach for 5 µm long extended cavity with tapering within the cavity and (a) with tapering outside the cavity (b) without tapering outside the cavity.*

*Fig. 5.4 (a)* shows the results of a 2D FDTD simulation of a 5 µm long extended cavity, with tapering used both within and outside the cavity – and using specifically two hole tapering outside the cavity, while *Fig. 5.4 (b)* shows the results for the cavity without the use of tapering effects outside the cavity.

**Table 5.1**: *A comparison of 2D FDTD approach showing the effect of tapering within and outside cavity in the Q-value and optical transmission for $C_E$=5 µm*

|  | Q-factor | Optical Transmission (%) |
|---|---|---|
|  | w/o \| both \| w/TI | w/o \| both \| w/TI |
| P1 | 800 \| 97,000 \| 51,000 | 35.1 \| 72.9 \| 46.3 |
| P2 | 760 \| 25,300 \| 8,600 | 38.3 \| 91.1 \| 67.5 |
| P3 | 320 \| 8,000 \| 3,900 | 43.8 \| 92.7 \| 90.5 |

*Note: w/o – without hole tapering, w/TI – with tapering within cavity, both – using both tapering within and outside cavity*

*Table 5.1* shows a comparison of the optical transmission and Q-factor values for the cases with and without tapering outside the cavity. As the tapering section was introduced into the design with a medium cavity length of 5 μm, the optical transmission increased by almost 20% - and the Q-value at the resonance frequency also increased to the value of 97,000 for P1, as shown in Table 1 – simulated using 2D FDTD approach. The transmission and Q-factor enhancements were attributed to the introduction of both tapering within and outside cavity for this kind of structure. On the other hand, in *Fig.5.4 (b)*, a resonance Q-factor of nearly 51,000 was calculated at the resonance wavelength of 1471 nm, using the 2D FDTD approach. As mentioned earlier, further enhancement of the transmission and Q-factor was achieved through the use of tapering outside the cavity – where a calculated Q-factor value of approximately 97,000 was obtained at a resonance wavelength of 1472 nm, as shown in *Fig.5.4 (a)* – for resonance P1. By referring to P1 in that figure, the optical transmission of the PhC micro-cavity using tapering both within and outside the cavity shows a significant increase, by almost 27%, together with approximately 50% increase in the Q-factor value. It shows an increase in the optical transmission and Q-factor value from 46.3% to 72.9% and 51,000 to 97,000 respectively. Tapering both within and outside the cavity has greatly enhanced both the optical transmission and Q-factor values.

## 5.3.3 Long Extended Cavity Arrangement

Simulation of a somewhat longer cavity, with spacer section lengths is further expended between 7 μm to 8 μm – and with the introduction of tapering within the cavity also shows multiple Fabry-Perot resonances, with the number of resonances excited increasing to seven – with medium Q-factor values and large transmission. Medium Q-factor values of between 5000 and 10,000 have been calculated using the 2D FDTD approach, as shown in *Fig.5.5*. The highest Q-factor values calculated were at resonance wavelengths ranging from 1480 nm to 1500 nm, with transmission values of less than 50% for all cases. A constant shift, by approximately 6 nm, in the whole set of resonances for each cavity length case towards a shorter wavelength was observed, as the cavity length increased by 250 nm from 7.25 μm to 7.5 μm.
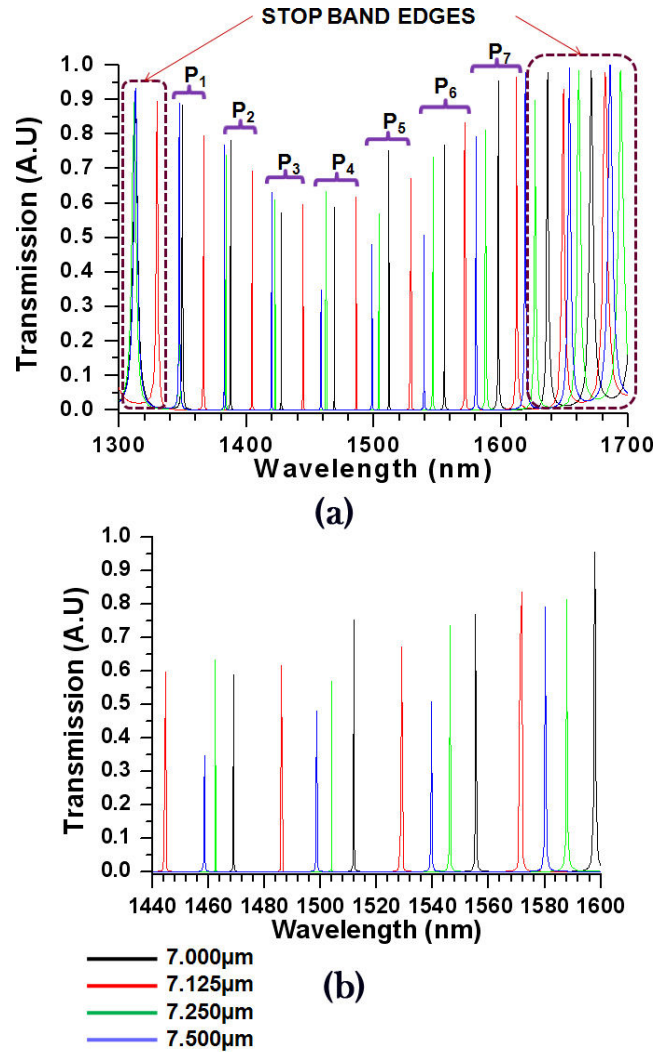
**Fig.5.5**:*2D FDTD calculations for a difference in cavity length with tapering both within and outside cavity with- (a) whole spectrum between the two band edges, (b)The resonances simulatedfor the limited range over which the optical characterization was carried out.*

The reduced FSR value of approximately 42 nm is also observed, in comparison with the previously calculated FSR for the short and medium extended cavity situations. But for small increases in the cavity length, where the extended cavity is expanded in steps of 1.25 nm from a 7 µm spacer length – the overall shift in the resonance wavelength is somewhat larger.
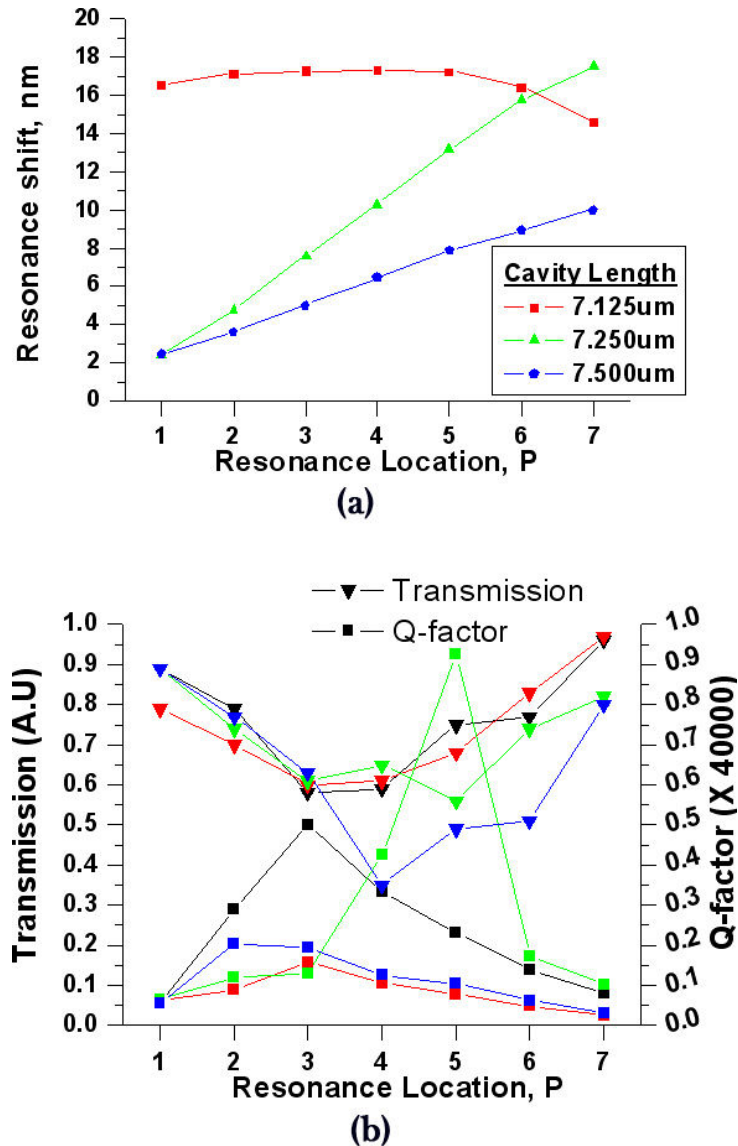
**Fig.5.6***:2D FDTD calculations for (a) A shift of different steps in cavity length, $C_E$ at each resonance location as compared to the resonances excited by 7 μm long spacer. (b)The resonance Q-factor and optical transmission for each set of resonances excited for different cavity spacers for the case with tapering both within and outside cavity.*

*Fig5.6 (a)* shows that, for the condition where the size of the 7 μm spacer is increased by 125 nm ($C_E$=7.125 μm), a large resonance wavelength shift is obtained, with the average shift of the resonances from the central resonance wavelength for $C_E$ = 7 μm *(shown in Table 5.2)* being approximately 16 nm for each resonance condition. The

larger shift became obvious for the resonance wavelengths in the shorter wavelength region of P1 to P4. Whereas a 250 nm shift in the spacer length (i.e. $C_E$=7.250 µm), gives rise to a smaller shift for P1 in the shorter wavelength regions. But rapid linear increase in the shift of the resonance wavelength towards the longer wavelength region is also obtained, in which the largest shift in resonance was observed at $P_7$, with a resonance wavelength shift of 17.3 nm.

As the cavity spacer increased in larger steps of 500 nm (i.e. $C_E$=7.5 µm), the resonance wavelength shift for each resonance condition increased at a slower rate than linear, where the largest shift was obtained at $P_7$ , with a shift of approximately 9.2 nm.

**Table 5.2***: Resonance central wavelength for resonances excited within stop band for $C_E$=7 µm*

|  | P1 | P2 | P3 | P4 | P5 | P6 | P7 |
|---|---|---|---|---|---|---|---|
| $\lambda_{0(7\mu m)}$ | 1349.12 | 1387.26 | 1427.19 | 1468.85 | 1511.79 | 1555.33 | 1597.81 |

The introduction of tapering within and outside cavity has been shown to enhance the Q-factor value, as well as the optical transmission with the calculated Q of more than 1000 and optical transmission of more than 50% at any resonance wavelength (between $P_1$ to $P_7$) for large extended cavity between 7 to 7.5 µm. The highest Q-factor value of approximately 41,900 was calculated at $P_5$, with $C_E$ = 7.125 µm and an optical transmission coefficient of approximately 55%. *Fig.5.6 (b)* shows the behavior of the Q-value and optical transmission coefficient for each resonance wavelength excited within the stop band – for the long extended cavity with space lengths between 7 µm to 7.5 µm, for the case of integration of the tapering effect both outside and within cavity. The optimum numbers of aperiodic holes used in this configuration were two and four, with respect to the use of tapering outside and within cavity. In general the Q-factor value changes for each cavity condition, where the highest Q-factor values were obtained in or around the middle of the stop-band (by referring to $P_3$, $P_4$ and $P_5$) – and with reduced optical transmission, as compared to the one which is closer to each band edge ($P_1$, $P_2$ ,$P_6$ and $P_7$). It can be deduced that although the increase in Q-factor resulted in a slight reduction in the optical transmission

coefficient, but when hole tapering is used outside the cavity, the optical transmission coefficient decreases at a slower rate, which implies that tapering outside the cavity also helps to maintain the optical transmission.

## 5.4     Experimental Results and Discussion for Extended Cavity

### Arrangement

The devices were measured using a tunable laser operating at wavelengths around 1.55 μm. The light was end-fire coupled into the waveguide via a 2 μm wide ridge waveguide. The waveguide was then tapered adiabatically from a width of 2 μm into the 500 nm wide photonic wire waveguide. The waveguide was then tapered back out using exactly the same arrangement for device characterization. The patterns were transferred into the silicon substrate using the VB6 Vistec electron-beam lithography (EBL) machine with the patterned negative tone HSQ resist also acting as the etch mask layer. The PhW waveguides were etched using Inductively Coupled Plasma (ICP) dry etching to remove the unwanted silicon areas. *Fig.5.7.* shows an SEM image of a device structure with a pattern of periodically and aperiodically located (and diameter tapered) holes embedded in it. The sidewall roughness of the waveguide has been reduced considerably because of the use of HSQ resist, thus reducing the intrinsic photonic wire propagation losses to values as small as 0.91dB/cm [21].
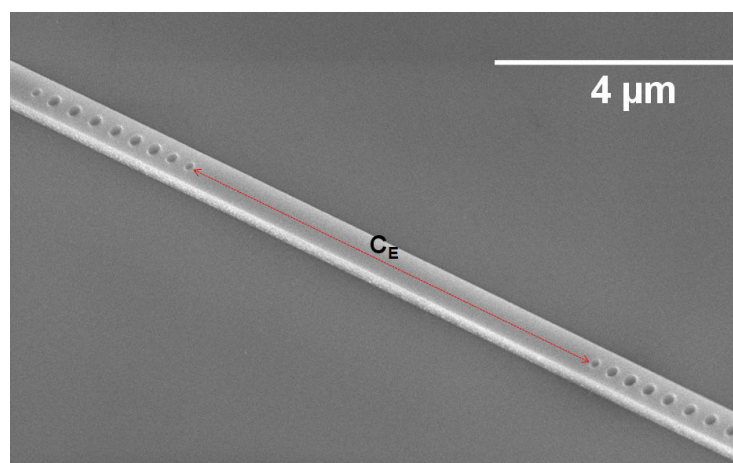


**Fig.5.7**: *SEM image of the PhC mirror embedded in a PhW waveguide, with smooth sidewalls –after dry etch processing where $C_E$ is the extended cavity length.*

The reduction in propagation losses is important for enhancing the optical transmission, as well as the Q-factor value at a chosen resonance frequency.
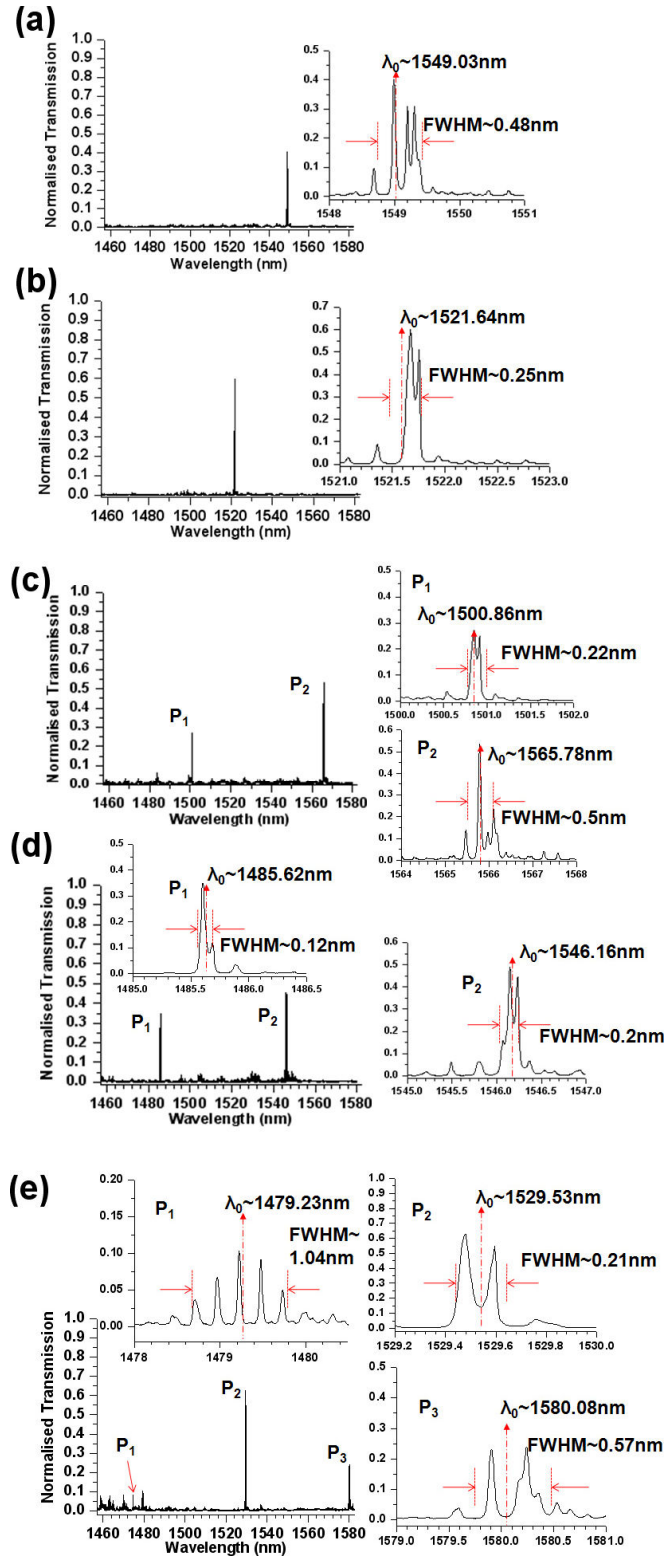


**Fig.5.8**: *Measured results for an extended cavity with tapering within cavity ($N_{TI}=4$) for (a) 2 µm (b) 2.5 µm (c) 3 µm (d) 3.5 µm (e) 4.0 µm*

All the devices were then measured using a tunable laser covering the wavelength range from 1.45 μm to 1.58 μm. TE polarized light was end-fire coupled into and out of the device waveguides – and the optical signal was then detected using a germanium photodiode. The experimental results were normalized with respect to an identical, but unstructured, nominally 500 nm wide PhW waveguide without any holes embedded in it. *Fig.5.8* shows the measured results for extended cavities with lengths in the range 2 μm to 4 μm, obtained with the use of aperiodic hole tapering within and outside cavity with $N_{TO}$=2 and $N_{TI}$=4 . The highest Q-value of approximately 12,400 was obtained with a cavity length of 3.5 μm situated at a resonance wavelength of 1485.62 nm with normalized transmission of approximately 35%- see $P_1$ in *Fig-5.8 (d)*.

By referring to *Fig 5.2,* (2D FDTD simulation result) for the case with spacer lengths of between 2 μm and 3 μm, the resonances excited within the limited measurement range may be for the second resonance, $P_2$, with the resonance $P_1$ lying at around 1421 nm (which is outside the measurement range). Given by the limited range of the tunable laser used for this present work (1457 nm to 1583 nm), the multiple resonance effect can only be seen at the cavity length greater than 3 μm or longer .Although, in the 2D FDTD simulation with shorter cavity length, i.e. 2 μm, the multiple resonances (three sharp peak) can clearly be seen *(refer to Fig.5.2)*.

At this cavity length (3 μm), the free spectral range (FSR) of the resonances was measured to be approximately 65 nm – whereas, at the cavity length of 3.5 μm, the FSR decreased to approximately 61 nm. The FSR value is further reduced to approximately 55 nm for the case of $C_E$=4 μm where, at this cavity length, the Q-factor for each resonance condition was measured to be approximately 1400, 7200 and 2700 with respect to $P_1$, $P_2$ and $P_3$. The Q-value was somewhat smaller than for other cavity conditions – which is partly due to the imperfections in the fabrication process. This is obvious at $P_1$, where the optical transmission is very low (approximately 8%) and there is some distortion around the resonance at $P_1$ which probably comes from fabrication imperfections. From our observations based on the simulation results shown in *Fig.5.2* to *Fig.5.5,* the number of Fabry-Perot resonances excited within the mirror stop-band wavelength range, due to the extended cavity, increased as the cavity length increased from 2 μm to 8 μm . This behavior is due to

the increase in the number of FP modes within the extended cavity region – corresponding to the number of half-wavelengths related to the cavity length, $C_E$.
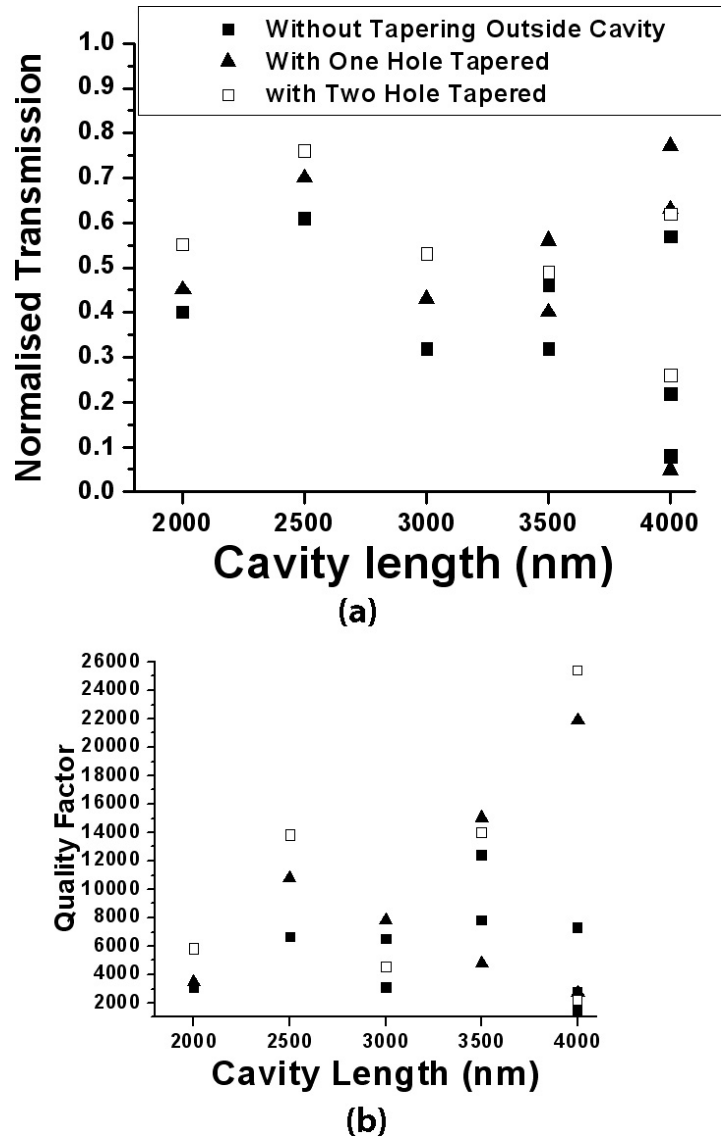


**Fig.5.9**: *The Variation of the optical transmission and Q-factor for tapering within cavity: ■-Without tapering outside the cavity, ▲-with one-hole tapering outside the cavity and □-with two-hole tapering outside the cavity*

The enhancement of the Q-factor value, together with the optical transmission, obtained via tapering both within and outside cavity- is shown in *Fig.5.9* – in structures that match the measurement results for the device shown in *Fig. 5.8*. A Q-factor value of approximately 25,400 has been measured at a cavity length of 4.0 μm,

with a normalized transmission of around 62% *(see Fig.5.9 (b))*- corresponds to $P_2$, with two hole taper structures outside the cavity *(see also Fig 5.8 (e) for comparison)*.
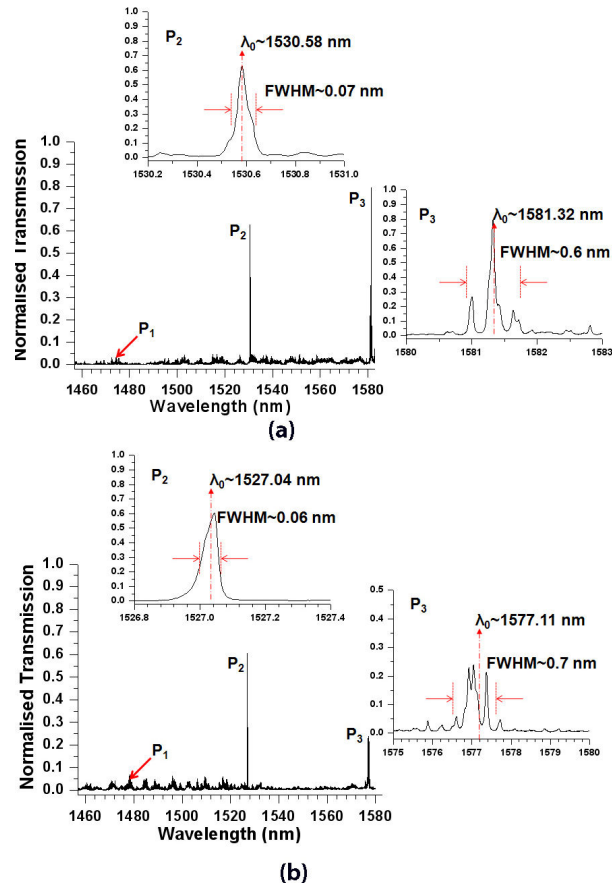


**Fig.5.10**: *Measured results for an extended cavity with tapering both within and outside cavity for $N_{TI}=4$ and (a) $N_{TO}=1$ (one hole taper outside cavity) (b) $N_{TO}=2$ (two hole taper outside cavity)*

For the medium extended cavity configuration, the highest Q-facto value achieved by using two hole tapering for the case of $C_E=4$ μm, with the normalized transmission at this cavity length being approximately 62%. *Fig.5.10.* shows the result for spacer length of 4 μm using $N_{TI}=4$ and different tapering outside cavity, $N_{TO}$, of one and two holes respectively. This result shows further enhancement by comparison the structures not using of hole taper outside cavity shown in *Fig.5.8 (e)*. As the number of holes in the aperiodic hole tapering outside the cavity (one or two holes), together with four hole taper within the cavity, $N_{TI}$, , the improvement of the Q-factor was measured for both cases but the normalized transmission was reduced by approximately 4% and 60% with respect to the resonances at $P_2$ and $P_3$. The inconsistencies in preserving the optical transmission in this case are rather difficult-

as somewhat surprisingly, at some point the Q has the opposite trend to the optical transmission. As the number $N_{TO}$ is increased to three and four aperiodic holes, the optical transmission is further reduced by an average of around 25% for each resonance. On the other hand, the Q-value started to reduce dramatically by almost half of the highest Q achieved for $N_{TO}=2$ , for $P_2$ shown in *Fig.5.10 (b)*.
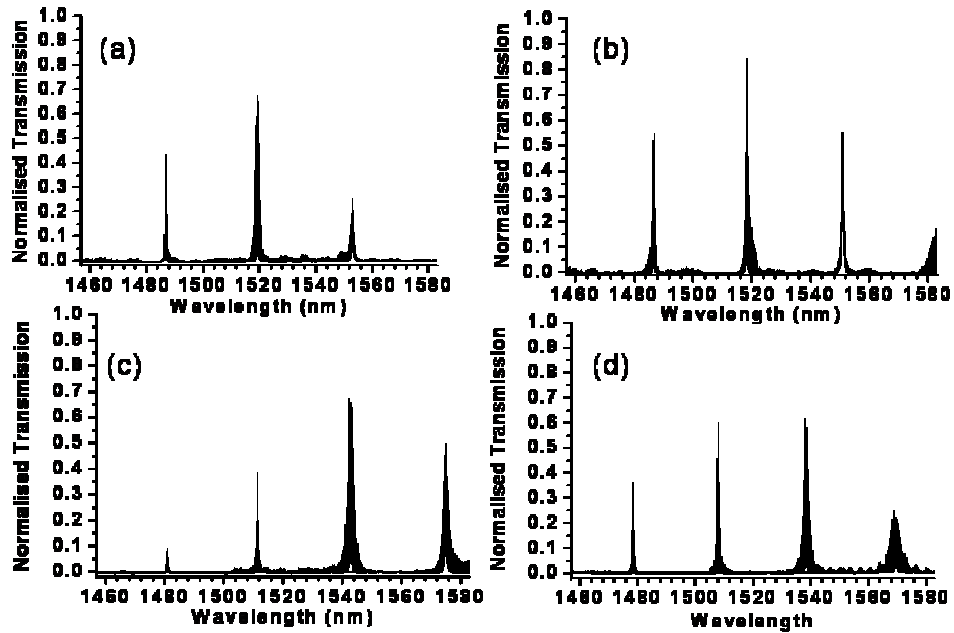


**Fig.5.11***: Measured results for 250 nm differences in the extended cavity length, without tapering effect. (a) 7.5 µm (b) 7.75 µm (c) 8 µm (d) 8.25 µm*

On the other hand, using a longer cavity, of more than 7 µm in length, shows multiple Fabry-Perot resonances excited within the stop-band. It also shows a significant shift of the resonances, with a 250 nm variation in cavity length, by approximately 10 nm. This variation is essentially an arbitrary choice since this value is approximately a half wavelength at the effective index of the guided light propagation in the silicon photonic wire. But if a smaller variation applies, i.e. 125 nm, a larger shift is expected, as already described in discussion the 2D FDTD simulation in the *section 5.3.3*. As the cavity length is extended further to around 7 to 8 µm, multiple FP resonance are excited with smaller FSR values, as compared to previously measured device structures with short or medium extended cavities. *Fig.5.11* shows the trend of

the resonances obtained using long extended cavities ranging in length from 7.5 μm to 8.25 μm, with progressive increases of 250 nm in cavity length – *see Fig-5.11 (a)-(d)*. These results represent the initial stage of investigations into the characteristics of multiple Fabry-Perot-like resonances at longer cavity lengths. The results in *Fig. 5.11* are based on designs without any tapering effects yet imposed on the periodic-hole mirrors. The highest Q-value of 3500 obtained was measured at a resonance wavelength of 1512 nm, with a cavity length of 8 μm – *see Fig. 5.11 (c)*. On the other hand, a shift of 10 nm in the resonance frequencies was also observed for a 250 nm variation in cavity length for those cavity conditions. In addition, a consistent trend of the distance between resonances (FSR values) of approximately 33 nm, 32 nm, 31 nm and 30 nm for each case is measured. This is due to the shift of the resonance for different spacer length, $C_E$ for resonance at shorter wavelength region towards the longer wavelength region which has been measured for the successive extended cavity conditions.

## 5.5 Achieving Ultra-high Quality Factor Extended Cavity 1D

### PhC/PhW Structures

The introduction of tapering both within and outside the cavity in longer cavities using aperiodic tapers with different hole diameters, as mentioned earlier (*in Chapter 4, section 4.3*), has led to a significant increase in the Q-factor values obtained, as well as increased optical transmission at the resonance frequencies. The high Q values achieved are mostly due to the reduction of the modal mismatch between un-patterned wires and the periodic mirror sections through correct arrangements of aperiodic tapered holes together with the correct parameters for the periodic hole mirror structures. *Fig 5.13* shows a zoom-in of the resonances ($P_1$, $P_2$, $P_3$ and $P_4$) excited corresponds to the measurement result shown in *Fig.5.12 (b)* – with the existence of fine feature next to the actual resonance. The presence of this fine feature is associated to the Fabry-Perot (FP) effect due to the end cleaved facets. Therefore, the existence of this feature has resulted in ambiguities for the estimation of the Q-factor values.
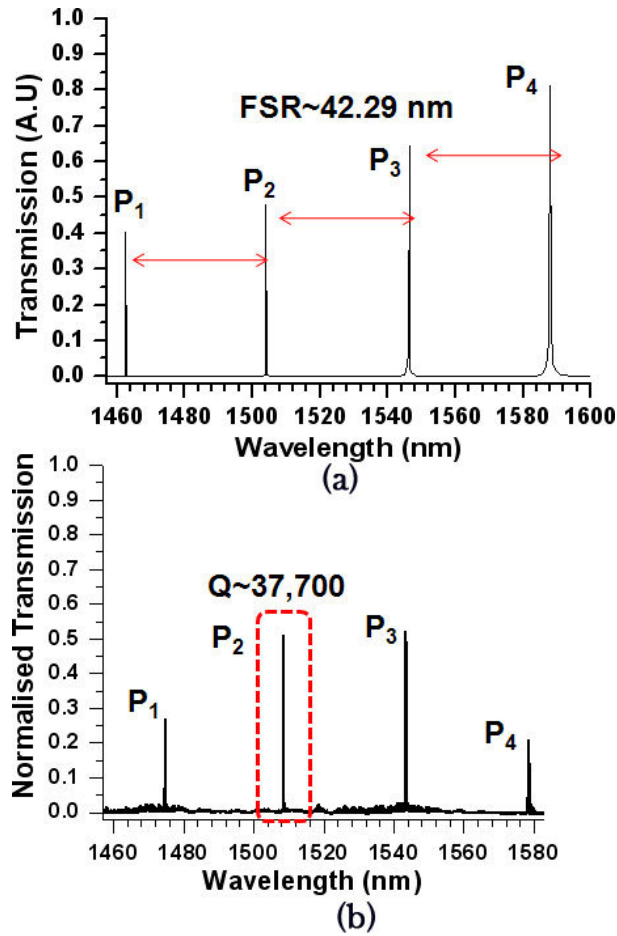
**Fig.5.12***: Comparison of high Q Tapered extended cavity with cavity length=7.25 μm, $N_{TI}$=4, $N_{TO}$=2 showing (a) 3D FDTD simulation result (b) Measurement result with Q-value of 37,700 at λ~1509 nm for $P_2$*

Throughout this presence work, the distance between the points of the arrows has been used to obtain, in a reasonably conservative manner, the estimates of the resonance quality factors, via the 3 dB points – as already discussed in the *section 4.4.2*. But the Q-factor values obtained using this approach shows a significant agreement between the measurement and the simulated results. The 3D FDTD simulation of *Fig. 5.12 (a)* yields a Q-factor value of approximately 45,000, in good agreement with the measured value of approximately 37,700 at the resonance wavelength of 1509 nm. The difference in the optical transmission between the 3D FDTD and the measured result is likely to be due, at least in part, to imperfections in the fabrication of the tapered hole sections used for this device – and such fabrication

imperfections will also contribute to the reduction in the Q-factor value of the simulated results.
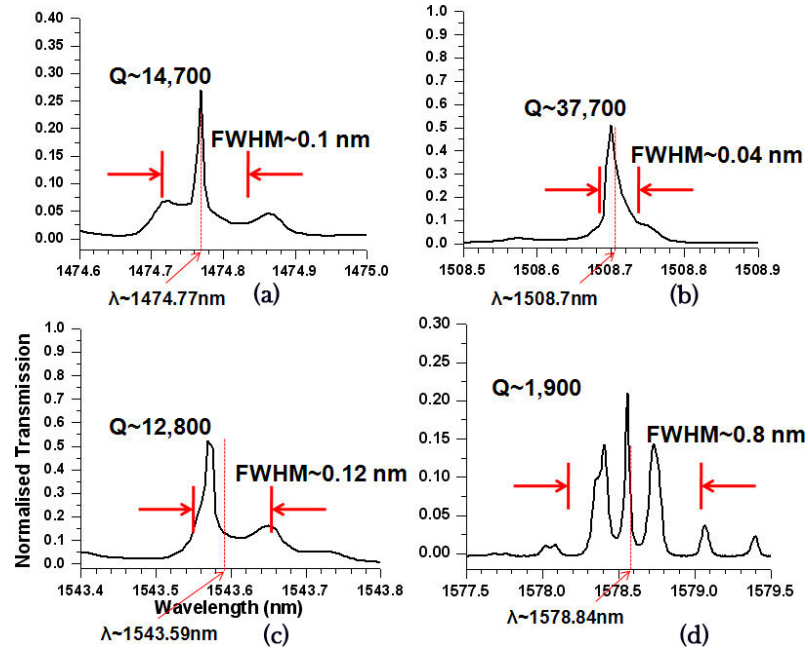


**Fig.5.13**: *Close-up of the measurement result for high Q Tapered extended cavity with cavity length=7.25 μm for (a) $P_1$ (b) $P_2$ (c) $P_3$ (d) $P_4$ corresponds to Fig.5.12 (b).*

By using the correct cavity length, the Q-value and optical transmission can be further enhanced – e.g. the Q-factor value of approximately 74,000 was obtained by using a cavity length of 5 μm in a medium extension cavity device structure. *Fig.5.14* shows the measured results for a 5 μm medium extended cavity with a Q-factor value of approximately 74,000 at a resonance wavelength of 1482.56 nm, which corresponds to the simulation result discussed in *Fig. 5.4 (a)* – where the resonance Q-factor value calculated using 2D FDTD computation for this design arrangement was approximately 97,000 –and the resonance was located at the central wavelength of 1472 nm.
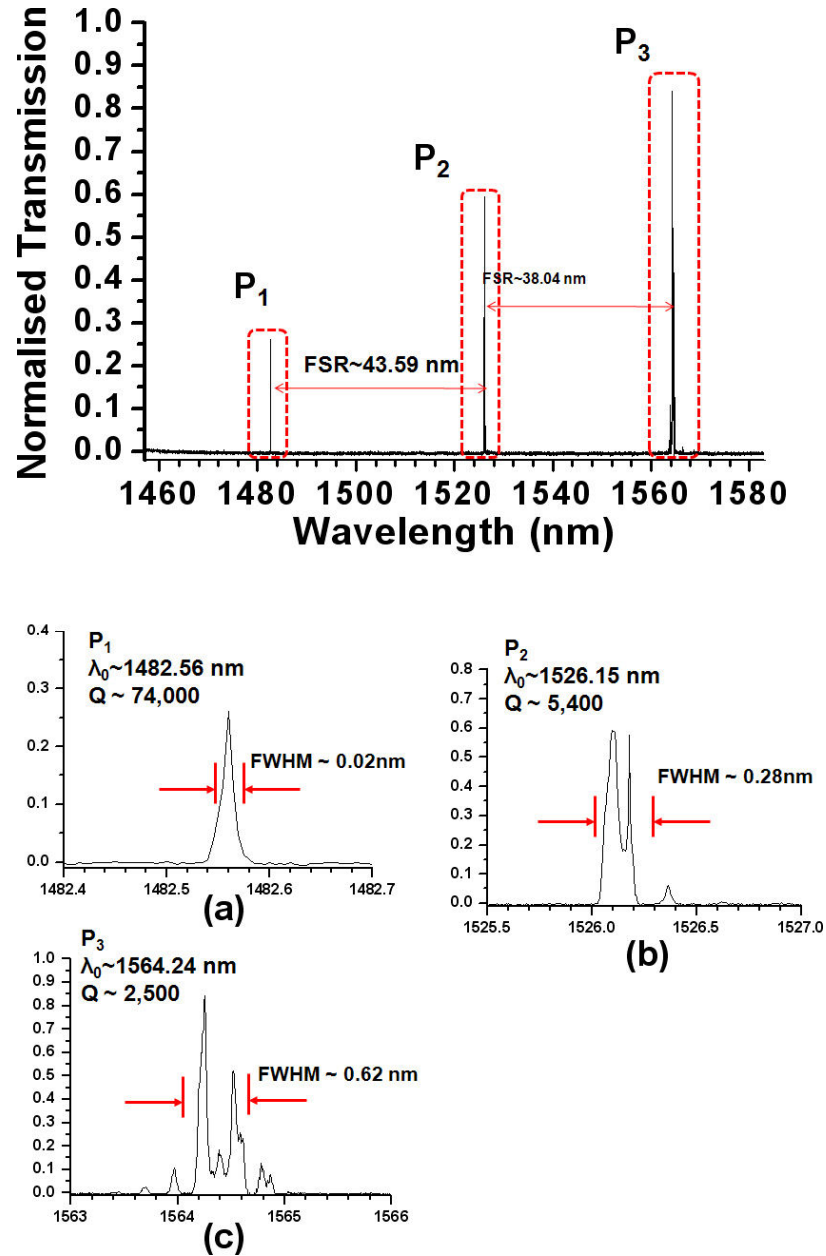
**Fig.5.14**: *Measurement result for ultra high Q extended cavity of c=5.0 μm with resonance (a) P₁ (b) P₂ and (c) P₃*

This experimental result also shows a significant difference, of 10.56 nm, in the resonance wavelength of the measured result for this particular design at $\lambda_0$-1482.56, in comparison with the simulated results. As discussed in *Chapter 2*, the variation of the location of the resonance wavelength is expected to be due, in part, to the approximation implied in using the effective index of the waveguide for 2D FDTD calculations. This problem can be overcome if 3D FDTD computation is used – in which the actual refractive index of the materials is used for the whole structure – and

there is a need for parallel cluster computing, which was not readily available during the period of this present work
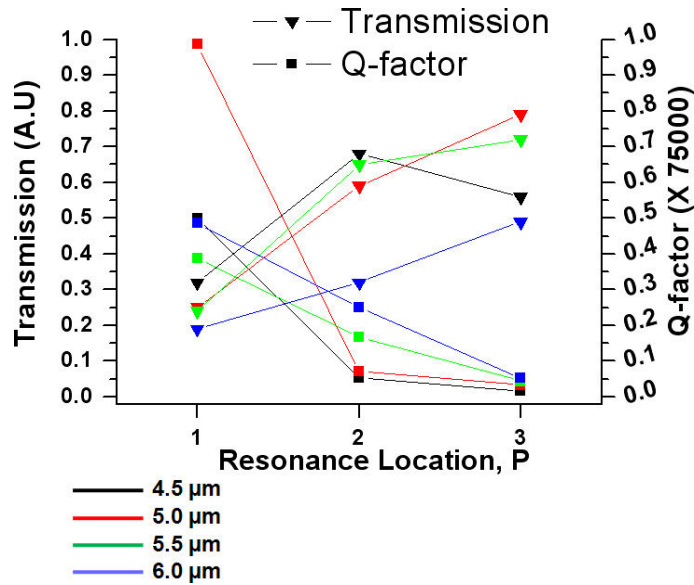


**Fig.5.15**: *The behavior of Q-factor value for each resonance condition in particular for medium extended cavity spacer of 4.5 μm, 5 μm, 5.5 μm and 6 μm.*

The FSR values measured for this particular caseare approximately 43.6 nm and 38 nm, between the three resonances excited within this optical wavelength range. These results have shown further that the use of tapering both within and outside cavity enhances the quality factor, as well as the optical transmission, which could be useful for telecoms applications such as switching, non-linear optics, slow light experiment and WDM. *Fig.5.15* shows a comparison of the Q-factor and optical transmission of a medium extended cavity for other spacer lengths around the medium spacer length – which are 4.5 μm, 5.5 μm and 6 μm. For each different cavity length, the highest Q-factor value was obtained at $P_1$, with estimated Q-values of 37,400, 74,000, 29,000 and 36,500, respectively- and mostly located near the centre of the stop band. The Q-factor values decreased dramatically for $P_2$ and $P_3$ , as the resonance moved towards the band edges.

The combination of tapering within and outside the micro-cavities, with a correct choice of hole diameters and spacing, has proven to have great influence on the challenge of achieving large Q-factor values together with high optical transmission for the extended cavity arrangement. For easier understanding of the

device, the overall performance of this device is illustrated in *Fig.5.16 (a)* – which is based on the highest value obtained at the resonance for each cavity condition. This resonance condition is located within the limited range of the characterization capability that was available throughout this present work (a tunable laser operating between 1457 to 1583 nm for 0.005 nm steps).
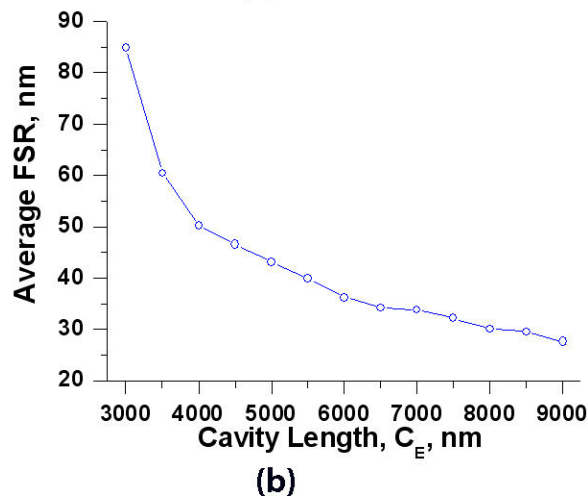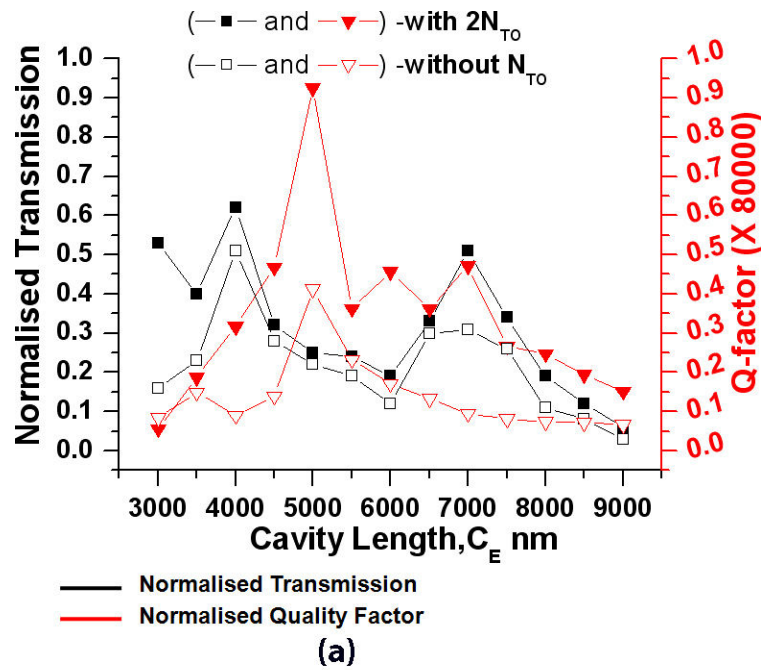


**Fig.5.16**: *(a) A comparison of Q-factor against normalized transmission of an extended cavity length, $C_E$ ranging from 3 μm to 9 μm for different hole tapered arrangement for $N_{TI}=4$. (b) A Graph showing the average FSR value at each cavity conditions.*

Most of the Q-factor and transmission values measured were located at around 1475 nm to 1510 nm, which correspond to the resonances of $P_1$ or $P_2$. For simplicity, only the highest resonance Q-Factor and normalized transmission value are considered for each cavity condition. From *Fig.5.16 (a),* it can be deduced that the highest Q-value of approximately 74,000 was obtained at a cavity length of 5 μm. This value was achieved with the use of both tapering within and outside cavity. On the other hand, the largest normalized transmission of more than 60% was measured at a cavity length of 4 μm, but the Q-factor at this resonance condition was smaller, at 45,000 for the case of using both tapering within and outside cavity ($N_{TI}$=4, $N_{TO}$=2). Above all, the use of both tapering outside and within cavity has shown great improvements, as compared to the results obtained without any hole tapering outside the cavity. In addition, the FSR value between resonances for each cavity condition reduced as the cavity length increases. This value changed exponentially with respect to the 500 nm change in cavity length, as illustrated in *Fig.5.16 (b).*

## 5.6        Suspended Silicon waveguide extended cavity

In this section some of the results obtained through removing silica cladding directly beneath the silicon waveguide will be discussed. Further enhancement of the Q-factor and the normalized transmission is potentially achievable through the removal of the silica cladding underneath the silicon core, as described in the fabrication chapter earlier (*Chapter 3- section 3.6*). On one occasion, at a cavity length of 4 μm, an extended cavity based on a suspended photonic wire has been successfully fabricated and measured. The Q-factor values achieved for  this cavity condition are 3900, 16,900 and 14,700 with respect to the resonance wavelengths of approximately 1470.3 nm, 1525 nm and 1574.5 nm- as shown in *Fig.5.17 (b).* Although somewhat surprisingly, we have found that the normalized transmission for the resonance at P1 is very small as compared to the resonances at position P2 and P3. The measured normalized optical transmission for resonances P1, P2 and P3 were 3.5%, 29% and 48% respectively. These resonances were normalized with respect to an un-patterned suspended wire without photonic crystal embedded in it. The resonances were measured to have a free spectral range (FSR) of 52 nm. In comparison, *Fig.5.17 (a)* shows the resonance excited for the case of unsuspended extended cavity structures at $C_E$=4 μm. A significant improvement has been made for this particular case, where

the Q-factor values increased considerably from 1400, 7200 and 2700 to 3900, 16,900 and 14,700 with respect to each resonance condition of $P_1$, $P_2$ and $P_3$. A shift of resonance by approximately 4 nm towards the shorter wavelength region is also observed- indicating that the removal of silica underneath the silicon waveguide has reduced the average refractive index of the silicon − thus shifting it to a shorter wavelength region.
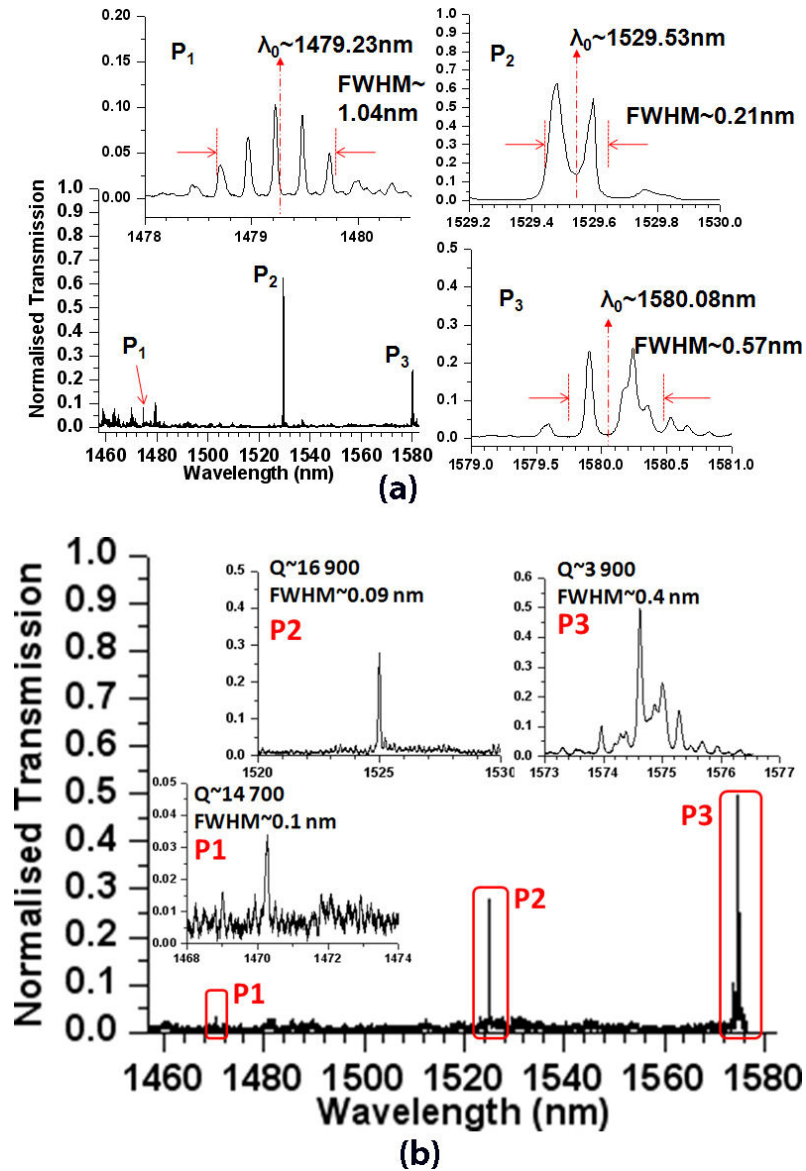


**Fig.5.17**: *Comparison of the measurement result of an extended cavity of $C_E$=4 μm for (a) with silica cladding (non-suspended wire) (b) suspended wire extended cavity*

The difficulties in achieving high transmission and high Q-factor values for the suspended wires of this particular device may be attributed to the abrupt change of the modal distribution when traveling from the feeder waveguide on a silica cladding into the suspended wire region, where the silica has been removed. But no attempt has been made so far to measure the loss at that interface, which we believe is a key factor for enhancing the optical transmission. No attempt has yet been made to normalize between suspended wires without the photonic crystal micro-cavity in them and the suspended wires with micro-cavity included. More work on the fabrication process for a suspended wire is desirable. The reproducibility of the suspended wire type of structure is low- with different outcomes from the fabrication process in each fabrication cycle. The most frequent problem obtained was the wire collapsing. The measurement needed to be taken less than two weeks after fabrication, since otherwise the suspended wire was found to have collapsed, probably due to the combination of environmental effects such as humidity and sample stress. This problem could potentially be overcome by a suitable encapsulation approach and sample annealing processes, where the suspended wire can be placed securely.

## 5.7 PhC/PhW Coupled Micro-Cavities

This section proposes that the coupling strength of the two micro-cavities separated by several holes with different diameters and hole spacing can be substantially influenced by the actual tapered hole combination used in the separation region between the micro-cavities. In this section, the design is described of PhC coupled micro-cavities consisting of a combination of mirrors formed by N periodic hole PhCs with diameters of 182 nm and periodic spacing of 350 nm. Two such micro-cavities with spacer sections, c1 and $c_2$, both 450 nm long were coupled to form a double-cavity structure - as illustrated in *Fig.5.18*. The existence of the two spacers or coupled micro-cavities has resulted in the splitting of the individual resonance into two resonances. The coupling strength of the two resonances very much depends on the arrangement of tapered hole structures within the cavity. In this section, the design of this particular device is divided into three different sections, as shown in *Fig.5.18*. For this case, no effort has been made to explore more on how the parameters such as small variation of cavity spacer length affect the resonance, since it has been shown

earlier that it does shifting the resonance to the required wavelength - and more importantly the high Q-values only appear at certain cavity lengths.
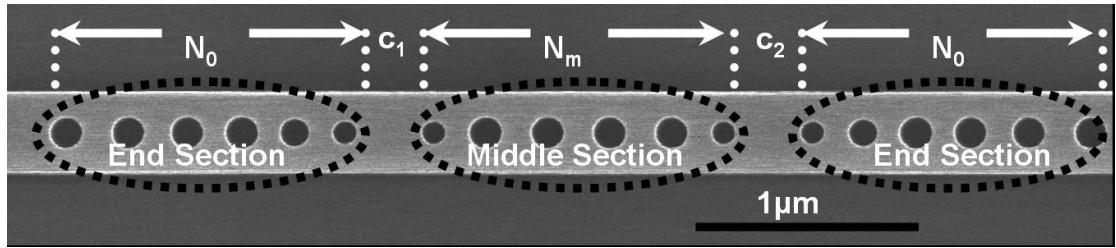


**Fig.5.18**: *SEM image of two micro-cavities between three periodic mirror with cavity length, $c_1$ and $c_2$ (edge-to-edge distance between two hole at micro-cavity), Number of hole at each side of the micro-cavities, $N_0$ and the number of hole between two micro-cavities, $N_m$*

But in this section the main intention is to look at how the coupling strength varies with the tapered hole arrangement- although high optical transmission is desirable. *Fig.5.18* shows an SEM image of a structure formed by two coupled micro-cavities, with a cavity spacer length of $c_1 = c_2 = 450$ nm. This structure was divided into three sections, consisting of two end sections, $N_0$ and a middle section, $N_m$. In order to reduce the modal mismatch for light entering from un-patterned wire waveguides into the mirror region, a tapered structure consisting of a combination of several aperiodically located holes and different diameters was used. The use of tapering both outside and within the cavity has produced a significant improvement in the optical transmission level, as well as much higher quality-factor for the selected resonances of the cavity. The four hole tapered structures used in our design have diameters of 170, 180, 166 and 131 nm sequentially, together with centre-to-centre hole distances of 342, 304, 310 and 290 nm, respectively. On the other hand, the two hole tapered structures used outside the cavity had diameters of 166 and 131 nm - with centre-to-centre hole distances of 310 and 290 nm. Both end sections, $N_0$, have two identical PhC hole arrangements - forming periodic mirrors, together with four aperiodically located holes forming tapers within the cavity. The tapered hole structures within the cavity have the same dimensions as were used previously in the micro-cavity structure - for both end sections. Control of the hole parameters has been shown to reduce the modal mismatch between un-patterned wire sections and mirror sections - thus enhancing optical transmission as well as the Q-factor value.

### 5.7.1     2D and 3D FDTD approach for Coupled Cavity Arrangement

The 2D FDTD approach has been used to simulate the device. Although 3D FDTD computation is obviously the desired method, the 2D FDTD approach is sufficient to provide a basic understanding of this kind of structure. A comparison has been made between 2D and 3D FDTD computation, as shown in *Fig.5.19*. It shows that the 3D FDTD approach gave a closer approximation to the measured result, with a calculated Q-factor of 1,200 - which agreed with the Q-value measured - approximately 1,100 for this particular design arrangement. The normalised transmission of approximately 60% also shows good agreement with the value computed using the 3D FDTD approach. A 2D computation gave a useful approximate description of the device behaviour, without giving much specific information on the device performance, when run at the low resolution required to reduce the simulation time.
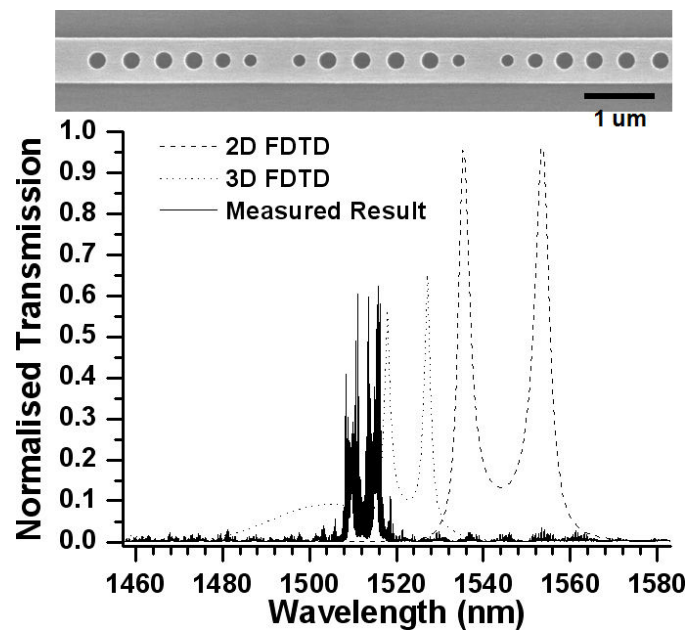


**Fig.5.19**: *A comparison between 2D and 3D FDTD approach with the measurement result for two coupled micro-cavities with $N_0$-$N_m$-$N_0$ (6-6-6) arrangement,  c=450 nm, and 1 hole taper in the middle section ($N_m$).*

Although 3D FDTD computation at reasonably high resolution is preferable, running a single simulation on a stand-alone PC, will normally take on the order of two to three weeks - which is not practical at  research level. Therefore, throughout this

section, 2D FDTD computation has been preferred for investigation of the general behaviour of the devices considered.
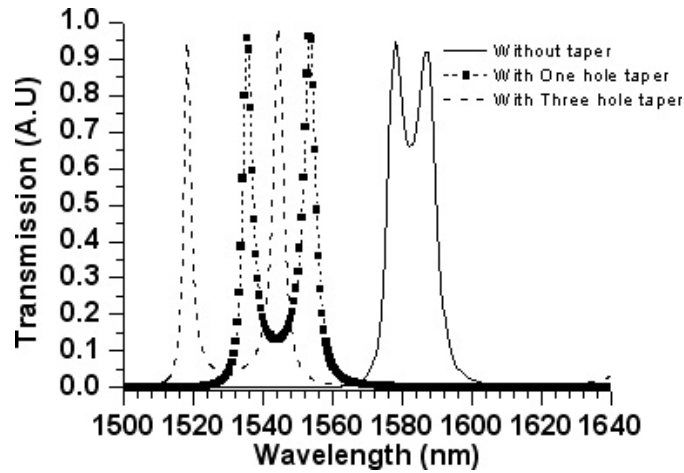


**Fig.5.20**: *2D FDTD simulation for 6-6-6 ($N_0$-$N_m$-$N_0$) hole arrangement with different hole taper arrangements in the middle section, $N_m$.*

At this point, a different number of holes was used in the tapered part of the middle section, $N_m$, by keeping the total number of periodic and aperiodic holes to six, for device simplicity - and to facilitate a consistent analysis. *Fig.5.20* shows the transmission spectra for a 6-6-6 ($N_0$-$N_m$-$N_0$) hole arrangement using different numbers of holes in the tapered part of the middle section, computed using a 2D-FDTD numerical approach. As the number of holes in the tapered part of the middle section is increased from one to three holes, a clear resonance splitting is predicted, implying stronger optical coupling between the two cavities. The split of the two resonances calculated in the successive cases are 9.90, 7.65 and 26.74 nm, respectively. In addition, the resonance obtained with a greater number of tapered holes used in the middle section also showed more pronounced resonance splitting as compared to the multiple resonance for the situation without any hole tapering imposed- thus implying that stronger coupling was observed for the three hole taper case. But the shift of the resonance is noticeable, whereas the number of holes in the taper is increased while keeping the total number of holes in the a combination of periodic and aperiodic holes the same. The shift of the two resonances was calculated to be 9.53 nm - which makes it difficult to reproduce, as shown in the simulation results obtained in *Fig.5.20.*
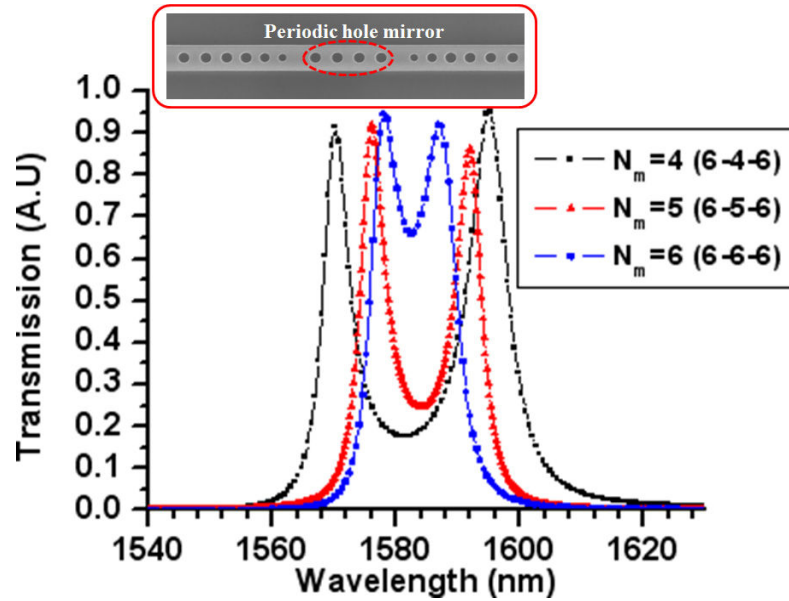
**Fig.5.21**: *2D FDTD simulation for different hole arrangements in the middle section, $N_m$, without any hole taper, i.e. using just a periodic hole mirror.*

Therefore varying the number of holes in the middle section without the need of hole tapering- i.e. using only a certain number of periodic holes in the separation mirror - was investigated, for example by using a different number of periodic mirror holes in the middle section- but without any tapering effect in those sections as shown in the inset of *Fig 5.21* (SEM image of the device structures). Using this arrangement, non-symmetric tapering within the cavity in the middle section was introduced. *Fig.5.21* also shows 2D FDTD simulation for different hole arrangements in the middle section, without any hole tapering being used. In this case, the centre position of the split resonance for different structure lies around 1584 nm. Clearer resonance splitting is seen as the number of periodic mirror holes in the middle section is reduced from six to four- with the separation of the resonances being increased from approximately 10 nm to 32 nm- implying stronger coupling of the cavities as the number of periodic mirror holes in the middle section, $N_m$ is reduced.

### 5.7.3        Measurement of Coupled Micro-cavities and Discussions

The characterization for this set of device structures was carried out using the same set-up as previously used (*see details in Chapter 3, section 3.7*). This device will work at the telecommunications wavelengths of 1457 nm to 1583 nm - being the limited

range covered by the tunable laser set-up used for the present work. *Fig. 5.22* shows the measurement results for the 6-6-6 ($N_o$-$N_m$-$N_o$) configurations, with variations in the taper hole arrangement in the middle section, $N_m$ - corresponding to the simulation results produced in *Fig. 5.20*, with a normalized transmission of around 60% at resonance. In this configuration, the number of tapered hole in the arrangement varies, while keeping the same number of hole in the middle sections, including both periodic and aperiodic holes. For example if two hole tapers of smaller size were used on each side of four periodic hole mirrors – the result was that the total number of holes (inclusive of periodic and aperiodic hole taper) remained at six. The introduction of two micro-cavities coupled together, has split the nominal identical cavity resonance frequencies into two, namely $\lambda_{0(1)}$ and $\lambda_{0(2)}$ in each case. A Clear resonance splitting is observed with a three hole tapered middle section. A significant shift in the position of the two resonances is obtained, as initially expected due to the progressive effective index change in the tapered hole part of the middle section. The calculated values for the resonance splitting measured for the successive cases are 2.74, 5.05, 13.82 and 17.85 nm respectively. As the number of periodically arranged holes in the middle section is reduced - and they are replaced by tapered hole sections with different diameters and aperiodic spacing, the optical coupling through the middle section becomes stronger - and therefore the resonance split between the two resonances increases. But multiple resonances with low transmission, of less than 5%, are also observed between the two clear resonances - in the latter two cases – and correspond to longer partial cavity structures formed between the middle mirror section and the outer ends of the outer cavity mirrors. The existence of the extra fine feature is discussed later in this chapter.
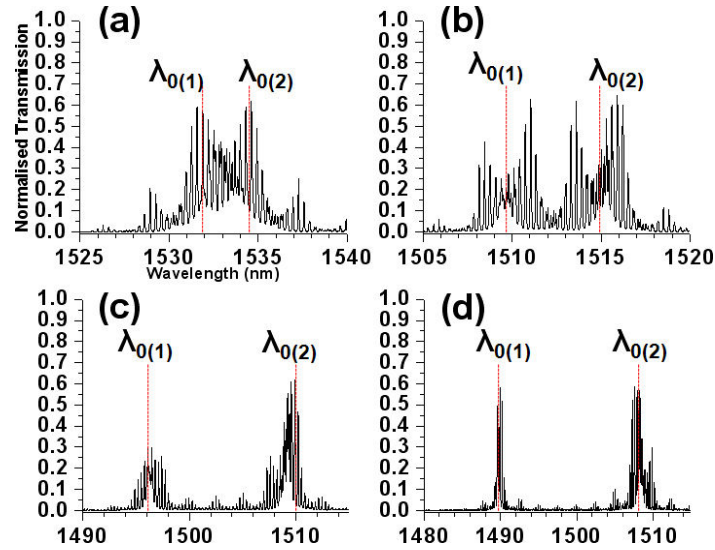
**Fig.5.22**: *Measurement result for 6-6-6 ($N_O$-$N_m$-$N_O$) hole arrangement corresponding to the 2D FDTD simulation results in fig-5.20 where $\lambda_{0(1\ and\ 2)}$ is the central wavelength of each resonances (a) without hole taper (b) with one hole taper (c) two hole taper and (d) with three hole taper in the middle section*

Clearly, the addition of suitable tapered hole structures at the input and output of the double cavity structure, as we have already demonstrated to be beneficial in the single cavity case, could well suppress such undesired features. As the number of periodic mirror holes in the middle section, $N_m$, is reduced to four (thereby becoming a 6-4-6 arrangement) for the situation with no tapered holes inserted in the middle section – a larger coupling strength is observed, with a clear resonance splitting. By Comparing the measurement results shown in *Fig. 5.22 (a)* with those in *Fig. 5.23 (b)*, the value of the separation between the two resonances has increased by 7 nm, from 2.74 to 9.74 nm, based on the measured results for this particular cavity condition. By inserting one reduced diameter hole into this particular design arrangement (maintaining four periodic holes in the middle section) - the coupling strength between the two cavities is further reduced - and accompanied by a reduction in the measured transmission by approximately 20%.
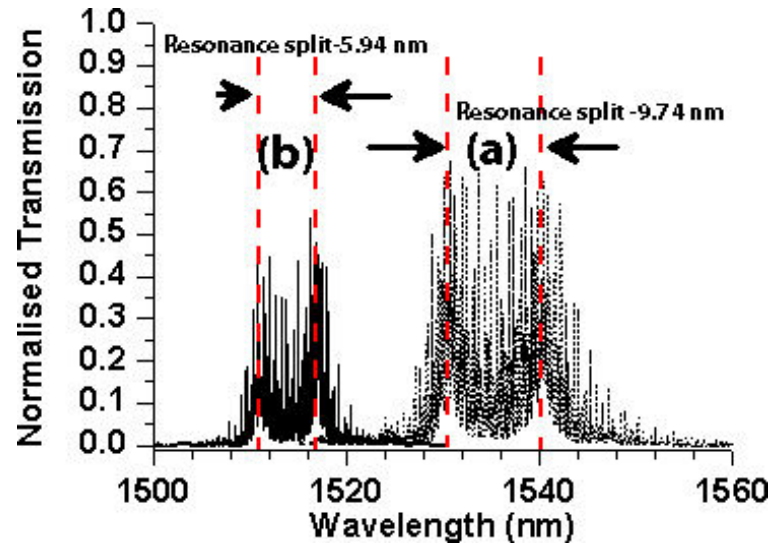
**Fig.5.23:** *Measurement result for $N_m$ with the periodic hole mirrors remains four at c=450 nm and (a) without hole taper (b) with one hole taper in the middle section.*

A reduction in the resonance splitting from 9.74 nm to 5.94 nm was obtained for this coupling condition - but a significant improvement in the Q-factor value from 400 to 1100 was also obtained.
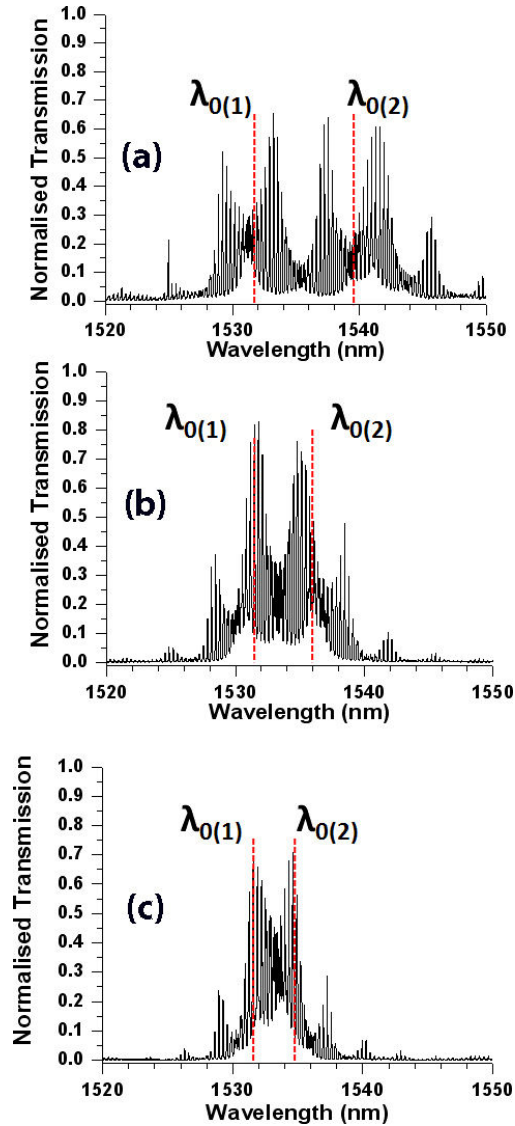
**Fig.5.24**: *Measurement results for different hole arrangements in the middle section, $N_m$ without any hole taper with a number of periodic mirror $N= N_m$ for (a) $N_m=4$ (b) $N_m=5$ and (c) $N_m=6$ - corresponds to 2D FDTD simulation results shown in* **Fig.5.20**

In previous measurements, *(see Fig.5.22 and 5.23)*, it was shown that a several tens of nanometer shift in the resonances could be obtained by using the same number of holes in the tapered middle section of the structures. The other way to keep the centre of the resonance around the same wavelength region while varying other parameters is through a change only in the number of periodic mirror holes in the middle section. *Fig.5.24* shows that the measured results for that particular case correspond to the simulation results obtained in *Fig.5.21*. As the number of periodic mirror holes is

reduced from five to four, more clear resonance splitting is observed, with the central wavelength between the two resonances in this particular case being measured to be around 1533 nm and 1535 nm respectively- with only approximately 2 nm separating those resonances.
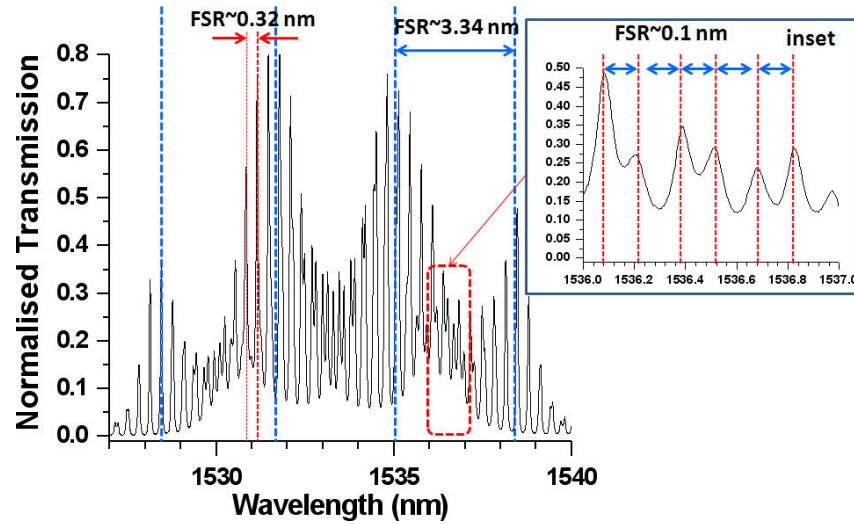


**Fig.5.25**: *One example showing a close look at the spurious resonance like features in one of the result shown in Fig.5.24 (c) - inset is the finest FP resonances feature.*

The resonance splitting for either design arrangement of having different numbers of periodic mirror holes in the middle section ($N_m$) of four and five respectively  was measured to be 8 and 2 nm respectively. Therefore clear resonance splitting has occurred, implying that a reduced number of periodic hole mirrors in the middle section ($N_m$) has resulted in an increase in the coupling strength of the resonance - with clearly larger resonance splitting. The normalized transmission coefficients for these resonance conditions were reasonably high, with the value measured being approximately 60% and 65%, respectively, showing the effect of tapering with smaller hole sizes in the cavity sections.
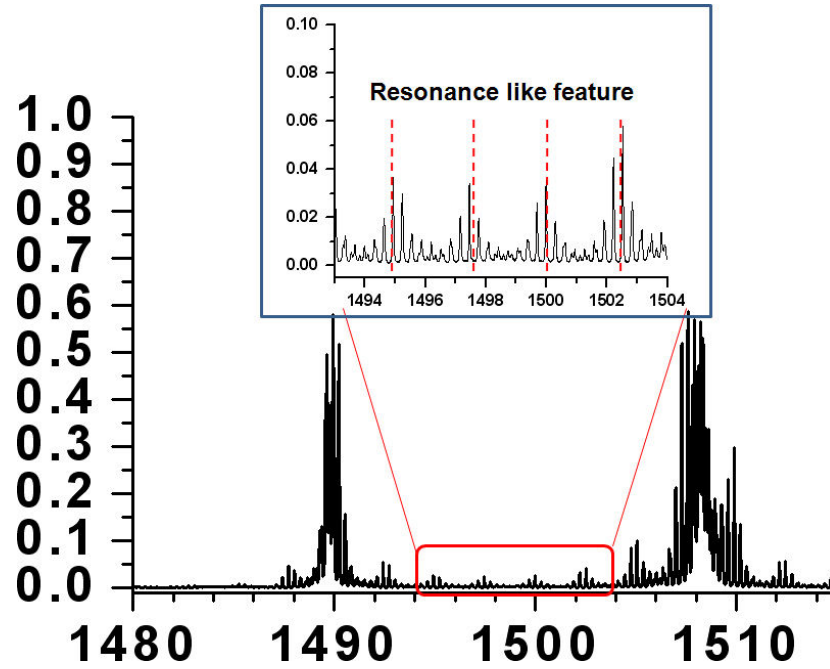
**Fig.5.26**: *Another example showing a close look at the spurious resonance like features in one of the result shown in Fig.5.22 (d)*

*Fig.5.27 (a)* shows a schematic drawing of the structures with a possible origin of fine features associated with the FP effect and *Fig 5.27 (b)* indicate the actual micro-cavity anticipated for this particular design (SEM image)- and the red arrows line indicate the other cavity created by the FP effect due to interface at the intersections to the adiabatic taper and the patterned wire waveguides which has quite a significant influence. The existence of fine features is seemingly obvious in the coupled micro-cavities, as compared with the basic features of the micro-cavities structures. This phenomenon is directly related to the 'double' Fabry-Perot (FP) effect produced by the coupled micro-cavities superimposed on the existing FP effect produced by the cleaved end facets, $FP_1$ and at the adiabatic taper section, $FP_2$ and $FP_3$, as shown in *Fig 5.27 (a)*. By referring to *Fig.5.25,* the resonance like feature presented by the blue line has an FSR of approximately 3.34 nm between the estimated central wavelengths of the 'envelope' measured in a rather conventional way, whereas the finer features shown by the red line has an FSR value of approximately 0.32 nm.

Based on the equation for the peak spacing of multiple FP resonances, the cavity length for any particular uniform resonance is given by [27-28]- where this famous equation are used in analysis of FP effect in laser cavities ;

$$L = \frac{\lambda_0{}^2}{2\ \delta\lambda\ n_g} \qquad (5.1)$$

*Where:*

$L$      *- Cavity Length of the FP effect associated with multiple resonances*

$\lambda$      *- Central wavelength of the associated resonances*

$\delta\lambda$      *- Distance between two adjacent resonance peaks*

$n_g$      *- Group refractive index (note: in this case the $N_g = N_{si} = 3.45$- this is based on the assumption of $N_g$ is big enough which approximately equal to actual $N_{si}$ – no further attempt is made at this stage to calculate the actual $N_g$)*

*Where $n_{eff}$ is given by;*

$$n_g = n_{eff} - \lambda \frac{dn_{eff}}{d\lambda_0}$$

By referring to *Fig.5.25* and on the basis of *equation 5.1*, for the resonant FSR value, corresponds to the each fine FP resonance feature, the cavity length associated with that particular resonance condition is given by;

1.  Blue Line:

$$L_1 = \frac{\lambda^2}{2\ \delta\lambda\ N_g}$$

$$L_1 = \frac{(1535.12)^2}{2\ (3.34)\ (3.45)} \qquad (5.2)$$

$$L_1 \approx 102\ \mu m$$

2.  Red Line:

$$L_2 = \frac{\lambda^2}{2\ \delta\lambda\ N_g}$$

$$L_2 = \frac{(1530.87)^2}{2\ (0.32)\ (3.45)} \qquad (5.3)$$

$$L_2 \approx 1100\ \mu m$$

$$L_2 \approx 1.1\ mm$$

3. inset:

$$L_3 = \frac{\lambda^2}{2\,\delta\lambda\,N_g}$$

$$L_3 = \frac{(1536.02)^2}{2\,(0.1)\,(3.45)} \qquad\qquad (5.4)$$

$$L_3 \approx 3400\ \mu m$$

$$L_3 \approx 3.4\ mm$$

Therefore, based on the schematic drawing of the whole structure shown in *Fig.5.27 (a)*, the fine features of the resonances for the cavities $L_1$, $L_2$ and $L_3$ may be calculated using *equation 5.2, 5.3 - and 5.4* and most probably originated from the FP effects of $FP_3$, $FP_2$ and $FP_1$ respectively.
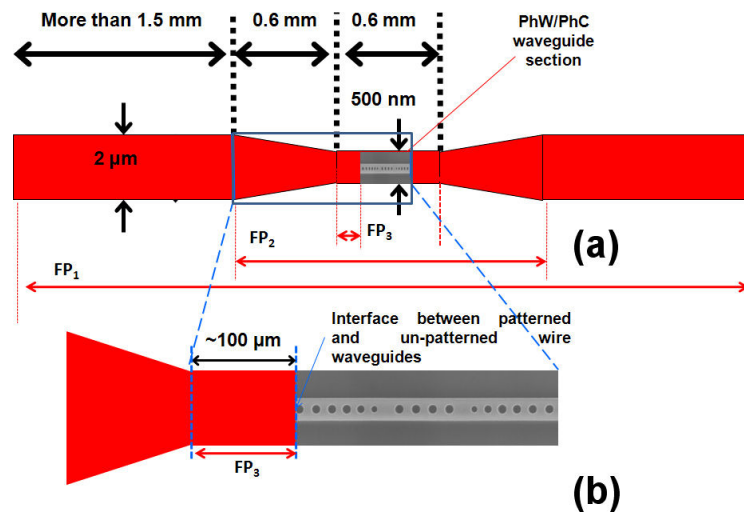
**Fig.5.27**: *(a) Schematic drawing of a design for PhC/PhW characterization showing the possible origin of multiple FP effect, $FP_1$, $FP_2$ and $FP_3$ (b) 'Zoom in' of the section showing te effect of FP fine feature between the start of patterned wire waveguides with the intersection with the adiabatic taper, $FP_3$ (Note: The schematic drawing are not in scale)*

In addition, the existence of 'extra' small features like resonance were also seen in other measurement result for example, as shown in *Fig.5.26 (see also Fig. 5.22)* in particular are mostly due to the Fabry-Perot effect of the systems shown in *Fig.5.27 (b)*. The FSR value for the multiple resonance features in this case is

approximately 3 nm- thus the cavity associated with this resonances are around 100 μm. Therefore this resonance feature appears in conjunction with the FP$_3$ shown in *Fig.5.27*. It becomes apparent that the FP effect is much more strongly present in the coupled cavity arrangement, as compared with single micro-cavity device structures - which implies that characterization of a two or more micro-cavity arrangement becomes more complex as spurious resonance features strongly appear due the FP associated with the end facets and adiabatic tapers arrangement at the entrance of the 500 nm PhC/PhW sections. The coarse structures resulted by the design arrangement can be overcome by reducing the multiple FP effect of whole system within the waveguides- and need to be re-design using inverse taper at the sample ends [23]- as initially proposed for coupling laser diodes into optical fiber [24-26]. Observation of the 2D and 3D FDTD simulation results obtained in one case (*refer to Fig.5.19*) shows that there are no spurious resonance-like features with the measured result for the coupled micro-cavity situation. This has confirmed that the 'extra spurious features' are isolated from the FP effect in the cavity regions formed by the coupled micro-cavity proposed - or FP effects due to the total length of the device structures. The 2D and 3D FDTD approach did not take the cleaved end facets and adiabatic taper into consideration, in order to run the device simulation effectively. It is also suggested that more work is needed on studies of the behavior of two or more micro-cavity arrangements - but general understanding has been developed sufficiently on the device structures of the present work.

**5.8**          **Summary**

In this chapter, the characterization of high-Q Photonic Crystal extended cavities embedded in 500 nm Photonic Wire waveguides have been demonstrated. Q-factor values as high as 74,000 for 5 μm long extended cavities have been obtained at a resonance wavelength of 1482.52 nm. This enhancement is due to the introduction of tapering both within and outside the cavity, together with a combination of aperiodic hole spacing and the correct choice of the periodic hole dimensions used in previous chapter. The resonance frequency can be tuned via small differences in the cavity length, although significant decreases in the Q-value were observed for the particular resonance of interest. A shift of approximately 10 nm in cavity length was also measured for a 250 nm difference in cavity length. Use of 2D FDTD computational approaches gives reasonably good agreement with the measured Q-value - with a calculated Q-factor value of nearly 100,000 corresponding to the measured Q-factor value of 74,000. This type of device could be useful for applications in communications such as DWDM and optical filtering. The initial investigation of an extended cavity longer than 7 μm shows a highest Q-factor value of nearly 3,400 for the case where no tapering was introduced. The resonances of this cavity were separated by approximately 30 nm in wavelength. In addition, further enhancement has been obtained where, with a measured Q-factor value of 37,700 for a cavity length of 7 μm. This resonance was at a wavelength of 1509 nm, with normalized transmission at this resonance frequency measured to be 40%. A 3D FDTD computational approach has been used to obtain a calculated Q-factor value of approximately 40,000, which is in a good agreement with the measured Q. Our measured results have shown a significant enhancement of the Q-value, as well as transmission, at chosen resonance frequencies due to the introduction of tapering effects. Experimental results have shown good agreement with both 2D and 3D FDTD computational approaches run at high resolution.

The experimental results for 1D PhC/PhW devices that use two coupled micro-cavities to split the cavity resonance in two have also been demonstrated - while retaining high optical transmission (of around 60%), which could also be useful for WDM applications. Control of the FSR of the combined resonance structures, through the use of different numbers of holes in periodic mirror holes and different

numbers of holes in the aperiodic middle section between the cavities has also been demonstrated. For the case where a constant combination of tapered holes and periodic mirror holes was used, it was shown that, as the number of tapered holes in the middle section increases, there is an increase in the coupling strength - thus splitting the resonance more clearly, with an FSR of approximately 17.85 nm. In contrast, for the same number of mirror holes in the middle section, increasing the number of holes in the tapered section produces a reduction in the FSR between the two resonances. 2D FDTD simulations have shown reasonably close agreement with the measured results. In conclusion, the coupled cavity design in a two-cavity arrangement is potentially useful as a basic building block for designing multiple-cavity structures - with a series of cavities providing the required spectral response for WDM de-multiplexing applications. We have also observed some discrepancy between the simulated and the measured results, presumably arising from fabrication inaccuracy and the limitation of a 2D approach to simulation.

**References**

1. J. D. Joannopoulos, R. D. Meade, and J. N. Winn, *Photonic Crystals: Molding the Flow of Light*. Princeton, NJ: Princeton Univ. Press, 1995.

2. T. F. Krauss, R. M. De La Rue and S. Brand: "Two-dimensional photonic bandgap structures operating at near infrared wavelengths", *Nature*, vol 383, 699-702, 1996.

3. T. F. Krauss and R. M. De La Rue, "Optical characterisation of waveguide based photonic microstructures," *Appl. Phys. Lett.*, vol. 68, no. 12, pp. 1613–1615, Mar. 1996.

4. M. Koshiba, "Wavelength division multiplexing and demultiplexing with photonic crystal waveguide couplers," *J. Lightwave Technol.* **19**, 1970-1975 (2001).

5. J. Smajic, C. Hafner, and D. Erni, "On the design of photonic crystal multiplexers," *Opt. Express,* **11**, 566- 571 (2003),

6. M. Loncar, T. Yoshie, Y. Qiu, P. Gogna, and A. Scherer, "Low-threshold photonic crystal laser," *Proc. SPIE* **5000**, 16-26 (2003).

7. M. Rattier, T. F. Krauss, J.-F. Carlin, R. Stanley, U. Oesterle, R. Houdrè, C. J. M. Smith, R. M. De La Rue, H. Benisty, and C. Weisbuch, "High extraction efficiency, laterally injected, light emitting diodes combining microcavities and photonic crystals," Opt. and Quantum Electron. **34**, 79-89 (2002).

8. Pottier P, Mastroiacovo S and De La Rue R M 2006 Power and polarization beam-splitters, mirrors, and integrated interferometers based on air-hole photonic crystals and lateral large index-contrast waveguides", O*pt. Express* **14** 5617–5633

9. Wu L J, Mazilu M, Gallet J F, Krauss T F, Jugessur A S and De La Rue R M 2004 Planar photonic crystal polarization splitter *Opt. Lett.* **29** 1620–2

10. Taillaert D, Chong H, Borel P I, Frandsen L H, De La Rue RMand Baets R 2003A compact two-dimensional grating coupler used as a polarization splitter *IEEE Photon. Technol. Lett.* **15** 1249–51

11. Shi S, Sharkawy A, Chen C, Pustai D M and Prather D W 2004," Dispersion-based beam splitter in photonic crystals", *Opt. Lett.* **29** 617–9

12. C.Ciminelli, F. Peluso, M.N. Armenise, and R.M. De La Rue," Variable Oblique Incidence for Tunability in a Two-Dimensional Photonic-Crystal Guided-Wave Filter", Journal of Lightwave Technology , Vol: 24, No: 1, January 2006.

13.    Ciminelli C, Chong H.M.H, Peluso F, De La Rue R.M and Armenise M.N 2004 High Q guided-wave photonic crystal extended microcavity, ECOC 2004, Stockholm (5–9 Sept. 2004), Post-Deadline papers Th4.2.6 pp 26–7.

14.    C. Ciminelli, F. Peluso, M. N. Armenise and R. M. De La Rue, "Variable oblique incidence for tunability in a 2D guided wave photonic band gap filter," J. Lightwave Technol.

15.    Jin C, Johnson N P, Chong HMH, Jugessur A S, Day S, Gallagher D and De La Rue R.M ,"Transmission of photonic crystal coupled-resonator waveguide (PhCCRW) structure enhanced via mode matching *Opt.Express* **13** 2295–302

16.    L.A.Everall, K.Sugden, J.A.R.Williams, I.Bennion, X.Liu, S.Aitchison, S.Thoms and R.M.De La Rue," Fabrication of multipassband moiré resonators in fibres by the dual phase mask exposure method", *Opt. Letters*, 22 (19), 1473-1475, October 1997.

17.    A.Yariv, Y.Xu, R.K.Lee and A.Scherer ,"Coupled-resonator optical waveguide: A proposal and analysis", *Opt. Letters*, **24** (11), 711-713, June 1999.

18.    D.O.Brien, M.D.Settle, T.Karle, A.Michaeli, M.Salib and T.F.Krauss, "Coupled photonic cystal heterostructure nano-cavities", *Optics Express*, **15** (3), 1228-1233, January 2007.

19.    A.S. Jugessur, P. Pottier and R.M. De La Rue, 'Engineering the filter response of photonic crystal microcavity filters', *Optics Express*, **12**(7), pp.1304-1312, 5th Apr (2004).

20.    A. Melloni and M. Martinelli, 'Synthesis of Direct-Coupled-Resonators Bandpass Filters for WDM Systems', *IEEE Jour. Lightwave Technology*, **20**(2), pp. 296 – 303, February (2002).

21.    M. Gnan, S. Thoms, D.S. Macintyre, R.M. De La Rue and M. Sorel, 'Fabrication of low-loss photonic wires in silicon-on-insulator using hydrogen silsesquioxane electron-beam resist', *Electron. Letters*, 44(2), 115 - 116, 17th Jan (2008).

22.    C.Ciminelli, R.M.De La Rue and M.N.Armenise,"High Coupling Efficiency in 2D Guided-Wave Photonic Band Gap Extended Microcavities for Sensing Applications", *Current Analytical Chemistry*, 4(4), page 362-370, October 2008.

23.     Vilson R. Almeida, Roberto R. Panepucci, and Michal Lipson," Nanotaper for compact mode conversion", *Optics Letters* , 28 (15), 1 August 2003.

24.     I. Moerman, P. P. Van Daele, and P. M. Demeester, *IEEE J. Sel. Top. Quantum Electron*. **6,** 1308 (1997).

25.     K. Kasaya, O. Mitomi, M. Naganuma, Y. Kondo, and Y. Noguchi, *IEEE Photon. Technol. Lett*. **3,** 345 (1993).

26.     O. Mitomi, K. Kasaya, and H. Miyazawa, *IEEE J. Quantum Electron*. **8,** 1787 (1994).

27.     Optical waves in layered media, P. Yeh, LIVRE, J. WILEY EDITIONS, 1988

28.     Waves and Fields in Optoelectronics, Herman.A.Haus, Prentice Hall, in Solid State Physical Electronics, 1984.

29.     Chyong-Hua Chen and Yeshaiahu Fainman*,* Photonic Bandgap Microcavities With Flat-Top Response", *IEEE Journal of Selected Topics in Quantum Electronics*, 13 (2), April 2007.

# Conclusions and Future Work

This thesis has demonstrated the detailed design, fabrication and characterization of single row PhC cavities embedded in narrow (typically 500 nm wide) photonic wire waveguides based on Silicon-on-Insulator (SOI). Three main design arrangement were analyzed and demonstrated, consisting of micro-cavities with spacer section lengths of between 400 nm and 500 nm, extended cavities where the cavity extends from between 2 μm and 9 μm and coupled micro-cavity structures. The device structures have been designed to operate in TE polarization at wavelengths around 1550 nm. The compactness, together with high reflectivity and possibilities for an active tuning capability make the device suitable as a basic building block for incorporation into integrated circuits where several functions are realized on a single chip − i.e. what are commonly known as high-density Photonic Integrated Circuits (PICs). On the other hand, it may also be useful in providing one of the solutions for the design of compact filters for either coarse or dense wavelength-division multiplexing situations, for high-speed switching and non-linear optics.

The development of high-resolution fabrication techniques plays an important role in achieving high performance in this device. The use of state-of-the-art lithography tools and processes has shown a significant enhancement of the device capability. Considerable improvement has been made in terms of work on fabrication techniques, where all aspects of critical stages in the fabrication process have been thoroughly investigated. The use of a newly installed electron-beam lithography tool namely the Vistec-VB6 tool has produced a significant improvement by comparison with the previously available Leica-EBPBG5 tool. The development of HSQ resist as a writable etch-mask layer for pattern transfer, rather than using ZEP-520A together with a deposited silica transfer layer, has also played an important role in reducing sidewall roughness, which in turn has reduced the propagation losses. Substantial

improvement has been achieved through a reduction in the number of fabrication process steps, provides excellent controllability in the fabrication of small feature sizes. Inductively Coupled Plasma (ICP), RIE tools was used to etch the silicon core with a limited amount of sidewall roughness. The device was finally characterized using tunable laser covering the range from 1457 nm to 1583 nm where the light was end-fired into the waveguide input end and detected using a germanium-photodiode detector at the other end. The result is subsequently normalized against the optical transmission of an un-patterned photonic wire without any holes embedded in it.

The fabricated device structures typically consist of a single row of holes embedded in a narrow ridge waveguide with a spacer section introduced in the middle, which has led to the achievement of usefully high quality factors, together with high optical transmission. The main source of light scattering was identified as the mismatch between the un-patterned photonic wire and the Bloch mode of the periodic mirror - and therefore the engineering of tapered hole structures at the input and output interfaces is necessary. This thesis will emphasize the design of hole tapers in order to obtain high quality factor values, together with usefully large optical transmission sufficient for telecommunications applications. Tapered hole regions consisting of several holes, between one and four, having different diameters and aperiodic spacing have been used. The main aim of such an arrangement is to provide a smoother and graded route for the light to travel into periodic hole mirrors. The tapered hole section at the interface between the un-patterned ridge waveguide and the periodic hole mirror-structure of the micro-cavity region led to an enhancement of both the optical transmission and the resonance Q-factor. The correct choice of the number of holes used - and the dimensions of the hole is the most important parameter in order to get the highest performance of the device. The device structures were initially modeled and simulated using both 2D and 3D FDTD. Although 3D FDTD computation is ultimately more useful, since it uses exact refractive index values rather than the effective index method used in the 2D FDTD approach, the massive memory requirements and high power consumption needed for 3D FDTD give difficulties. The use of parallel computing is required to produce substantially reduced simulation time.

The introduction of tapered hole structures consisting of several holes with different diameters and spacing at the entrance and the exit of the periodic hole

mirrors has produced a considerable improvement in both the optical transmission level and the quality factor values obtained, together with substantially reduced radiation losses. This reduction in the radiation losses is partly due to the reduction in the modal mismatch as the light travels from the un-patterned ridge waveguide into the periodic mirror region and on into the spacer region, where multiple transits occur. Using this design arrangement a Q value of approximately 147,000 has been achieved, together with a useful value of the normalized optical transmission. The expected increase in the quality factor and the enhancement of the optical transmission is due to the tapered hole mirror section, which increases the photon confinement lifetime within the cavity and reduces the modal mismatch. Furthermore, the tapered hole arrangement was also successfully introduced into the extended cavity and coupled cavity structures. A significant improvement in quality factor values and optical transmission has also been demonstrated in this particular case.

The extended cavity device structures with Q-values of approximately 74,000 with normalised optical transmission of 30% for 5 μm long extended cavity have also been successfully obtained. This enhancement is partly due to the introduction of tapering both within and outside the cavity, with a correct combination of aperiodic hole tapering and the correct choice of the periodic mirror hole dimension. This resonance frequency can be tuned via small differences in cavity length, although a significant decrease in thee Q-factor value was observed in some cases. Good control of the FSR is also demonstrated while varying the extended cavity length from 2 μm to 9 μm, which might be useful for some telecomm wavelength selection applications.

Finally, coupling of two micro-cavities has been used to split the cavity resonance into two - while retaining high optical transmission values (of around 60%), which could also be useful for WDM applications. Control of the FSR of the combined resonance structures, through the use of different numbers of holes in periodic mirror sections and different numbers of holes in the aperiodic middle section between the cavities has also been demonstrated. For the case where a constant total number of tapered holes and periodic mirror holes was used, it was shown that, as the number of tapered holes in the middle section increases, there is an increase in the coupling strength - thus splitting the resonance more clearly, with an FSR of approximately 17.85 nm. In contrast, for the same number of mirror holes in the middle section, increasing the number of holes in the tapered section produces a

reduction in the FSR between the two resonances. My 2D FDTD simulations have shown reasonably close agreement with the measured results. In conclusion, the coupled cavity design in a two-cavity arrangement is potentially useful as a basic building block for designing multiple-cavity structures - with a series of cavities possibly providing the required spectral response for WDM de-multiplexing applications.

In addition, the capabilities of the silicon core need to be explored more fully. For instance, tuning of this particular device can be implemented by means of either small variations of the cavity length or the thermo-optic effect. For the thermo-optic case, the current could be passed through the silicon photonic wire in which the cavity is formed, in order to deliver the desired refractive index change - which in turn will shift the resonance frequency, depending on the amount of current delivered [1]. Furthermore, the large positive thermo-optic coefficient of silicon ($1.83 \times 10^{-4} K^{-1}$) [2,3] can be exploited to produce a significant change of the refractive index in reference to the temperature (dn/dT). It is reported that a small amount of power of 9.2mW is needed to drive the resonance to shift by 5nm in wavelength without a change ion Q-factor [4]

In contrast to the use of heavily doped silicon – which can exploit either n-type or p-type dopant, as used typically in CMOS, the cavity region would be heated using a carefully designed micro-heater in which the refractive index change, in conjunction with the temperature change, will produce a shift in the resonance peak. An investigation of how large a current is needed to drive a useful shift in resonance will be carried out. On the other hand passing current directly into silicon that has been doped p-type will also be carried out. In this case, a silicon core will be doped with p-type (boron) to provide the path for the current flow through it. This current will heat up the silicon where change in temperature will result in refractive index change-thus a shift in resonance peak will be expected- although there are issues regarding the absorption losses.

Further enhancement of the Q-factor can also be achieved by removing the silica cladding underneath the silicon core layer, in order to provide better isolation of the light traveling within the silicon. Thus better light confinement inside the silicon can be achieved. Improvements in the Q-value, with useful optical transmission have been demonstrated via this method in one of the device structures - and I believe that

a Q-factor value greater than currently demonstrated can be achieved by completely removing the silica cladding to provide a symmetrical device with air surrounding the silicon core. But this demonstration of higher Q-factor values lies in the future work on optimizing the fabrication process of the membrane SOI, where the development of complete 'hanging' silicon is required. More attention to reducing the losses at the interface between the silicon sitting on the platform and the suspended silicon needs to be addresses carefully, in order to achieve the full capability of this device.

In conclusion, a Compact PhC/PhW device structure with ultrahigh quality-factor together with large optical transmission has been successfully demonstrated. This performance was achieved via the use of tapering both within and outside cavity. Further optimization of the fabrication process in the suspended wire configuration is necessary in order to enhance the performance of the PhC/PhW device structures still further. There is also possibility of embedding the silicon PhC/PhW micro-cavity structures with silica surrounding them - i.e. a complete silica environment. This can be achieved through a controlled silica deposition on the silicon waveguide. One of the advantages of using this approach is to provide an alternative to increase the optical confinement through the design of symmetrical ridge structure. For instance, the modal distribution through the silicon waveguide will be symmetrical especially in relation to the mode 'tails'.

**References:**

1. M. W. Geis, S. J. Spector, R. C. Williamson, and T. M. Lyszczarz, "Submicrosecond submilliwatt silicon-on-insulator thermooptic switch," *IEEE Photon. Technol. Lett.*, vol. 16, no. 11, pp. 2514–2516, Nov. 2003.

2. "Temperature dispersion of refractive indices in semiconductors," *J. Appl. Phys.*, vol. 79, no. 12, pp. 9388–9389, 1996.

3. Vilson R. Almeida, Roberto R. Panepucci, and Michal Lipson," Nanotaper for compact mode conversion", *Optics Letters*, Vol. 28, No. 15, August 1, 2003, pp 1302-1304.

4. Harold M. H. Chong and Richard M. De La Rue*," Tuning of Photonic Crystal Waveguide Micro-cavity by Thermo-optic Effect", *IEEE Photonics Technology Letters*, vol. 16, no. 6, June 2004, pp 1528-1530.